Title
Synthesis and Optimization of Praseodymium Telluride System Through Alloys and Composites

Author
Hogan, Brea Elizabeth

Publication Date
2023

Peer reviewed|Thesis/dissertation

UNIVERSITY OF CALIFORNIA
Los Angeles

Synthesis and Optimization of Praseodymium Telluride System Through Alloys and Composites

A dissertation submitted in partial satisfaction of the requirements for the degree
Doctor of Philosophy in Materials Science and Engineering

by

Brea Elizabeth Hogan

2023

ABSTRACT OF THE DISSERTATION

Synthesis and Optimization of Praseodymium Telluride System
Through Alloys and Composites

By

Brea Elizabeth Hogan

Doctor of Philosophy in Materials Science and Engineering
University of California, Los Angeles, 2023
Professor Bruce S. Dunn, Chair

Radioisotope Thermoelectric Generators (RTGs) provide electrical power for spacecraft by converting heat generated by the decay of plutonium-238 (Pu-238) into electricity. In missions such as Curiosity, the excess heat generated from an RTG can be used as a convenient and steady source of warmth to maintain proper operating temperatures for a spacecraft and its instruments in cold environments. While RTGs have been historically viewed as a highly reliable power option, current RTGs have relatively low system efficiencies on the order of 6%. This clearly highlights the need to concentrate research in this field to improve overall efficiencies. To accomplish this, vast improvements on thermoelectric materials are necessary for the success and longevity of future space emissions.

The figure of merit to determine the efficiency of thermoelectric materials is defined as $ZT=(\sigma S^2/\kappa)T$ where σ, S, κ, and T are electrical conductivity, Seebeck coefficient, thermal conductivity, and temperature, respectively. Rare earth chalcogenides with the Th_3P_4-type

structure (such as $La_{3-x}Te_4$) can accommodate vacancies on the rare earth site, leading to disorders and distortions in the lattice, and in turn enhanced phonon scattering. This ultimately results in a reduction in the lattice thermal conductivity of ~0.4-0.8 W/m-k. Previously reported optimized defect stoichiometry ($LaTe_{1.46}$) attained ZT=1.1 around 1275K. Previous research conducted at JPL indicates that improvements are seen within Pr_3Te_4 and Nd_3Te_4 compared to La_3Te_4, primarily due to the contribution of the *f*-states to the density of states near the Fermi level. This ultimately contributes to an improvement in Seebeck, and thus an improvement in ZT.

One of the main projects of this dissertation is to better understand the oxidation kinetics across RE_3Te_4 (RE = rare earth: La, Pr, Nd). Understanding kinetics for these materials using thermogravimetric analysis (TGA) will help us to further mitigate the effects of oxidation and improve the efficiencies of these materials for long-term, deep space missions. Research indicates that rare earth tellurides experience similar oxidation mechanisms, but at distinct rates. Pr_3Te_4 and Nd_3Te_4 oxidize kinetically faster compared to La_3Te_4, which would suggest there is less time for the formation of intermediate phases.

Another project discussed in this research is focused on the synthesis and characterization of thermoelectric systems with the potential for higher thermoelectric conversion efficiency such as $La_{3-x}RE_xTe_4$ (RE = Pr) to develop high-performance radioisotope thermoelectric generators. It is hypothesized that alloying in the $La_{3-x}Pr_xTe_4$ system will tune the DOS via f-electrons, which will help reduce thermal conductivity because of point defect scattering, and mechanical improvements will be seen via solid solution strengthening. The rule of mixtures was scientifically proven due to the alloy thermoelectric properties residing between the properties of the end members. Hardness measurements indicate that the end members and the alloys all have similar hardness values within error.

The final project is focused on understanding the CAFE (composite-assisted funneling of electrons) effect on $PrTe_{1.46}$ composites and their thermoelectric properties. Ni composites within $PrTe_{1.46}$ have not been previously investigated; thus, this research will discern how the CAFE effect exhibits itself within a Pr_3Te_4 matrix. It is hypothesized that a significant decrease in electrical resistivity will occur compared to $LaTe_{1.46}$-Ni composites, due to the improvement in *ZT* observed with $PrTe_{1.46}$ compared to $LaTe_{1.46}$. *ZT* values for 5% volume Ni increased the average *ZT*, while the 10% and 15% volume Ni resulted in an improvement in peak *ZT* at 1275K. The resultant increase cannot be attributed to the CAFE effect due to the Seebeck and resistivity coupling.

The dissertation of Brea Elizabeth Hogan is approved.

Sabah K. Bux

Yang Yang

Laura Kim

Tim Fisher

Bruce S. Dunn, Committee Chair

University of California, Los Angeles
2023

To my loving friends and family members: Thank you for being my continued source of support and love

TABLE OF CONTENTS

LIST OF FIGURES

LIST OF TABLES

ACKNOWLEDGEMENTS

I'm so incredibly thankful that I've been able to experience amazing research opportunities at two incredible institutions, UCLA and JPL. When I enrolled at Duquesne University as an undergrad, I did not ever expect that graduate school would take me to such amazing places. I'm so grateful to two amazing individuals in my life: Professor Bruce Dunn and Dr. Sabah Bux. Firstly, Professor Dunn – thank you so much for providing me with enough freedom to pursue my research and try new experiments, but with enough mentorship to make significant progress with my work. I will always remember when Dean first brought us together to discuss research, and when I invited my entire family over to your house. Thank you for continually encouraging me and for your continued support, both financially and emotionally.

Dr. Sabah Bux – what can I possibly say to thank you for everything that you have done for me? Any time that I was unsure of what to do, whether in my personal or professional life, you were always willing and able to provide priceless advice. I'm looking forward to you compiling all of your wisdom into a book! I immensely value our friendship, and I would not have had such confidence to move to LA if not for your wonderful support.

Thank you to my doctoral committee, Professor Yang Yang, Professor Laura Kim and Professor Tim Fisher, for your continued insight and support of my research.

I want to thank Dr. Jennifer Aitken and Dr. Tomislav Pintauer for growing my interest in materials characterization and for giving me my first taste of lab experience. Who knew that introducing me to Sabah at a guest speaker event would lead to this?

Thank you so much Mama Dean, for being such an incredible mentor and giving me so much insight into thermoelectric materials. I truly appreciate your friendship and research guidance. Thanks for making lab a fun space!

Thank you, Dr. Jean-Pierre Fleurial, for giving me unrestricted access to JPL's labs. Thank you Billy Li! It took many trials and errors to figure out all of the new instrumentation, so I thank you for your patience. Thank you, George Nakatsukasa, for sharing your wealth of knowledge with me. Thank you, Greg Gerig, for our wonderful conversations, I'm looking forward to you publishing your short stories!

Thank you Dr. Fivos Drymiotis, Dr. Kurt Star, Prof. Eric Toberer at the Colorado School of Mines, Prof. Alexandra Zevalkink at Michigan State, Prof. Susan Kauzlarich at UC Davis, Prof. Jeff Snyder at Northwestern, and Dr. Christofer Whiting at UDRI for listening to my numerous research updates and providing insight into future work.

Special thanks to all other members in the JPL thermoelectrics group: Dr. Ike Chi, Araseli Cortez, Duncan Zalvanelli, Dr. Chris Perez, Dr. Andy Justl, Dr. Paul Von Allmen, Dr. Trinh Vo, Professor David Dunand, Professor Richard Blair, Allison Garavito Alex Proschel, Yunjia Zhang, Alan Fung, Professor Shahab Derakhshan, Leah Webb, Bavley Mobarak, Patrick Pham, Ming Chen. I'm very thankful for your conversations, and I wish you all the best in your future endeavors.

I would be remiss not to mention my past and more recent UCLA lab mates: Dr. Patricia McNeil, Dr. Danielle Butts, Dr. Chris Choi, Dr. Grace Whang, Dr. Ryan DeBlock, Dr. Chun-Han Lai, Yunkai Luo, Randy Chen, Jacky Yu, Bintao Hu, Winnie Hsieh, Mingyu Jung, Justin Huang, Makena White, Henry Choi, Peter Cao, Kyle Kotanchek, and Kyle Fujisaka. I appreciate all of our shenanigans and

Thank you, Maggie Fox, for being such an incredible friend! We joined and finished graduate school together, and you made it such a memorable experience. Special shout-out to

Alexander Cheikh! You were not only essential for my experimental research to succeed (especially with regards to TGA measurements), but your friendship is immensely invaluable.

Thank you to IBM, the GEM fellowship and all of my lab mates in Fishkill! I gained so much industrial insight from you all, and I would not had had the same graduate school experience without your financial support.

I reserve the greatest thanks for my family, those who are still living and those who have passed away. To Chris, Meme, Danielle, and my parents, I'm so thankful that you are a part of my life and continue to encourage me in my wild endeavors, even if it takes me across the country. Pittsburgh will always be in my heart!

Thank you to all of the volunteers at GCGP (Good Clothes Good People) for providing me with a community outside of research. I have seen the organization build itself up over the past 5 years, and I am forever indebted to everyone for their friendship and support.

All of the research in Chapter 2, 3, and 4 was a collaborative effort conducted at JPL and UCLA. Measurements of Seebeck coefficient were performed by Greg Gerig. Measurements of thermal diffusivity were performed by George Nakatsukasa. Dr. Bux and Professor Dunn were co-principal investigators and provided input for research experiments and writing/preparation of the manuscript. Dr. Trinh Vo and Dr. Paul von Allmen contributed to the computational modelling presented in this work. Dr. Chi Ma assisted with SEM training and analysis. TGA measurements were conducted by Dr. Alexander Cheikh.

This work was performed at the California Institute of Technology/Jet Propulsion Laboratory under contract with the National Aeronautics and Space Administration. This work was supported by the NASA Science Missions Directorate under the Radioisotope Power Systems Program's Thermoelectric Technology Development Project.

VITA

Duquesne University Pittsburgh, PA

BA, *cum laude*, Biochemistry 2017
Minor: Biology

Thesis: Synthesis and Physicochemical Characterization
of Ternary Diamond-like Tellurides: Cu_2GeTe_3 and $Cu_5Ge_2Te_7$

Duquesne University Pittsburgh, PA
MS, Forensic Science and Law 2018

Thesis: Synthesis and Physicochemical Characterization
of Semiconductors for Latent Fingerprint Identification

University of California, Los Angeles Los Angeles, CA
Graduate Student, PhD Materials Science and Engineering 2018-2023

SELECTED CONFERENCE PRESENTATIONS

Hogan, B.E., Cheikh, D.A., Vo, T., Allmen, P.V., Aitken, J.A., Dunn, B.S., Fleurial, J.-P., and Bux, S.K. Low-Temperature synthesis and thermoelectric performance of praseodymium telluride $Pr_{3-x}Te_4$ series. Poster presentation delivered at the 36th International Conference on Thermoelectrics, Pasadena, CA, August 2017.

Hogan, B.E. and Aitken, J.A. Synthesis and physicochemical characterization of narrow-bandgap telluride containing earth-abundant elements. Poster presentation delivered at the 251st American Chemical Society meeting, San Diego, CA, March 2016.

Hogan, B.E. and Aitken, J.A. New phase discovered in the Cu-Ge-Te system by high-temperature solid state reaction. Poster presentation delivered at the 249th American Chemical Society meeting, Denver, CO, March 2015.

PEER REVIEWED PUBLICATIONS

Male, J.P., **Hogan, B.**, Wood, M., Cheikh, D., Snyder, G.J., Bux, S.K. (2023). Using vacancies to tune mechanical and elastic properties in $La_{3-x}Te_4$, $Nd_{3-x}Te_4$, and $Pr_{3-x}Te_4$ rare earth telluride thermoelectric materials. Materials Today Physics. https://doi.org/10.1016/j.mtphys.2023.101016

Pohls, J.-H., Chanakian, S., Park, J., Ganose, A.M., Dunn, A., Friesen, N. Bhattacharya, A. **Hogan, B.**, Bux, S., Jain, A., Mar, A., Zevalkink, A (2021). Experimental validation of high thermoelectric performance in $RECuZnP_2$ predicted by high-throughput DFT calculations. Materials Horizons. https://doi.org/10.1039/d0mh01112f

Cheikh, D.A., **Hogan, B.E.**, Vo, T., Allmen, P.V., Lee, K., Smiadak, D.M., Zevalkink, A., Dunn, B.S., Fleurial, J.-P., and Bux, S.K. (2018). Praseodymium telluride: a high-temperature, high-*ZT* thermoelectric material. Joule. https://doi.org/10.1016/j.joule.2018.01.013

Chapter 1: Introduction to Thermoelectric Materials and Applications

1.1. Thermoelectric Principles and Strategies for Improvement

Thermoelectric materials have the specific capacity of either converting a heat flux into electrical power output (Seebeck effect) or producing a temperature gradient in a direction perpendicular to an electric current (Peltier effect). Such direct energy conversion is attractive for recovering a portion of waste heat from a variety of commercial and space applications, such as transportation vehicles, microelectronics and low-power applications like wrist watches.[1-2] The configurations of power generation (Seebeck) and heating/cooling (Peltier) can be seen in Figure 1.1. To maximize efficiency, *n*-type and *p*-type legs are placed electrically in series and thermally in parallel. In the power generation system, a heat source provides the energy needed to drive the majority charge carriers on both the *n*-type and *p*-type legs of the thermocouple; this current is then applied to an external load.

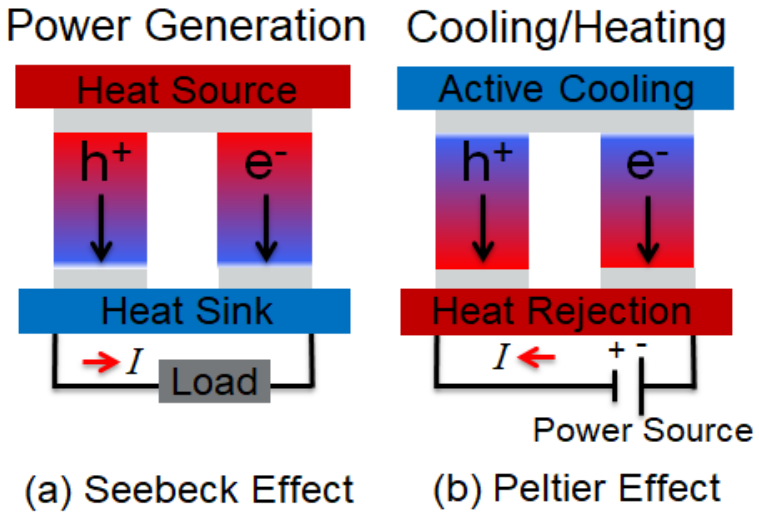

Figure 1.1. Schematic of thermoelectric couples with *n*-type (electron (e^-) charge carriers) and *p*-type (hole (h^+) charge carriers) for power generation (left) and heating/cooling (right).

Alternatively, in a cooling/heating system, a power source applied a current to the thermocouple, thus generating a temperature gradient. The focus of this project will be on the thermoelectric materials applied to power generation systems.

The Carnot efficiency equation is utilized to determine the maximum efficiency of a thermoelectric generator:

$$\eta = \frac{T_h - T_c}{T_h}\left(\frac{\sqrt{1+ZT}-1}{\sqrt{1+ZT}+\frac{T_c}{T_h}}\right) \quad \textbf{Equation 1.1}$$

In the conventional thermoelectric configuration (as shown in Figure 1.1), both the hot-side heat source (T_h) and cold side rejection radiator (T_c) operate at constant temperature. The Carnot efficiency also includes a dimensionless figure-of-merit, *ZT*, which can be further defined in the following equation:

$$ZT = \frac{\sigma\alpha^2}{\kappa}T \quad \textbf{Equation 1.2}$$

where electrical conductivity (σ), Seebeck coefficient (α), thermal conductivity (κ) and temperature (T) all play an important role in assessing *ZT*. The device efficiency with a cold side temperature of 50°C is plotted for various *ZT* values in Figure 1.2.[2] It can be seen that efficiency increases with *ZT* and as *ZT* increases to infinity, the device efficiency approaches the Carnot efficiency.

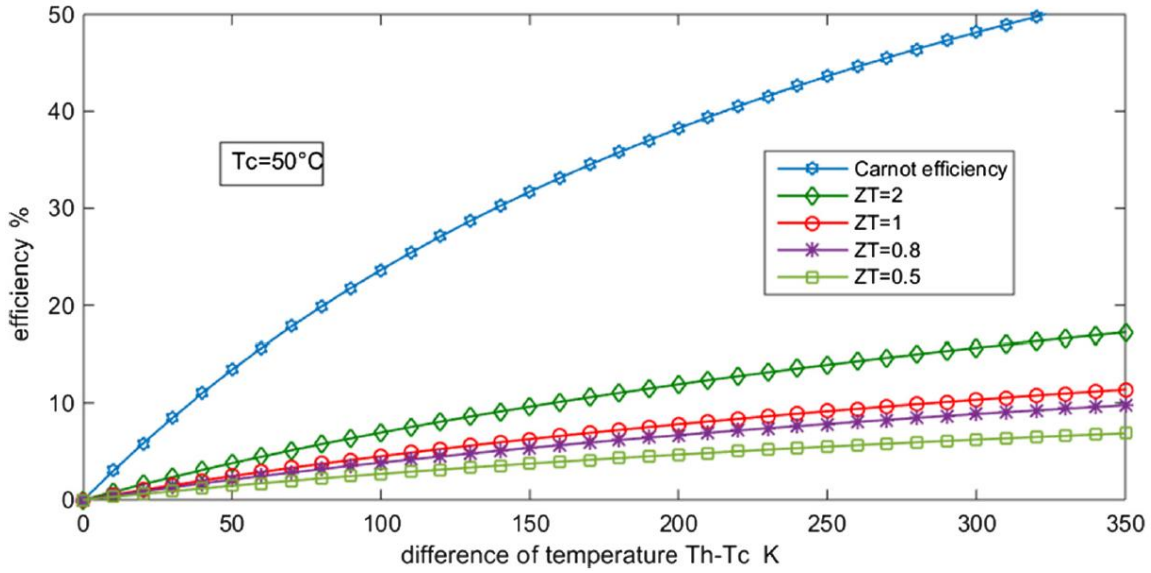

Figure 1.2. Typical values of thermoelectric efficiency for different values of ZT[2]

In order to increase the total device efficiency, ZT must be increased or the Carnot efficiency must be increased (Equation 1.1). Increasing the Carnot efficiency is challenging due to practical constraints on thermoelectric generators, e.g., limits to the operating temperatures of the hot and cold sides and material constraints due to melting or decomposition temperatures of the thermoelectric materials.[3-4]

In general, ZT also depends on the exact temperature-dependent material properties, exact geometry, including non-ideal circumstances such as electrical and thermal losses (e.g., contact resistances, parasitic losses) and non-optimized geometric parameters. However, for the sake of simplicity we are solely focusing on optimizing the efficiency of thermoelectric materials under ideal circumstances (i.e. all other parameters are optimized).[4]

Increasing the efficiency of thermoelectric materials according to the *ZT*, however, poses an interesting challenge because all of the variables are correlated, as shown in Figure 1.3.[5] One of the most well-known and intuitive conflicts is between the electrical conductivity and Seebeck coefficient, and their relation to carrier concentration.

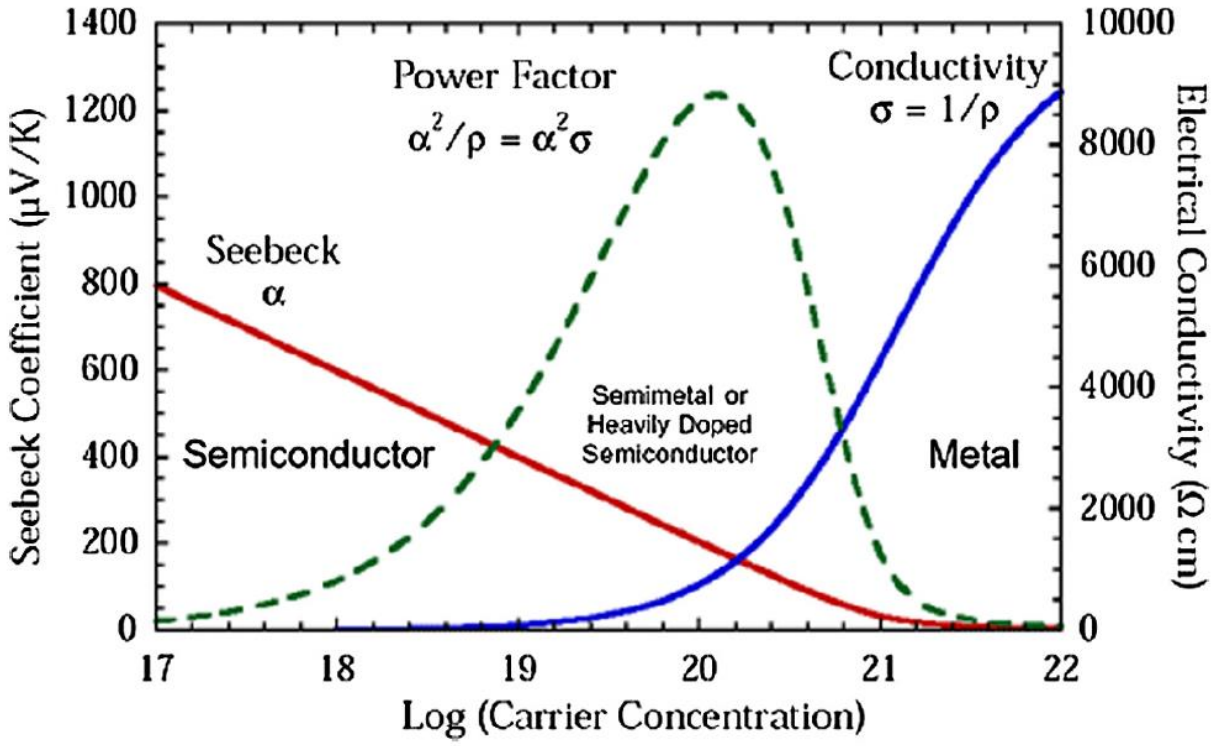

Figure 1.3. Variation of *ZT* parameters as a function of carrier concentration[5]

The electrical and thermal conductivity increase with carrier concentration, while the Seebeck coefficient (α) decreases with increasing carrier concentration. Thus, it's important to optimize all properties so that the average *ZT* of the materials is improved.[6-10] Let's take a deeper

dive into how to optimize each parameter, starting with the Seebeck coefficient. The Mott relation for the Seebeck coefficient is presenting in the following equation:

where T is the temperature, n(E) is the carrier density at energy E, μ(E) is the mobility at energy E, E_F is the fermi energy, and q is the electronic charge.

$$\alpha = \frac{\pi^2}{3}\frac{k_B}{q}k_B T\left(\frac{1}{n}\frac{dn(E)}{dE} + \frac{1}{\mu}\frac{d\mu(E)}{dE}\right)_{E=E_F} \quad \textbf{Equation 1.3}$$

The Seebeck coefficient depends on the absolute temperature, composition, charge-carrier concentration and crystal structure of the thermoelectric material. Since Seebeck depends on both bandgap and carrier concentration, there are two primary strategies to optimizing this parameter: (i) increasing the energy dependence of μ(E) by a scattering mechanism that is strongly dependent on the charge carriers and (ii) increasing the energy dependence of n(E) by a local increase in the density of states (DOS).[11-12]

The dependence of the electrical conductivity (σ) of a semiconductor on carrier concentration and mobility is given by:

$$\sigma = e(\mu_e n + \mu_h p) \quad \textbf{Equation 1.4}$$

where μ_e, μ_h, n and p denote the electron mobility, hole mobility, density of electrons, and density of holes, respectively. Lattice and impurity scattering determine the mobility of the charge carriers. At lower temperatures, impurity scattering dominates, ultimately resulting in a decrease in mobility. As the temperature increases, lattice vibrations increase which decreases mobility.[13-14]

Thermal conductivity is a sum of two contributions: charge carriers and phonons. When one type of charge carrier is predominant, the total thermal conductivity is attributed to the sum of the lattice ($K_{lattice}$) and charge-carrier (K_c) contributions, that is:

$$\kappa = \kappa_c + \kappa_{lattice} \quad \textbf{Equation 1.5}$$

A lower thermal conductivity can be attained by lowering the lattice thermal conductivity. The charge-carrier thermal conductivity can be estimated from the Wiedemann-Franz law ($K_c=L\sigma T$), where L is the Lorenz constant.

The lattice thermal conductivity can be expressed as the following equation:

$$\kappa_c = DC_p\rho \quad \textbf{Equation 1.6}$$

where D is the thermal diffusivity, Cp is the specific heat, and p is the density of the material. Thus, the thermal conductivity is strongly affected by phonons, which are generated from the lattice vibrations. The lattice contribution depends on the crystal structure and lattice parameters of the material.[15-16]

A good thermoelectric material is characterized by a large Seebeck coefficient to produce the thermoelectric voltage, a low thermal conductivity for limiting the dissipative Fourier heat flow throughout the device exposed to a temperature gradient, and a high electrical conductivity to minimize Joule heating. This configuration, where thermocouples are connected electrically in series and thermally in parallel, is appropriate for space technology applications.

1.2. Heritage Materials for Space Technologies

One of the original and most successful uses of thermoelectric heat engines has been primary electric power generation for spacecraft. The thermoelectric generators (TEGs) developed in the United States and the former USSR dominated energy conversion for spacecraft operating beyond the effective range of sun-powered photovoltaic cells.[17-19] They exhibit compact design, exceptional durability, and stable power output over decades. The lower efficiency of these systems has been outweighed by the positive characteristics, such as continuous primary electric power production for remote communications and control system applications.

Radioisotope Thermoelectric Generators (RTGs) provide electrical power for spacecraft by converting heat generated by the decay of plutonium-238 (Pu-238) into electricity. In missions such as Curiosity, the excess heat generated from an RTG can be used as a convenient and steady source of warmth to maintain proper operating temperatures for a spacecraft and its instruments in cold environments.[20] Since they have no moving parts that can fail or wear out, RTGs have been historically viewed as a highly reliable power option. Earlier generations of RTGs have been utilized as power systems for Voyager 1 & 2, Cassini-Huygens, New Horizons, and Curiosity.[21]

However, current RTGs for these missions have relatively low system efficiencies on the order of 6%.[22] As mission concepts and spacecraft become more sophisticated, the demand for higher specific power (W/kg) increases.[23] This clearly highlights the need to concentrate research in this field to improve the overall efficiency. To accomplish this, vast improvements on thermoelectric materials are necessary for the success and longevity of future space emissions.

Historically, PbTe and Si-Ge alloys have proven to be sufficient for thermoelectric power generation; however, newer materials can provide greater improvements in *ZT*, as seen in Figure 1.4.[24]

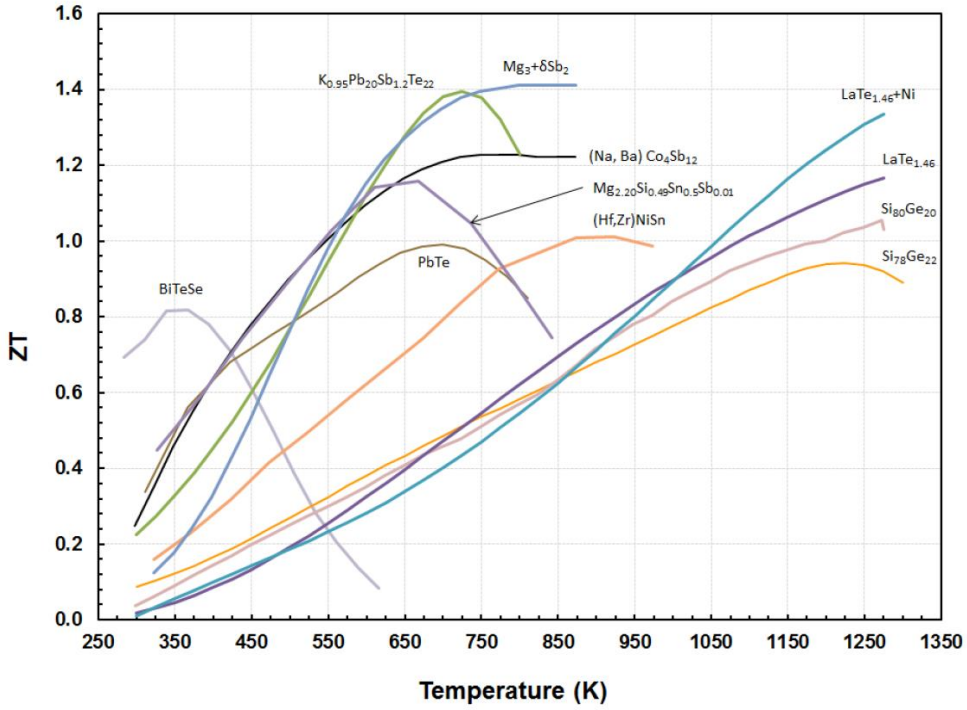

Figure 1.4. Figure of merit (*ZT*) for various *n*-type thermoelectric materials across a wide temperature range[24]

This figure highlights the improvement in average *ZT* seen in systems such as $LaTe_{1.46}$ and Ni composites. Previous research has gone into studying the enhanced properties of this system, which are intrinsically tied to its Th_3P_4 structure type.

1.3. RE_3Te_4 (RE = La, Pr, Nd) as Thermoelectric Materials

Rare earth chalcogenides can be observed with the Th_3P_4-type structure. In this structure, using La_3Te_4 as an example, Te atoms at the P sites can experience a six-fold coordination with La atoms, producing a distorted octahedral structure, as shown in Figure 1.5.[25-27]

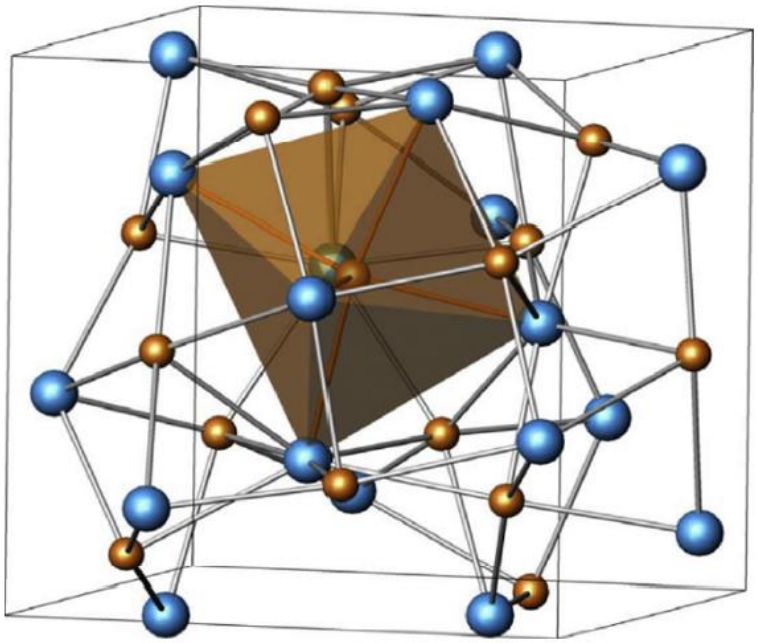

Figure 1.5. Crystal structure of $La_{3-x}Te_4$. Lanthanum atoms are represented by blue spheres and Tellurium atoms by brown spheres

The resulting structure accommodates vacancies on the rare earth site, leading to disorders and distortions in the lattice, and in turn enhanced phonon scattering. This ultimately results in a reduction in the lattice thermal conductivity of ~0.4-0.8 W/m-k. Snyder et al. studied the effects of carrier and doping concentration on the thermoelectric properties of the $La_{3-x}Te_4$ system.[28] They reported that, when x=0 (La_3Te_4), the material behaves as a degenerate semiconductor and the electronic properties are metallic. When x=0.33 ($La_{2.667}Te_4$, also written as La_2Te_3 or $LaTe_{1.5}$), the material acts as an intrinsic semiconductor. Previously reported optimized defect stoichiometry ($LaTe_{1.46}$) attained ZT=1.1 around 1275K.

Previous research conducted at JPL indicates that improvements are seen within Pr_3Te_4 and Nd_3Te_4 compared to La_3Te_4, primarily due to the contribution of the *f*-states to the density of states near the Fermi level. This ultimately contributes to an improvement in Seebeck, and thus an improvement in *ZT* as seen in Figure 1.4.[29]

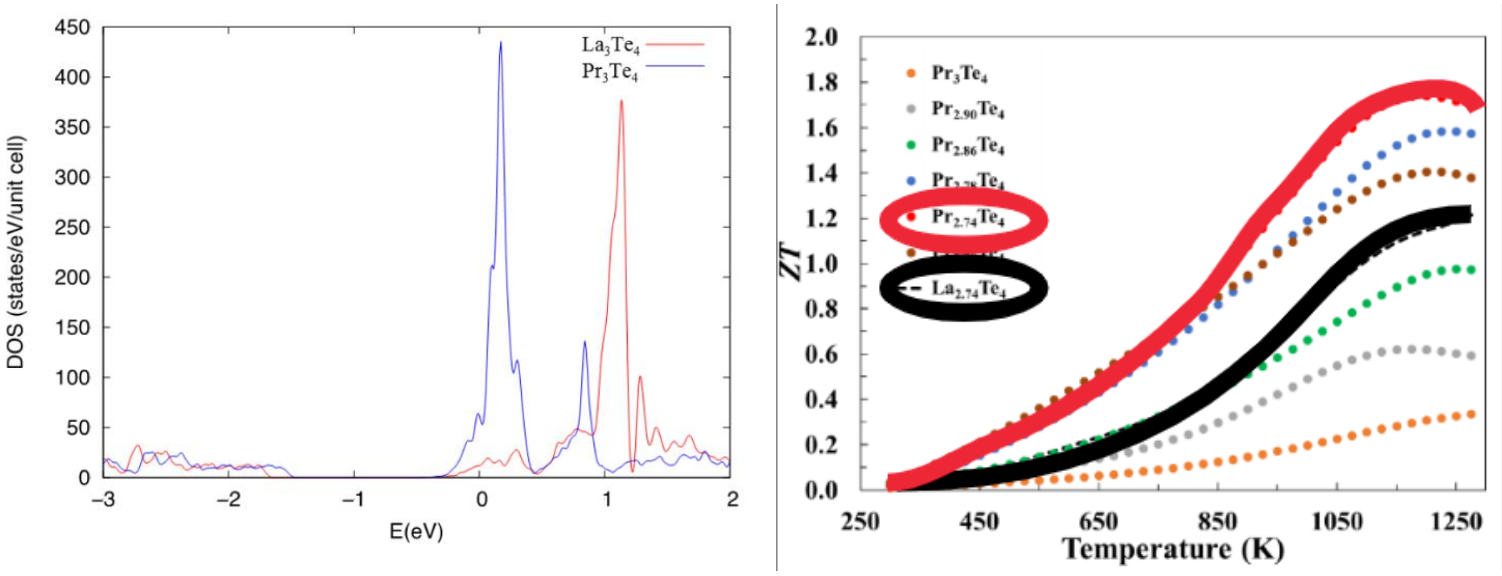

Figure 1.6. Density of states (DOS) for Pr_3Te_4 and La_3Te_4 showing a difference in contribution of *f*-states (left) and comparison of *ZT* for optimized $LaTe_{1.46}$ and the $Pr_{3-x}Te_4$ series (right)

1.4. Dissertation Objectives

One of the main projects of this dissertation is to better understand the oxidation kinetics across RE_3Te_4 (RE = rare earth: La, Pr, Nd). No previous research has been conducted to investigate the potential distinctions in oxidation kinetics across rare earth tellurides. Understanding kinetics for these materials will help us to further mitigate the effects of oxidation and improve the efficiencies of these materials for long-term, deep space missions.

Another project discussed in this research is focused on the synthesis and characterization of thermoelectric systems with the potential for higher thermoelectric conversion efficiency such

as $La_{3-x}RE_xTe_4$ (RE = Pr) to develop high-performance radioisotope thermoelectric generators. It is hypothesized that alloying in the $La_{3-x}Pr_xTe_4$ system will tune the DOS via f-electrons, which will help reduce thermal conductivity because of point defect scattering.

The final project is focused on understanding the CAFE (composite-assisted funneling of electrons) effect on $PrTe_{1.46}$ composites and their thermoelectric properties. Ni composites within $PrTe_{1.46}$ have not been previously investigated; thus, this research will discern how the CAFE effect exhibits itself within a Pr_3Te_4 matrix. It is hypothesized that a significant decrease in electrical resistivity will occur compared to $LaTe_{1.46}$-Ni composites, due to the improvement in *ZT* observed with $PrTe_{1.46}$ compared to $LaTe_{1.46}$.

1.5. References

[1] Hamid Elsheikh, M.; Shnawah, D. A.; Sabri, M. F. M.; Said, S. B. M.; Haji Hassan, M.; Ali Bashir, M. B.; Mohamad, M. A Review on Thermoelectric Renewable Energy: Principle Parameters That Affect Their Performance. *Renewable and Sustainable Energy Reviews* **2014**, *30*, 337–355. https://doi.org/10.1016/j.rser.2013.10.027

[2] Champier, D. Thermoelectric Generators: A Review of Applications. *Energy Conversion and Management* **2017**, *140*, 167–181. https://doi.org/10.1016/j.enconman.2017.02.070

[3] Zhu, T.; Liu, Y.; Fu, C.; Heremans, J. P.; Snyder, J. G.; Zhao, X. Compromise and Synergy in High-Efficiency Thermoelectric Materials. *Advanced Materials* **2017**, *29*, 30-38. https://doi.org/10.1002/adma.201702816

[4] Zhang, X.; Zhao, L.-D. Thermoelectric Materials: Energy Conversion between Heat and Electricity. *Journal of Materiomics* **2015**, *1*, 92–105. https://doi.org/10.1016/j.jmat.2015.01.001

[5] Gayner, C., and Kar, Kamal K. Recent Advances in Thermoelectric Materials. *Progress in Materials Science* **2016**, *83*, 330-382. https://doi.org/10.1016/j.pmatsci.2016.07.002

[6] LeBlanc, Saniya. Thermoelectric Generators: Linking Material Properties and Systems Engineering for Waste Heat Recovery Applications. *Sustainable Materials and Technologies* **2014**, *1*, 26–35, https://doi.org/10.1016/j.susmat.2014.11.002

[7] Chen, Renkun, et al. Thermoelectrics of Nanowires. *Chemical Reviews* **2019**, *15*, 9260–302, https://doi.org/10.1021/acs.chemrev.8b00627

[8] Gayner, Chhatrasal, and Kamal K. Kar. Recent Advances in Thermoelectric Materials. *Progress in Materials Science* **2016**, *83*, 330–82, https://doi.org/10.1016/j.pmatsci.2016.07.002

[9] Kim, Tae Young, et al. Direct Contact Thermoelectric Generator (DCTEG): A Concept for Removing the Contact Resistance between Thermoelectric Modules and Heat Source. *Energy Conversion and Management* **2017**, *142*, 20–27, https://doi.org/10.1016/j.enconman.2017.03.041

[10] He, Ran, et al. Thermoelectric Devices: Thermoelectric Devices: A Review of Devices, Architectures, and Contact Optimization. *Advanced Materials Technologies* **2018**, *3*, 1870016, https://doi.org/10.1002/admt.201870016

[11] Yang, Lei, et al. High Performance Thermoelectric Materials: Progress and Their Applications. *Advanced Energy Materials* **2017**, *8*, 1701797, https://doi.org/10.1002/aenm.201701797

[12] Zeier, Wolfgang G., et al. Thinking Like a Chemist: Intuition in Thermoelectric Materials. *Angewandte Chemie International Edition* **2016**, *55*, 6826–41, https://doi.org/10.1002/anie.201508381

[13] Liu, Weishu, et al. New Trends, Strategies and Opportunities in Thermoelectric Materials: A Perspective. *Materials Today Physics* **2017**, *1*, 50–60, https://doi.org/10.1016/j.mtphys.2017.06.001

[14] Mao, Jun, et al. Advances in Thermoelectrics. *Advances in Physics* **2018**, *2*, 69–147, https://doi.org/10.1080/00018732.2018.1551715

[15] Rowe, David Michael. *Materials, Preparation, and Characterization in Thermoelectrics* **2017**, CRC Press.

[16] Chen, Zhiwei, et al. Manipulation of Phonon Transport in Thermoelectrics. *Advanced Materials* **2018**, *30*, 17. https://doi.org/10.1002/adma.201705617

[17]: Tailin, Youhong *et al,* "Comprehensive modeling and characterization of Chang'E-4 radioisotope thermoelectric generator for lunar mission", *Applied Energy* **2023**, *336*. https://doi.org/10.1016/j.apenergy.2023.120865

[18]: Freis, Vigier *et al*, "Exploratory Research on Radioisotope Thermoelectric Generators for Deep Space Missions", *E3S Web of Conferences* **2017**, *16*, 5001–. https://doi.org/10.1051/e3sconf/20171605001

[19]: Holgate, Bennett *et al*, "Increasing the Efficiency of the Multi-mission Radioisotope Thermoelectric Generator", *Journal of Electronic Materials* **2015**, *44*(6), 1814–1821. https://doi.org/10.1007/s11664-014-3564-9

[20]: Salh, H.M., "Improving the Overall Efficiency of Radioisotope Thermoelectric Generators", *Advances in Energy and Power* **2014**, 2(3), 21-26. https://doi.org/10.13189/aep.2014.020301

[21] Yang, Jihui, and Thierry Caillat. Thermoelectric Materials for Space and Automotive Power Generation. *MRS Bulletin* **2006**, *3*, 224–29, https://doi.org/10.1557/mrs2006.49

[22] Holgate, Tim C., et al. Increasing the Efficiency of the Multi-Mission Radioisotope Thermoelectric Generator. *Journal of Electronic Materials* **2014**, *6*, 1814–21, https://doi.org/10.1007/s11664-014-3564-9

[23] Pantano, David, et al. Utilizing Radioisotope Power System Waste Heat for Spacecraft Thermal Management. *3rd International Energy Conversion Engineering Conference* **2005**, American Institute of Aeronautics and Astronautics, http://dx.doi.org/10.2514/6.2005-5548

[24] Matthes, Christopher S. R., et al. Next-Generation Radioisotope Thermoelectric Generator Study *2018 IEEE Aerospace Conference*, http://dx.doi.org/10.1109/aero.2018.839673

[25] May, Andrew, et al. Lanthanum Telluride: Mechanochemical Synthesis of a Refractory Thermoelectric Material. *AIP Conference Proceedings* **2008**, AIP, http://dx.doi.org/10.1063/1.2845029

[26] Khan, Muhammad Rizwan, et al. Fermi-Level Instability as a Way to Tailor the Properties of La3Te4. *The Journal of Physical Chemistry Letters* **2023**, *7*, 1962–67, https://doi.org/10.1021/acs.jpclett.2c03701

[27] May, Andrew F., David J. Singh, et al. Influence of Band Structure on the Large Thermoelectric Performance of Lanthanum Telluride. *Physical Review B* **2009**, *15*, https://doi.org/10.1103/physrevb.79.153101

[28] May, Andrew F., et al. Thermoelectric Performance of Lanthanum Telluride Produced via Mechanical Alloying. *Physical Review B* **2008**, *12*, https://doi.org/10.1103/physrevb.78.125205

[29] Cheikh, Dean, Hogan, Brea *et al*, Praseodymium Telluride: A High-Temperature, High *ZT* Thermoelectric Material, *Joule* **2018**, *2*, https://doi.org/10.1016/j.joule.2018.01.013

Chapter 2: Oxidation Study of RE_3Te_4 (RE = La, Pr, Nd)

2.1. Introduction

Radioisotope thermoelectric generators (RTGs) have a proven track record of reliability in space applications with over 30 years of continuous service as implemented in the Voyager 1 and 2 missions. The need for a robust power system able to support a broader scope of future planetary missions has prompted the investigation of currently available RTG systems. These systems, referred to as multi-mission radioisotope thermoelectric generators (MMRTGs), were designed for both vacuum and atmospheric environments. This is a significant improvement over previous RTGs which could only operate in the vacuum of space.

Previous research has been conducted to best understand the radiation environments and exposure considerations for MMRTGs. Throughout generator operation at high temperatures, research indicates that the aerogel in the thermoelectric module produces non-inert outgassing products, including oxides.[1] The presence of these non-inert gases (including oxides) may result in undesirable interactions with system-level materials. To mitigate aerogel outgassing, Zr getters and different types of aerogels were implemented into the system. They have been shown to be effective at mitigating gas formation (including CO, CO_2, CH_4 and H_2O); however, even a small percentage of these gases could have detrimental effects on the thermoelectric materials.[2] Thus, the overall reliability of MMRTG's can be affected by the vaporization of the thermoelectric module and insulation residual outgassing.[3] To further understand and potentially mitigate the effects of oxidation exposure, especially for longer-term missions, it is imperative to understand the oxidation kinetics and mechanisms of thermoelectric materials.

Research regarding oxidation kinetics has been conducted in the $Yb_{14-x}RE_xMnSb_{11}$ system.[4] For this study, thermogravimetric curves as a time function of increasing mass were recorded, and kinetic characteristics of oxidation were calculated for the solid solutions. Significant differences were seen across different rare earths, indicating the impact of periodic trends on oxidation kinetics as well. This and similar research studies served as the foundation for this work, primarily due to the success of calculating parabolic kinetics and how that provides insight into understanding the mechanism as well.

Thus, the purpose of this study is to better understand the oxidation kinetics and mechanisms of rare earth tellurides (primarily Pr_3Te_4 and Nd_3Te_4 as they compare to La_3Te_4). From a qualitative perspective, it has been noted that these materials are especially prone to oxidation; however, a quantitative analysis had not been explored in depth previously. Previous work conducted at JPL by Chris Whiting (private communication) and Alexander Cheikh indicates that, in the case of oxidation of La_3Te_4, there are intermediary "glassy" phases formed in a unique mechanism they proposed.[5] Based on the differences across RE_3Te_4 in terms of electronic properties, it is hypothesized that there will be distinct differences for RE_3Te_4 in terms of oxidation mechanisms and kinetics as well, potentially as a result of differences in activation energy and formation rates of different rare earth oxides. Thus, periodic trends should have a significant impact on oxidation kinetics of rare earth tellurides.

2.2. Experimental

For this study, a variety of RE_3Te_4 (RE = La, Pr, Nd) samples were made using a previously reported mechanochemical synthesis procedure.[6] All preparation steps were performed in argon dry glove boxes (H2O < 1 ppm, O2 < 0.1 ppm). The materials were prepared based on targeted stoichiometric compositions using the corresponding elements (La, 99.9%, metals basis, HEFA Rare Earth; Pr, 99.9%, metals basis, Stanford Advanced Materials; Nd, 99.9%, metals basis, HEFA Rare Earth; Te, 99.9%, 5N Plus). The elements were combined in a stainless-steel vial with ½'' stainless steel balls. The vials were placed in a ball mill (SPEX SamplePrep 8000) and the sample was mechanochemically milled for over 10 hours until a homogeneous powder was synthesized. The powder was then loaded into 12.7 mm graphite dies and compacted using spark plasma sintering (SPS) at a pressure of 80 MPa and at temperatures above 1,200℃ for 30 min under vacuum. The sintered, compacted samples had densities greater than 98% of the theoretical density, measured using the Archimedes method.

Thermo Scientific Lindberg/Blue M Mini-Mite tube furnaces were used in air to expose the rare earth telluride samples to oxidation. The samples were polished and placed into alumina boats in the furnace. The following heating profile was used (as seen in Figure 2.1): starting at room temperature, the furnace temperature was increased to the max temperature of 500℃ at a rate of 1.5°/min. The temperature was held at 500℃ for 30 mins, then cooled down to room temperature ambiently.

A Zeiss 1550 VP SEM was used to perform scanning electron microscopy (SEM) on the $NdTe_{1.42}$ sample. Line scans were performed within 70μm on the front and back of the cross-section of the sample to determine the levels of Nd, Te and O present. X-ray diffraction (XRD)

data was collected with a Phillips PANalytical X'Pert Pro diffractometer using Cu Kα radiation on sintered, compacted samples. Scans were performed from 10-70°2Θ at a rate of 1°/min.

An Instrument Specialists Inc. Thermal Gravimetric Analysis (TGA) was conducted at UCLA to measure the mass change with respect to temperature and time, thus helping us to understand the oxidation kinetics and mechanisms of the materials. The following heating profile was used (as seen in Figure 2.7): the system was purged with air for 30 minutes at room temperature to remove any residual argon from any previous runs; the air purge rate was 20 ml/min. Then the furnace temperature was increased to the max temperature of 900°C at a rate of 5°/min. The temperature was held at 900°C for 30 mins, then cooled down to room temperature ambiently.

2.3. Results and Discussion

Tube furnace measurements were collected at JPL to determine the oxidation phases of RE_3Te_4. The compact samples were oxidized according to the following heating profile:

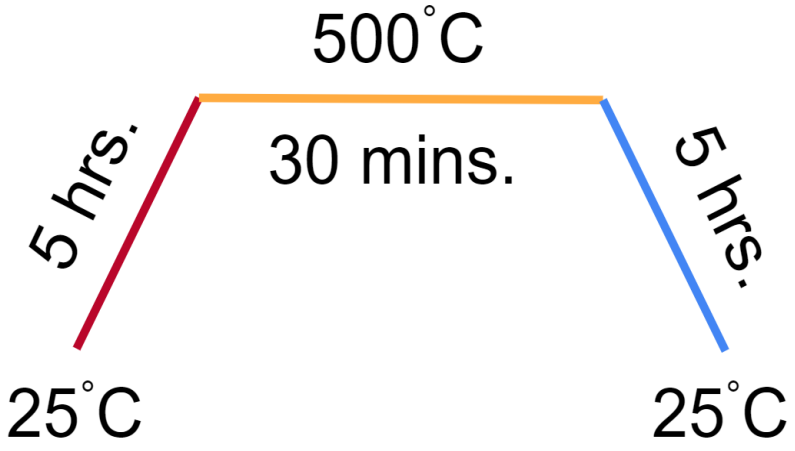

Figure 2.1. Heating Profile for tube furnace experiments for RE_3Te_4

Four samples were heated in the initial experiment: $PrTe_{1.33}$, $LaTe_{1.33}$, $NdTe_{1.33}$ and $NdTe_{1.42}$. While the samples were initially densified and compacted, most of the samples decomposed into a powder state, as seen in Figure 2.2.

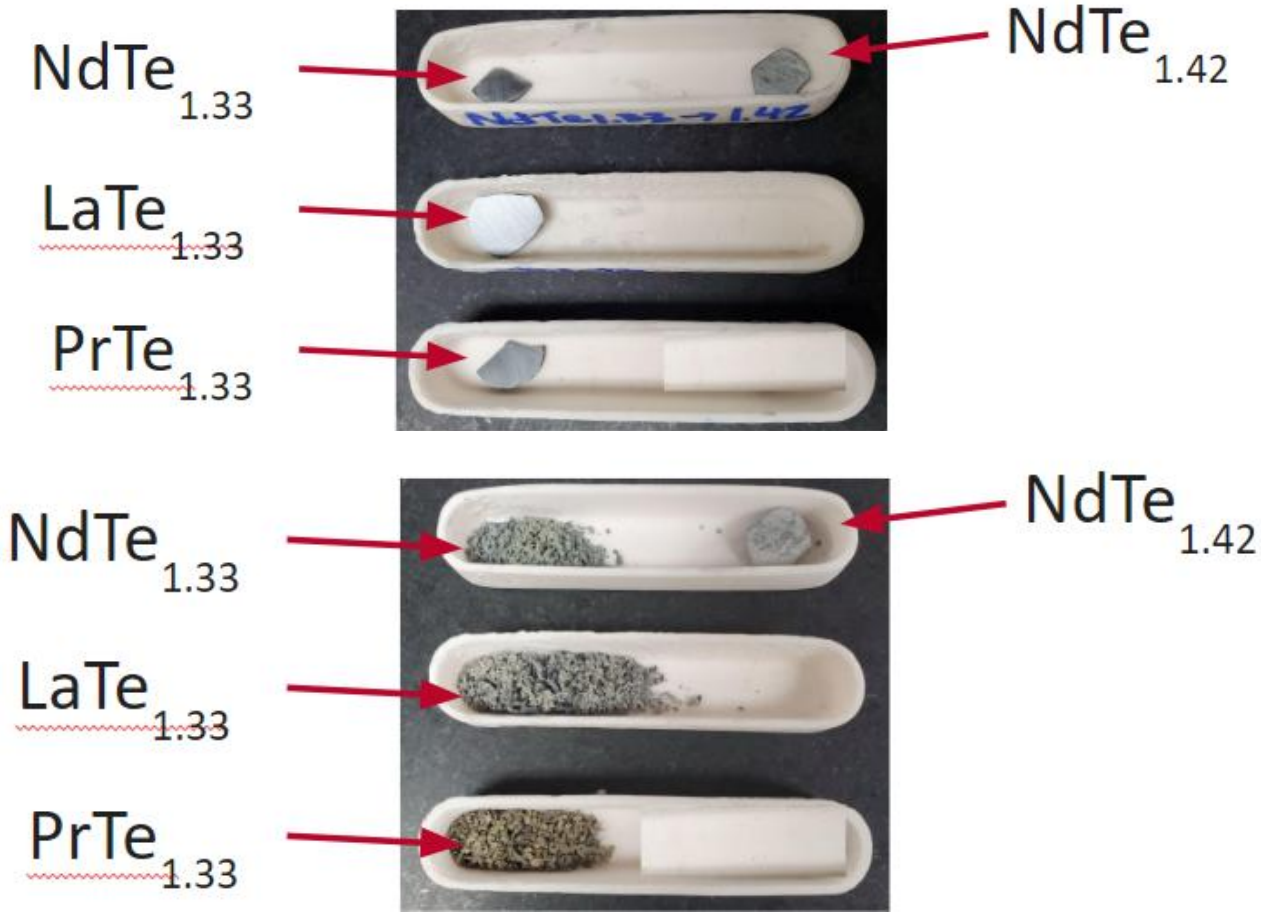

Figure 2.2. Images of various samples before (top) and after (bottom) tube furnace heating profile completed

All samples were characterized by XRD both before and after heat treatment, as seen in Figures 2.3 and 2.4. Both figures list the identified phases on the right next to the associated scan.

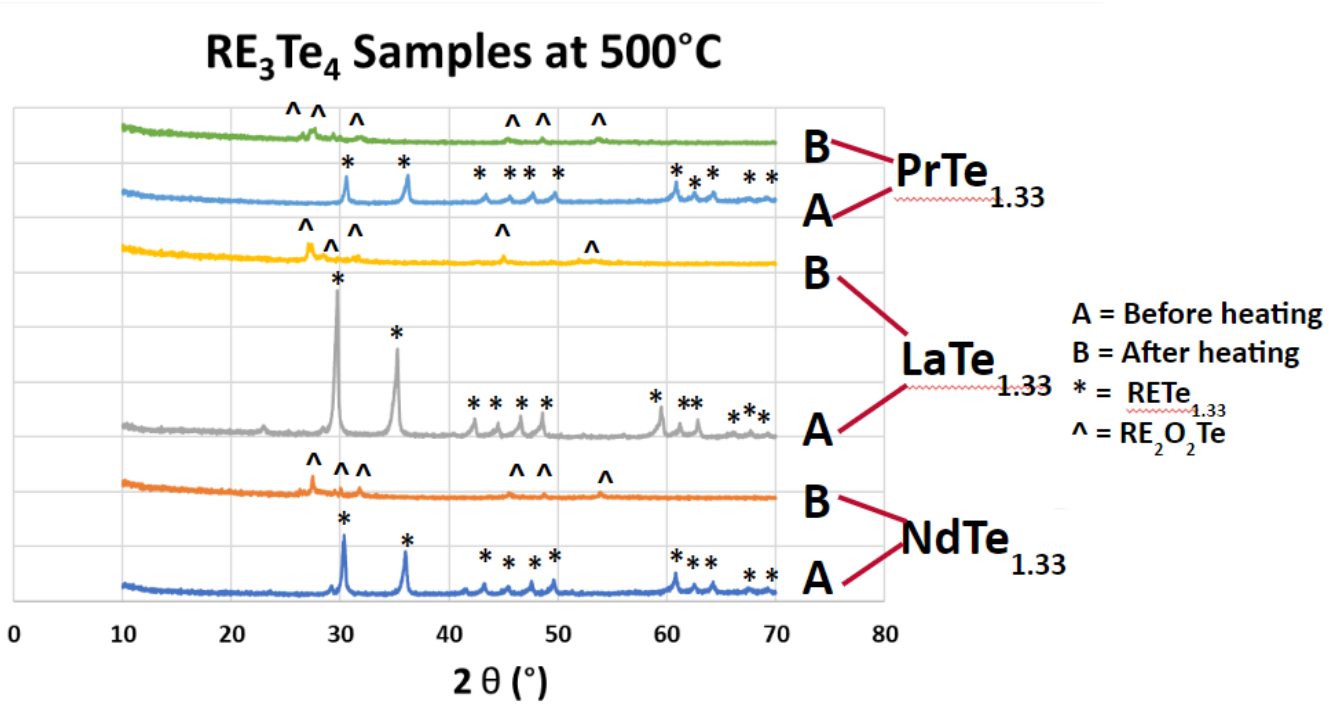

Figure 2.3. Pre (A) and Post (B) tube furnace heating XRD results of rare earth (RE) tellurides ($RETe_{1.33}$)

XRD results indicate that, at room temperature, the initial rare earth tellurides ($RETe_{1.33}$) is the major phase observed. However, for $NdTe_{1.33}$ and $LaTe_{1.33}$, a minor oxide peak can be observed at 29°2Θ. After the heat treatment, all of the samples completely decomposed into rare earth (RE) oxytellurides (RE_2O_2Te). However, as seen in Figure 2.2, $NdTe_{1.42}$ retained its initial shape, while all of the other samples became less-compact powders. It is hypothesized that the samples lost their initial shape due to the coefficient of thermal expansion (CTE) mismatch between the initial rare earth tellurides and the rare earth oxytellurides.

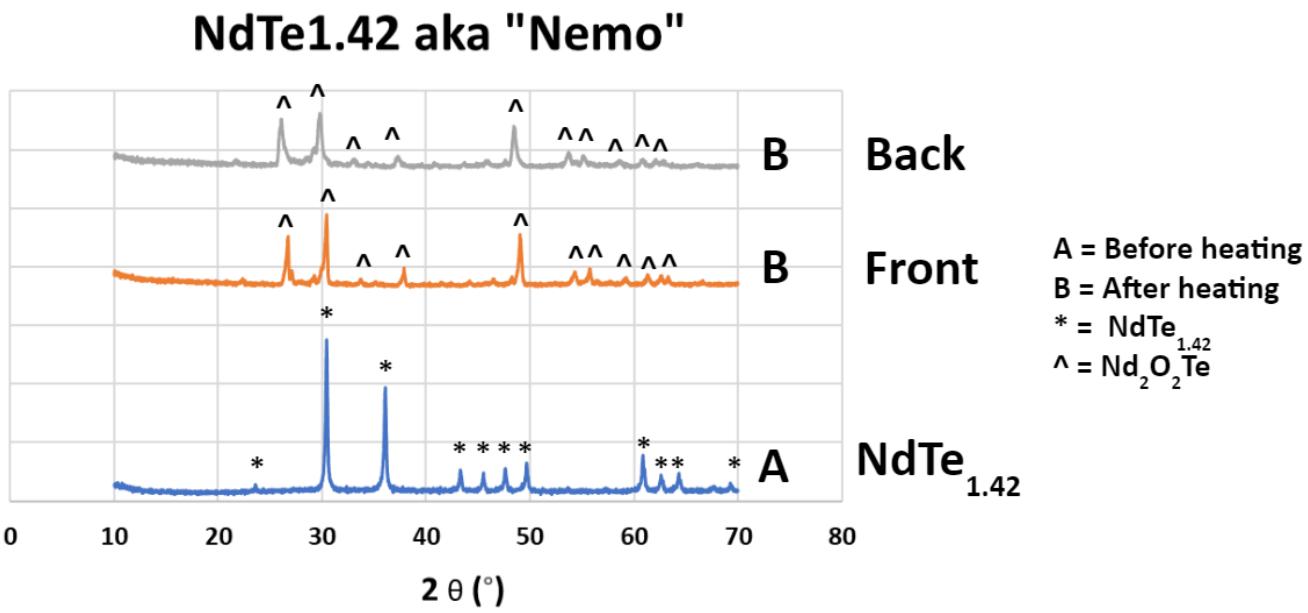

Figure 2.4. Pre (A) and Post, including Front and Back (B) tube furnace heating XRD results of $NdTe_{1.33}$

XRD analysis of $NdTe_{1.42}$ indicated that some of the initial stoichiometry was still present in the oxidized sample. Based on these results, the following was hypothesized: The surface of the $NdTe_{1.42}$ sample, when exposed to air at higher temperatures, began to oxidize into Nd_2O_2Te. The sample would thus have two interfaces: the interface of Nd_2O_2Te and air, and the interface between the residual $NdTe_{1.42}$ and Nd_2O_2Te. Because $NdTe_{1.42}$ was still present in the sample, it was hypothesized that the Nd_2O_2Te served as a passivation layer, where some of the initial $NdTe_{1.42}$ was retained. An illustration of this is shown in Figure 2.5.

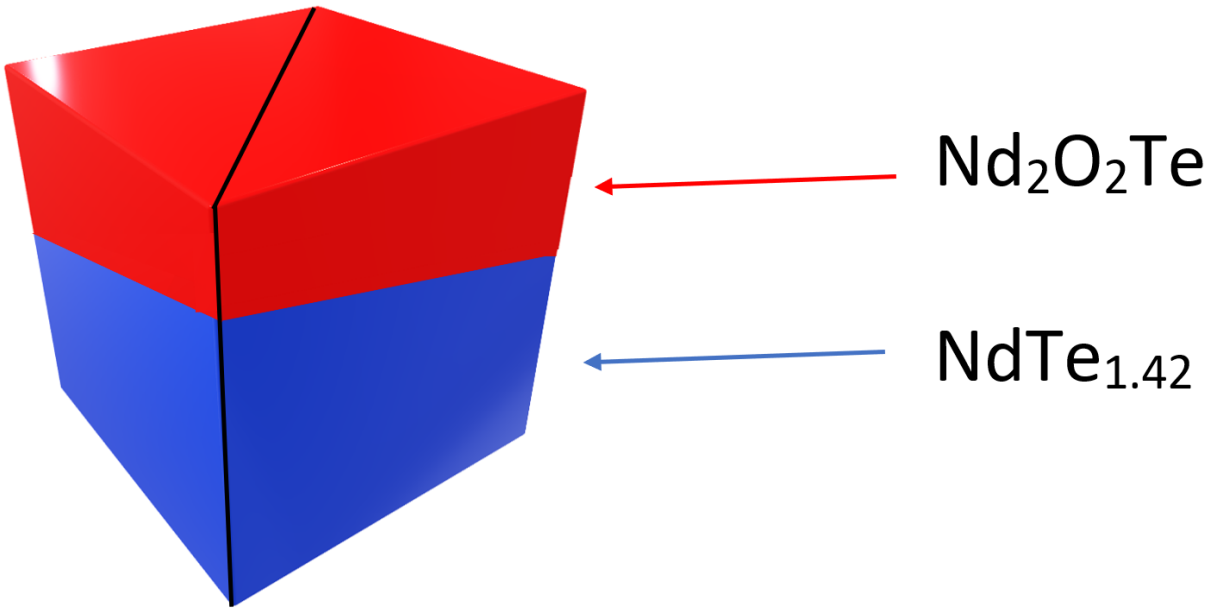

Figure 2.5. Hypothesized Nd_2O_2Te passivation layer formation from post-tube furnace heating of $NdTe_{1.42}$. The cross-sectional area is shown by a black line

To determine this, line scans were performed on the cross-section of the heated $NdTe_{1.42}$ sample via SEM analysis. Line scans that were conducted within 70 microns of the cross-section of $NdTe_{1.42}$ showed no significant changes in Nd, O, or Te levels, as seen in Figure 2.6. This indicated that the sample was completely oxidized, but was still able to maintain its original shape. Thus, it is hypothesized that there is a minimal CTE (coefficient of thermal expansion) mismatch between $NdTe_{1.42}$ and its oxytelluride (Nd_2O_2Te).

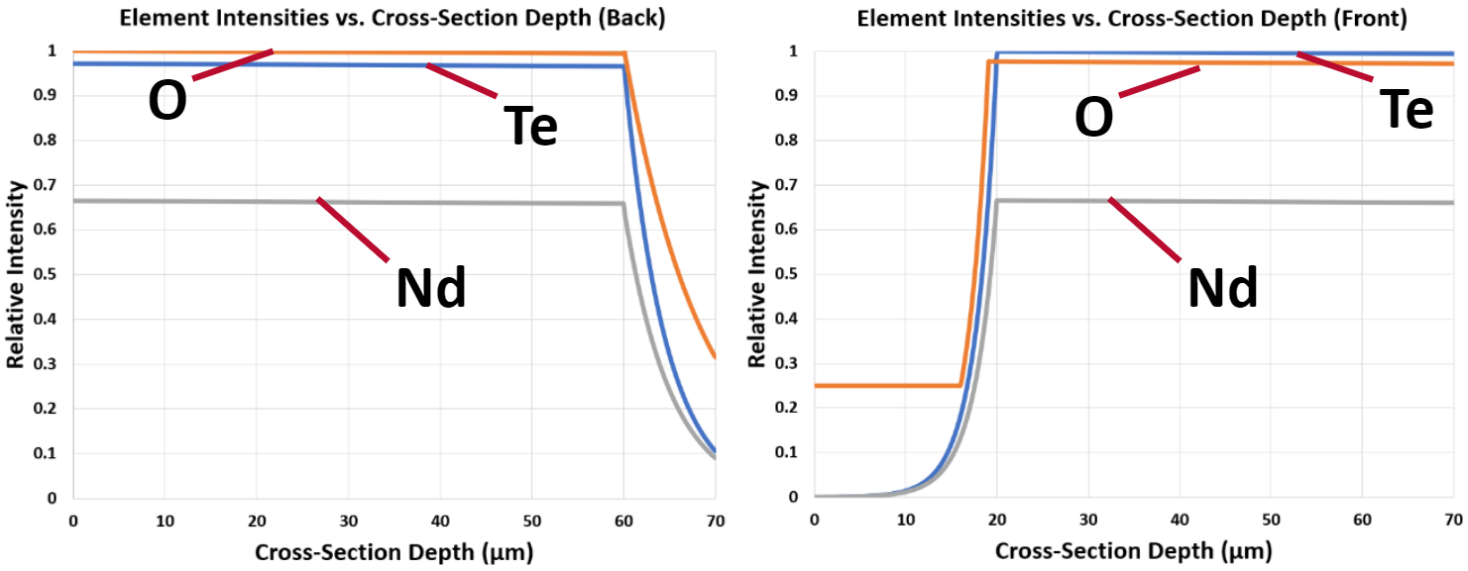

Figure 2.6. Respective Nd, Te and O levels for both the back (left) and front (right) of the cross-section of $NdTe_{1.42}$

TGA experiments were conducted to determine the kinetics of the oxidation for the rare earth tellurides (RE_3Te_4). The following heating profile was utilized:

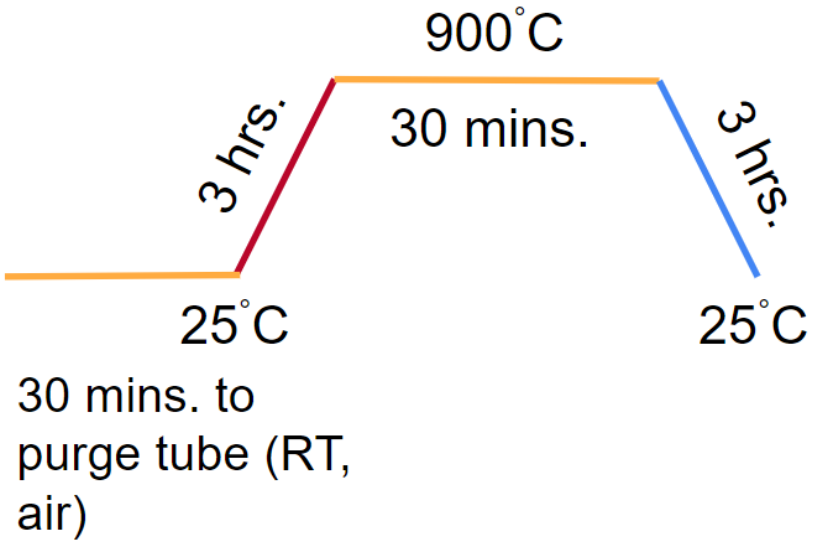

Figure 2.7. Heating Profile for TGA experiments for rare earth tellurides (RE_3Te_4)

Weight gain as a function of temperature was analyzed for the following samples: La_3Te_4, Pr_3Te_4 and Nd_3Te_4, as seen in Figure 2.8. There were very distinct differences noted, especially during the initial heating steps; as the temperature increases, Pr_3Te_4 initially has the greatest change in slope, followed by La_3Te_4 and Nd_3Te_4. However, around approximately 425°C, La_3Te_4 has a drastic slope change, drastically increasing the weight gain until it reaches saturation around 900°C. However, Nd_3Te_4 and Pr_3Te_4 do not see a drastic slope change until 440°C and 460°C. Because there are significant differences in weight gain across rare earth tellurides, this suggests that there are distinct differences in the oxidation kinetics and mechanisms across rare earths.

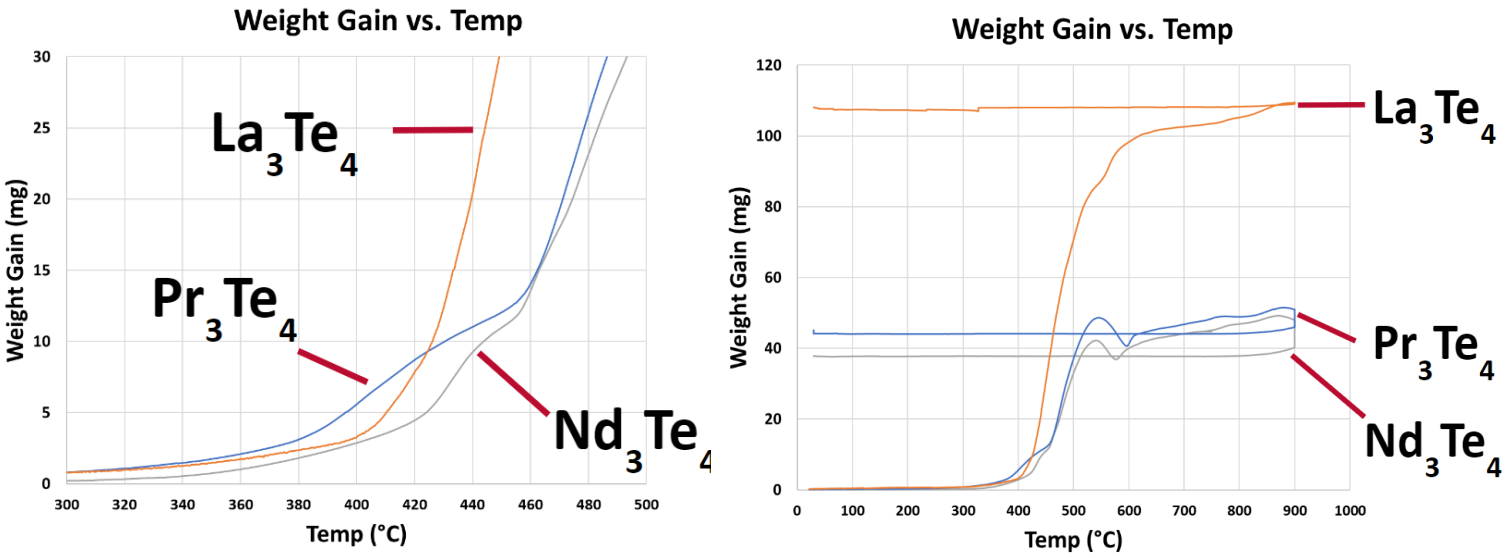

Figure 2.8. Weight gain as a function of temperature for various rare earth tellurides from 300-500°C (left) and from 25-900°C (right)

Composition	Weight Increase (%) at 350°C	Weight Increase (%) at 475°C	Weight Increase (%) at 575°C
La_3Te_4	100.21	108.19	114.23
Pr_3Te_4	100.34	104.32	108.53
Nd_3Te_4	100.17	104.58	108.32

Table 2.1. Weight increase of RE_3Te_4 at various temperatures for various compositions

Table 2.1 highlights specific temperatures (350°C, 475°C, and 575°C) where the weight increase, thus the slope of the weight gain, has significantly changed. This also emphasizes the distinctions in oxidation kinetics, because different rare earth tellurides exhibit different weight increases at different temperatures.

To understand the differences in kinetics for these materials, it's important to outline the mathematical description of rate laws. Rate laws are expressions that describe the relationship between the rate of a reaction and the amount of the reactants. Using the hydrolysis of acetylsalicylic acid as an example, we see that it breaks down into salicylic acid and acetic acid in Figure 2.9:[7]

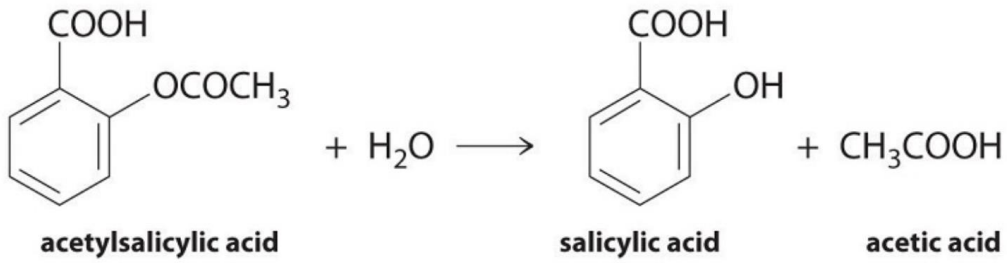

Figure 2.9. Hydrolysis of acetylsalicylic acid into salicylic acid and acetic acid

Because the breakdown of acetylsalicylic acid and the formation of salicylic acid is 1:1, the following equation can be used to describe the rate kinetics of the reaction:

$$rate = \frac{-\Delta[A]_{(s)}}{\Delta t} = \frac{\Delta[B]_{(s)}}{\Delta t} \quad \textbf{Equation 2.1}$$

where [A] is the concentration change of acetylsalicylic acid, [B] is the concentration of the salicylic acid formation, and Δt represents the change in time. This generalized equation was then applied to this research, where the decomposition of the rare earth telluride results in the formation of the rare earth oxytelluride.

Based on the XRD results from the tube furnace experiments showing the presence of oxytelluride in the oxidized samples, we hypothesize Equation 2.2 for all RE_3Te_4 above 500°C, which corresponds to the following rate equation:

$$2RE_3Te_{4(s)} + 3O_{2(g)} \longrightarrow 3RE_2O_2Te_{(s)} + 5Te_{(g)} \quad \textbf{Equation 2.2}$$

In the balanced equation above, we see that rare earth tellurides, when exposed to oxygen, form the oxytelluride with some tellurium sublimation taking place as well. Thus, for the rate equation, the decomposition of the rare earth telluride corresponds to a weight gain via TGA analysis which is the weight of the formation of the oxytelluride.

The following equation highlights how the rate of the decomposition of the initial rare earth telluride corresponds to the rate of formation of the rare earth oxytelluride:

$$rate = \frac{-\Delta 2RE_3Te_{4(s)}}{\Delta t} = \frac{\Delta RE_2O_2Te_{(s)}}{\Delta t}$$ **Equation 2.3**

Inputting values for La_3Te_4, Nd_3Te_4 and Pr_3Te_4 at 172.3 minutes into the experiment (which corresponds to 700°C), we were able to see the following differences in rate of formation of the oxytelluride in Table 2.2:

Composition	Rate of Formation (mg/min) ($x10^{-2}$) at 700°C
La_2O_2Te	8.28
Pr_2O_2Te	5.48
Nd_2O_2Te	5.14

Table 2.2. Rate of formation of rare earth oxytellurides at 700°C for various compositions

According to the calculated values for the rate of formation of oxytellurides, there is a clear and distinct difference across the rate earths. Lanthanum oxytelluride rate of formation is 51% greater than praseodymium oxytelluride, and 61% greater than neodymium oxytelluride at 700°C.

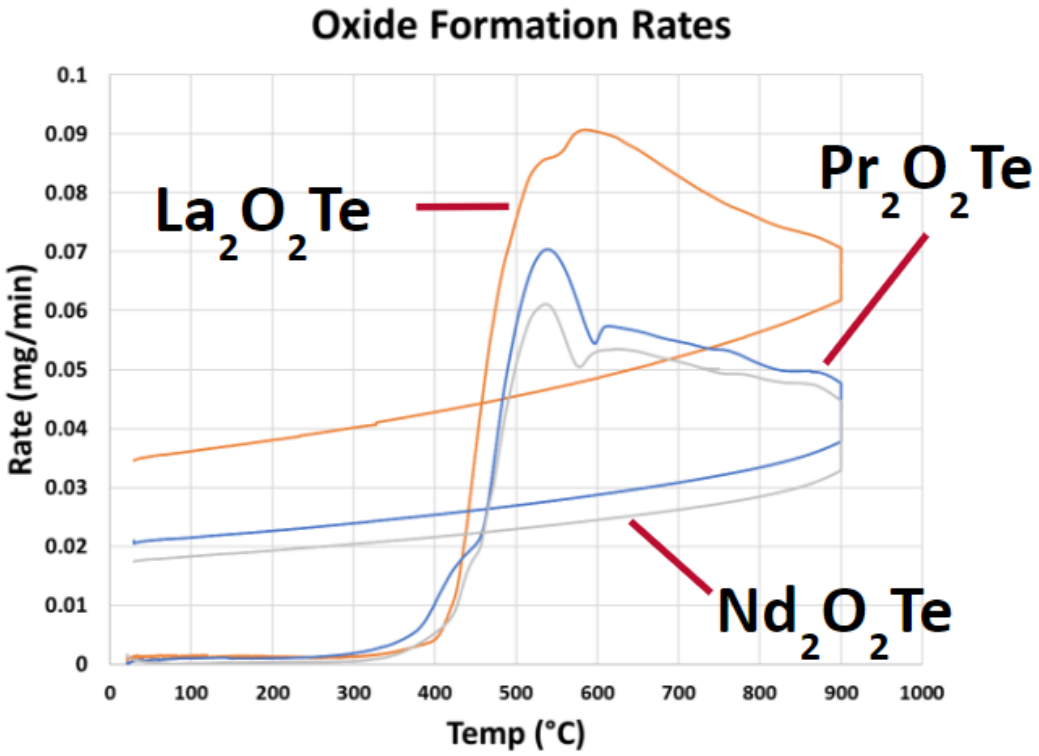

Figure 2.10. Oxide formation rates as a function of temperature for various rare earth oxytellurides

Because the oxidation rates change with respect to temperature, Figure 2.10 also highlights rate changes at significant temperatures. Up to 350°C, there is minimal oxide formation across all rare earth tellurides (RE_3Te_4). However, from 350°C to 375°C, rare earth oxytelluride formation begins. Pr_2O_2Te has the most significant formation rate at this temperature range, followed by La_2O_2Te and Nd_2O_2Te. However, from 475°C to 575°C, this pattern changes; La_2O_2Te now has the most significant formation rate, followed by Pr_2O_2Te and Nd_2O_2Te. Above 575°C, the same pattern emerges; however, La_2O_2Te formation becomes even greater compared to Pr_2O_2Te and Nd_2O_2Te.

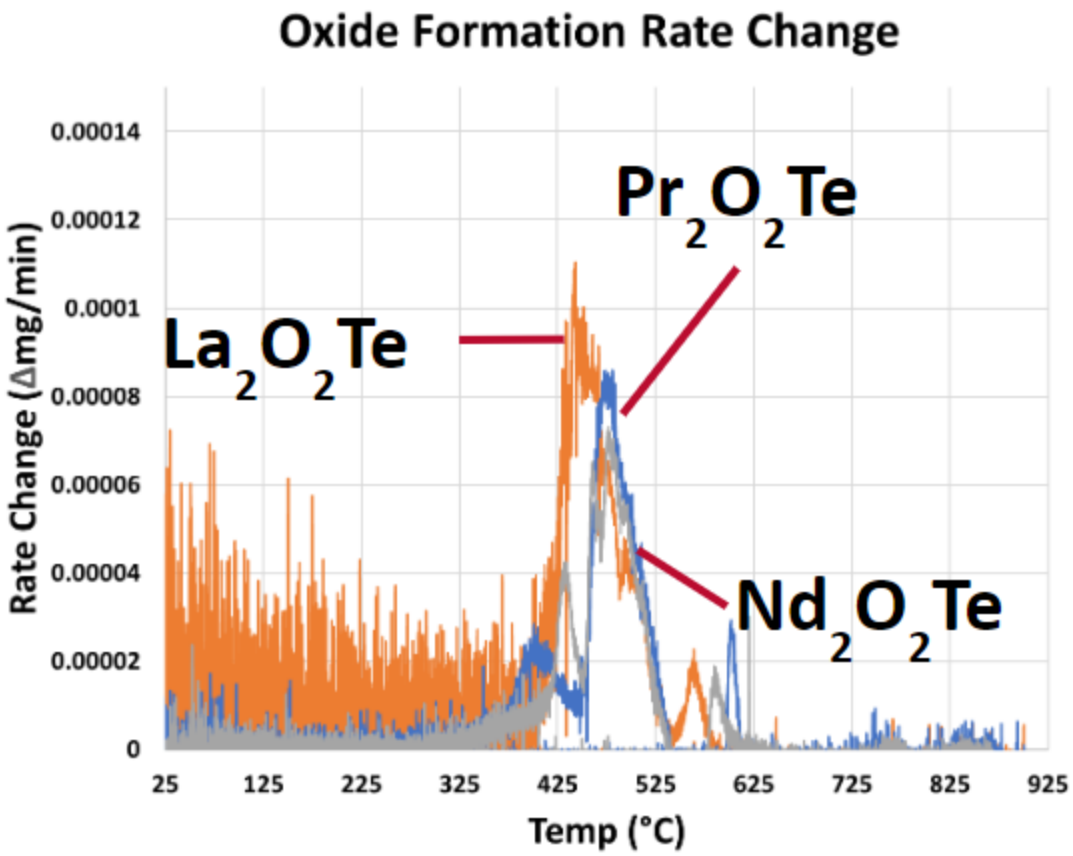

Figure 2.11. Oxidation formation rate change with respect to temperature for various rare earth tellurides

Figure 2.11 highlights major differences in oxidation formation rate change. La_2O_2Te has a more drastic rate change over a larger temperature range, until it reaches saturation. In contrast, Pr_2O_2Te and Nd_2O_2Te have smaller rate changes that take place over the larger temperature range. While there are some drastic increases in rate change at specific temperatures, overall the oxidation formation rate change is smaller compared to La_2O_2Te.

In our case, there is difficulty in experimental identification of oxides without separation of the scale from the matrix: diffraction peaks of oxides overlap with matrix peaks, and further investigation with XPS is necessary to identify the oxidation mechanisms for other rare earth tellurides such as Pr_3Te_4 and Nd_3Te_4. However, from our kinetics data, we can conclude that there are noticeable differences in the rate of the reactions: La_3Te_4 oxidizes at higher temperatures at a faster rate compared to Nd_3Te_4 and Pr_3Te_4, which begin oxidizing at lower temperatures but overall have lower oxidation rates in comparison.

Rate constant calculations were extrapolated from the oxide formation rate for three distinct temperature ranges: 375-400°C, 475-500C, and 575-600°C. The Arrhenius equation highlights the correlation between the rate constant, activation energy and temperature:

$$k = k_0 \exp\left(\frac{-E_a}{RT}\right) \quad \textbf{Equation 2.4}$$

where k is the rate constant, k_0 is the pre-exponential factor, E_a is the activation energy, R is the gas constant and T is temperature.

When rearranged to the slope-intercept form, we can utilize the follow equation to determine the apparent activation energy of different rare earth oxytellurides from the slope of the corresponding lines:

$$\ln k = \frac{-E_a}{RT} + \ln k_0 \quad \textbf{Equation 2.5}$$

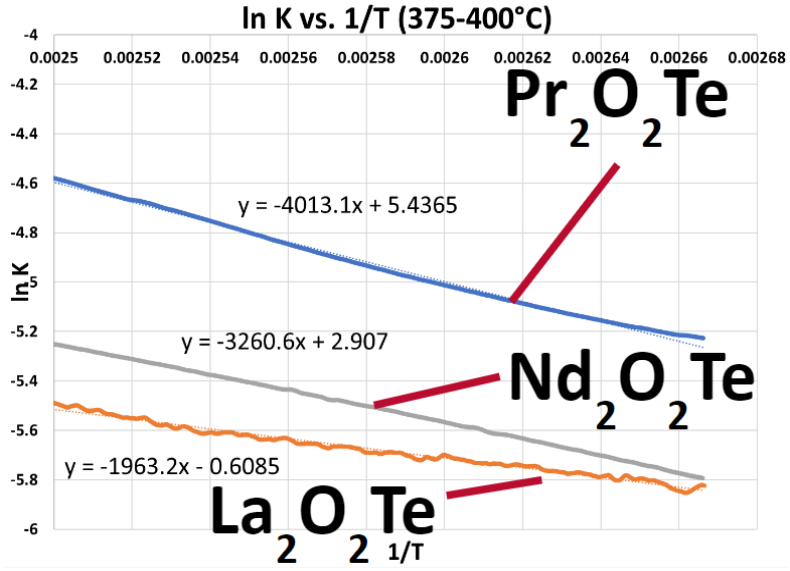

Figure 2.12. Arrhenius plots for various rare earth oxytellurides from 375-400°C

Figure 2.12 illustrates the Arrhenius plots for the corresponding rare earth oxytellurides from 375-400°C. It should be noted that a steeper slope corresponds to a larger activation energy. Figures 2.13 and 2.14 correspond to Arrhenius plots for 475-500C and 575-600°C respectively.

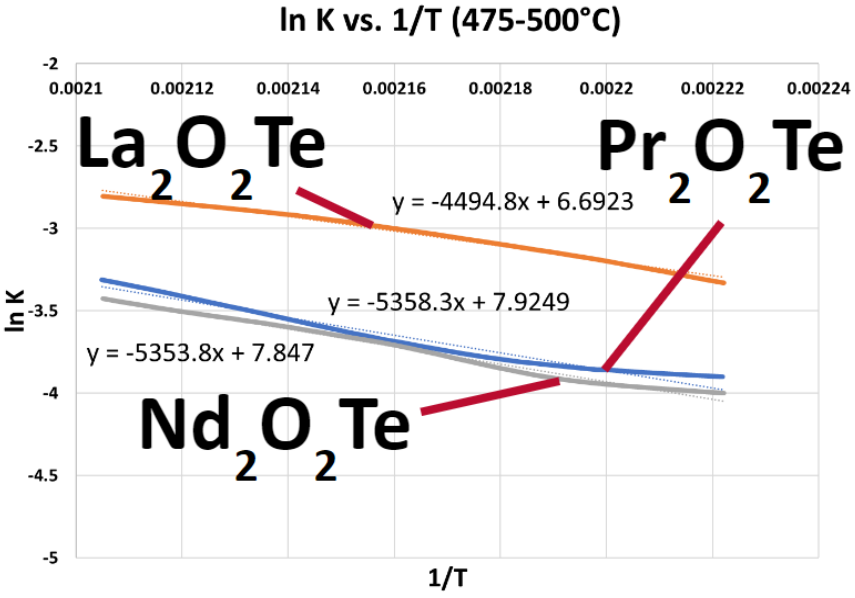

Figure 2.13. Arrhenius plots for various rare earth oxytellurides from 475-500°C

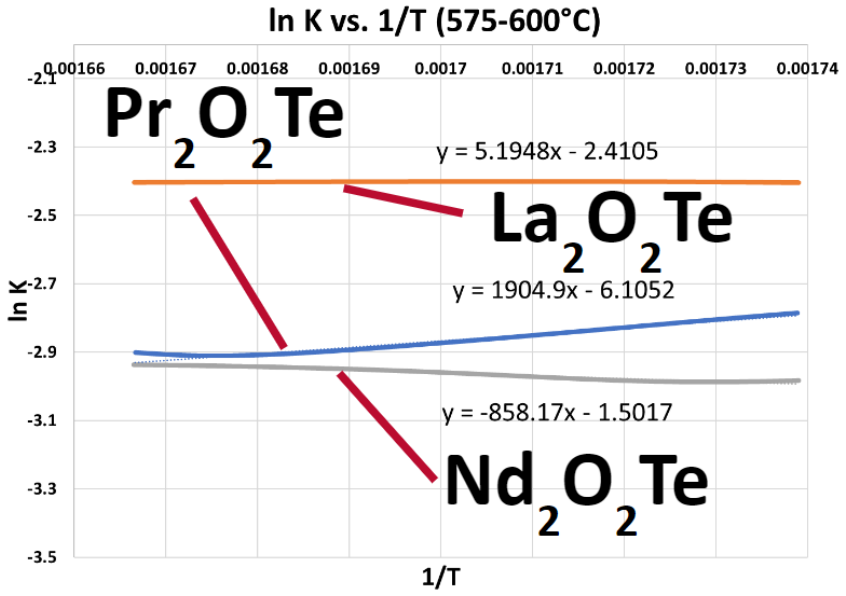

Figure 2.14. Arrhenius plots for various rare earth oxytellurides from 475-500°C

These figures indicate that the slopes (thereby the apparent activation energies) for the formation of the rare earth oxytellurides is the largest, and most significant within the 475-500°C temperature range. The calculated apparent activation energies for each rare earth oxytelluride within each temperature range is shown in Table 2.3:

Comp.	E_a (kJ/mol) 375-400°C	E_a (kJ/mol) 475-500°C	E_a (kJ/mol) 575-600°C
La_2O_2Te	33.3	37.4	0.043
Pr_2O_2Te	16.3	44.5	15.8
Nd_2O_2Te	27.1	44.5	7.1

Table 2.3. Activation energy (E_a) of rare earth oxytellurides at different temperature ranges

Understanding the differences in the apparent activation energies gives us better insight into periodic trends and clarifies the role of each rare earth in the oxidation process. Starting with the 375-400°C temperature range, we see that Pr_2O_2Te has the lowest barrier to formation (activation energy), and therefore is the most likely rare earth within this temperature range to begin oxidation. Nd_2O_2Te has the second-lowest activation energy, followed by La_2O_2Te; this thereby hints to a periodic trend and the influence of the rare earth on the activation energy.

Within the 475-500°C temperature range, La_2O_2Te activation energy increases slightly; however, both Pr_2O_2Te and Nd_2O_2Te have comparatively higher barriers to formation. This indicates that La_2O_2Te is most likely to form within this temperature range compared to other rare earths. And within the 575-600°C temperature range, both Pr_2O_2Te and Nd_2O_2Te have a lower barrier to oxidation compared to other temperature ranges. However, La_2O_2Te activation energy has the most significant decrease, resulting in rapid oxidation formation. This helps to illustrate the significance of rare earths on the formation of rare earth oxides; moving across the lanthanide series, the general trend would indicate an increase in oxidation resistance. This could potentially be attributed to the contribution of *f*-electrons, which is discussed more extensively in Chapter 2.

At high partial pressures of oxygen, Pr_3Te_4 and Nd_3Te_4 exhibit oxidation prior to La_3Te_4; this is mostly likely due to a lower activation energy for oxytelluride formation as was seen in the TGA results. However, it is proposed that once the praseodymium and neodymium oxytelluride phases form, they are more stable compared to lanthanum oxytelluride, which kinetically oxidizes the parent sample faster than other rare earths. The formation of the complex oxytelluride may enhance the semi-protective properties of the oxidized scale; however, the oxide layer is not stable enough to serve as a passivation layer. Still, a detailed mechanism of the scale formation remains to be elucidated and requires further study.

Further research into synchrotron XRD is necessary to determine the differences in lattice parameters of the rare earth tellurides, which would give insight into what intermediary phases were forming as a result of oxidation. Also, more isothermal studies would provide more quantitative analysis regarding reaction rate kinetics and the distinctions across rare earth tellurides due to periodic trends.

2.4. Summary

There is a distinctive difference in oxidation rates (and potentially mechanisms) for different rare earth tellurides (RE_3Te_4). Research indicates that rare earth tellurides experience similar oxidation mechanisms, but at distinct rates. Pr_3Te_4 and Nd_3Te_4 oxidize kinetically faster compared to La_3Te_4, which would suggest there is less time for the formation of intermediate phases. Future studies should explore high-temperature x-ray diffraction (HT XRD) measurements at fixed temperatures to understand the formation of intermediary phases and provide better insight into oxidation mechanisms.

2.5. References

[1] Matthes, C. S. R.; Woerner, D. F.; Caillat, T.; & Pinkowski, S. A Status Update on the eMMRTG Project. *IEEE Aerospace Conference* **2019**, 1-7. http://dx.doi.org/10.1109/aero.2019.8741919

[2] Hiller, N.; Allen, D.; Elsner, N.; Bass, J. C.; & Moore, J. P. Outgassing and vaporization considerations in milliwatt generators designed for 20-year missions. *AIP Conference Proceedings* **2002**, 1-9. http://dx.doi.org/10.1063/1.1449829

[3] Matthes, C. S. R.; Whiting, C. System-Level Risk Reduction Activities for the eMMRTG Project. *IAASS Conference* **2018**, 1-13.

[4] Vasilyeva, I., Abdusalyamova, M., Makhmudov, F., Eshov, B., & Kauzlarich, S. Thermal Air-Oxidized Coating on $Yb_{14-x}RE_xMnSb_{11}$ Ceramics. *Journal of Thermal Analysis and Calorimetry* **2018**, *136*, 541–48. https://doi.org/10.1007/s10973-018-7659-z

[5] Cheikh, Alexander. Novel Synthesis and Processing of Lanthanum Telluride ($La_{3-x}Te_4$) Thin Films via Electrophoretic Deposition and Ultrafast High-Temperature Sintering for Advanced High-Temperature Thermoelectric Device Applications, UCLA, **2023**, https://escholarship.org/uc/item/8fm4v07d

[6] May, A. F., Fleurial, J.-P., & Snyder, G. J. Thermoelectric performance of lanthanum telluride produced via mechanical alloying. *Physical Review B*, **2008**, *78*, 12. https://doi.org/10.1103/physrevb.78.125205

[7] Niels, Thomas. *Chemistry of the Modern World*. 1st, LibreTexts, **2020**.

Chapter 3: $La(Pr)_{3-x}Te_4$ Alloys

3.1. Introduction

The purpose of this study is to develop high-efficiency thermoelectric materials through low-temperature synthesis and thermoelectric characterization of systems such as $La_{3-x}Pr_xTe_4$. Previous research I conducted at NASA's Jet Propulsion Laboratory focused on evaluating the thermoelectric performance of $Pr_{3-x}Te_4$.[1] Heavy conduction bands in the band structure are typically favorable for acquiring a large Seebeck coefficient. The $La_{3-x}Te_4$ system possesses a sharp peak in the Density of States (DOS) near the Fermi level in the conduction band, as seen in Figure 3.1. La 5*d* and 4*f* states contribute to the peak at the conduction band; however, La lacks *f* electrons in the 4*f* shell. If *f*-orbital electrons are introduced into the system, Density Functional Theory (DFT) calculations predict that it would have a significant impact on the thermoelectric properties of the system by moving the peak density of states closer to the Fermi level. Since the Seebeck coefficient is defined as the 1st derivative of the DOS, a large change in the DOS at the band edge would lead to a larger Seebeck coefficient, which would significantly improve *ZT*. Praseodymium (Pr) has the capability to introduce *f*-orbitals into the $La_{3-x}Te_4$ system, thus potentially improving the Seebeck coefficient and enhancing *ZT*.[1]

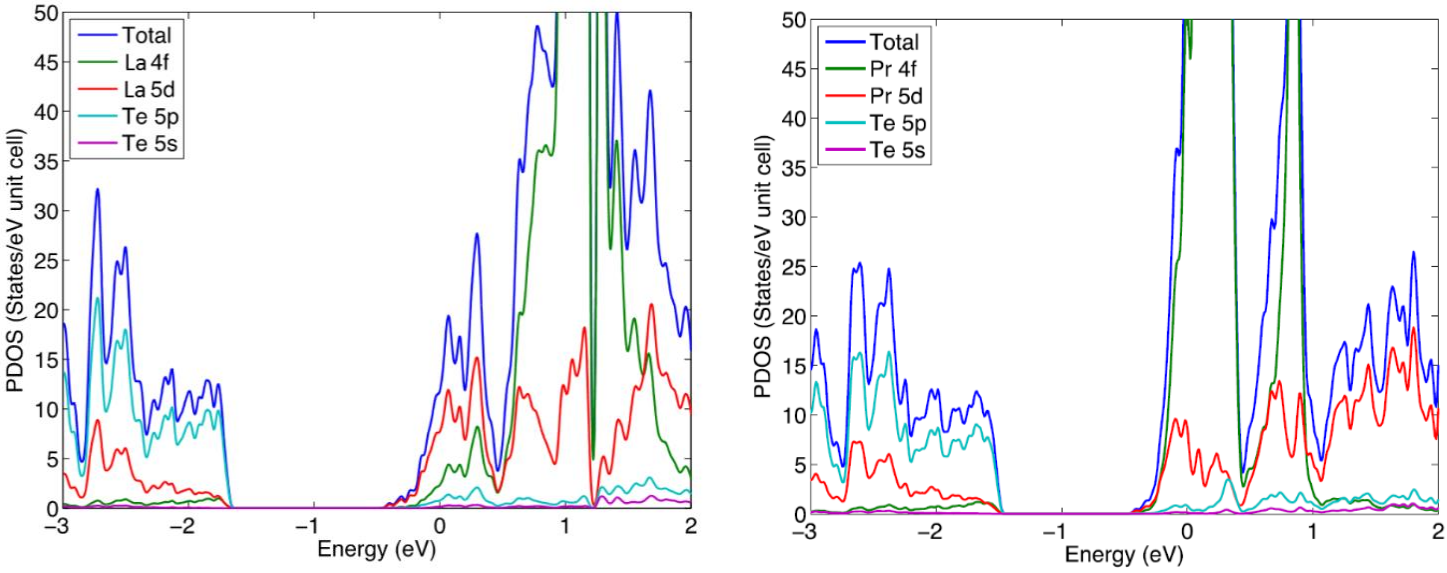

Figure 3.1. Partial Density of States (PDOS) for La_3Te_4 (left) and Pr_3Te_4 (right)[2]

Based on my research, peak *ZT* of 1.7 was achieved at 1200 K for the $Pr_{3-x}Te_4$ system, compared to the optimized *ZT* of 1.1 for $La_{3-x}Te_4$ (see Appendix A). The improvement in *ZT* resulted from the large increase in the Seebeck coefficient from the electronic states introduced by the 4*f* electron, as predicted from the computational modeling. Lower thermal conductivity, which results from a decreased lattice contribution, also resulted in the higher *ZT* value for the $Pr_{3-x}Te_4$ system.

My previous research has clearly demonstrated that the $Pr_{3-x}Te_4$ system has been shown to have significant impact on the Seebeck coefficient through the modification of the DOS. Therefore, alloying in the $La_{3-x}Te_4$ system with other rare earths (RE) such as Pr is a promising pursuit that could lead to even higher *ZT*s due to increased *f*-electron density and phonon scattering. Later rare earths have more *f*-electrons (and can therefore play a larger role in DOS); however,

they do not exist in the Th_3P_4 structure type.[1] If we alloy within the $La_{3-x}Pr_xTe_4$ system, we can successfully synthesize this series and produce efficient thermoelectric materials.

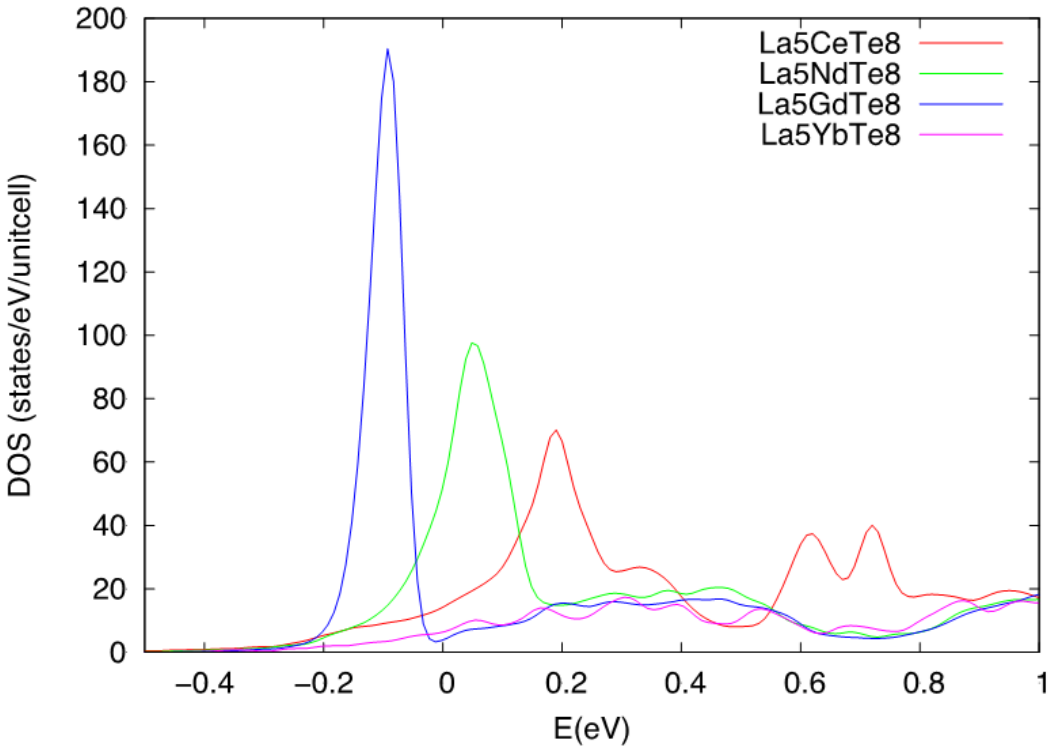

Figure 3.2. Density of States (DOS) for various La_5RETe_8 systems (Trinh Vo, to be published)

Figure 3.2 showcases the density of states for La_5RETe_8 systems (RE = Ce, Nd, Gd and Yb). There are significant differences in the peak density of states when different rare earths are introduced to the La_5RETe_8 system. For instance, moving left to right across the lanthanide series (Ce → Nd → Gd → Yb), more *f*-electrons are being introduced in the system, leading to the peak density of states approaching the Fermi level. With La_5GdTe_8, however, the peak shifts to the valence band; with La_5YbTe_8 no significant peak is present either in the valence or conduction band.

Collaborators at JPL using Density Functional Theory calculations predict that if one La atom is substituted by one rare-earth atom of different f-configuration: Ce (4*f*1), Nd (4*f*3), Gd (4*f*7), and Yb (4*f*14), the sharp peak at the conduction band edge shifts from higher to lower energies as the number of *f*-electrons increases from 1 (Ce) to 3 (Nd) to 7 (Gd), as displayed in Figure 3.2. For Yb, which has a completely filled *f*-orbital, the peak shifts to the valence band. This highlights the importance *f*-electrons have with respect to the enhancement of thermoelectric properties.

It is hypothesized that alloying in the $La_{3-x}Pr_xTe_4$ system will tune the DOS via f-electrons, which will help reduce thermal conductivity because of point defect phonon scattering. Strategies that introduce point defects have been used to enhance the thermoelectric performance of numerous metal chalcogenides, including PbTe and SnTe.[3-4] Additionally, it will improve mechanical properties from solid solution strengthening. Solid-solution strengthening results from lattice strain interactions between impurity atoms and dislocations; these interactions produce a decrease in dislocation mobility, thus strengthening the alloy.[5-7] This strengthening mechanism has been studied in various alloys such as Mg-X (X=Ga,Al, Er,Y) and Al-Ce-Mg.[8-10] It is hypothesized that the hardness of the $La_{3-x}Pr_xTe_4$ alloys will increase with an increase in concentration of Pr_xTe_4 that goes into the solid solution. Previous research has shown the crucial role of vacancies (x) on elastic and mechanical properties in $RE_{3-x}Te_4$, and highlights the unique, underappreciated, and poorly understood nature of mechanical properties in thermoelectric materials, which may vary considerably across a wide range of doping levels (see Appendix B).

3.2. Synthesis Methods

All preparation steps will be performed in argon dry glove boxes (H2O < 1 ppm, O2 < 0.1 ppm). Pr_3Te_4 and La_3Te_4 were prepared based on targeted stoichiometric compositions using the corresponding elements (La, 99%, metals basis, HEFA Rare Earth; Pr, 99%, metals basis, Stanford Advanced Materials; Te, 99.999%, 5N Plus). The elements were combined in a stainless-steel vial with ½'' stainless steel balls. The sample was mechanochemically synthesized in a SPEX 80000 mixer/mill (as seen in Figure 3.3) until a homogeneous powder was synthesized.[11-13]

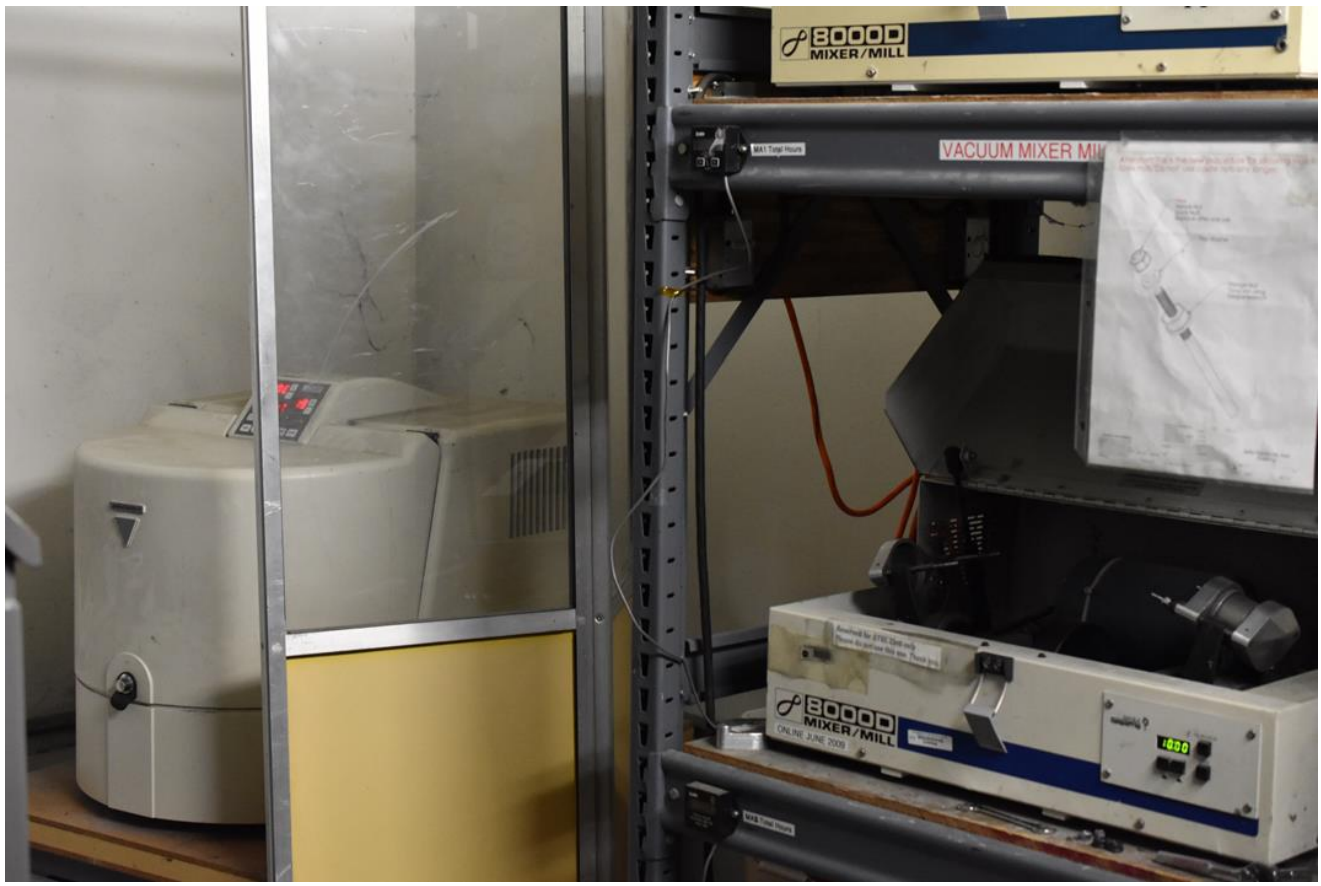

Figure 3.3. Fritsch Pulverisette P-5 four station ball mill (far left) and SPEX 80000 mixer/mill (far right)

Mechanochemical reactions are conducted through the transfer of mechanical energy to the reactants by high-energy collisions of the milling balls. During this process, the milling vials are secured in the clamp and swung energetically back and forth for multiple hours. The shaking motion is combined with lateral movements so that the amplitude (about 5 cm) and speed (about 1200 rpm) of the clamp motion results in high ball velocities, thus synthesizing the target compounds.[12]

Powders for the end members (Pr_3Te_4 and La_3Te_4) were synthesized first, and then they were milled together stoichiometrically to produce the alloys. The following weight percentages were synthesized and characterized to better understand the $La_{3-x}Pr_xTe_4$ system: 5%, 10%, 25%, 35%, 40%, 50%, and 75%. The powder was then loaded into 12.7 mm graphite dies and compacted using spark plasma sintering (SPS) at a pressure of 80 MPa and at temperatures above 1,200°C for 30 min under vacuum.[14-16]

Spark Plasma Sintering (SPS) is a process where diffusional mass transport leads to bonding between particles and the formation of dense bulk materials. It is a low-voltage, direct current, pulsed current-activated pressure technique. During sintering, external pressure and an electric field are applied simultaneously to enhance the densification of the powder compacts. The pulsed direct current is allowed to pass through the conductive graphite die and sample, producing an electric field. Thus, the powders undergo Joule heating and plastic deformation effects, allowing high relative densities in a relatively short time while undergoing uniaxial pressure inside a vacuum chamber.[15] The sintered, compacted samples had densities greater than 98% of the theoretical density, measured using the Archimedes method.

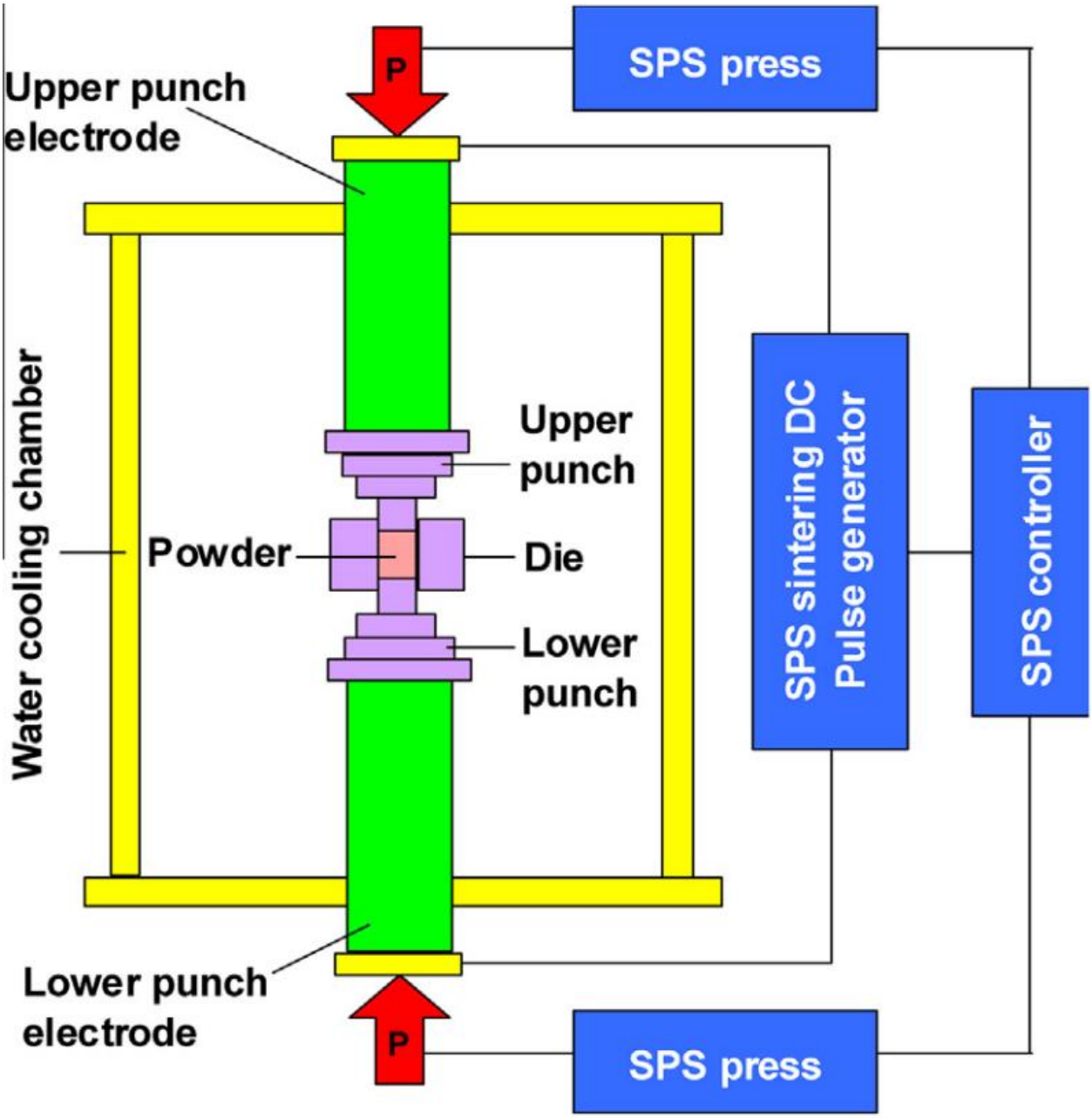

Figure 3.4. A Schematic of the SPS Process[14]

The schematic of the SPS process is highlighted in Figure 3.4. Multiple components are required for SPS equipment to function, including the furnace pressing chamber and power supply for the furnace as shown in Figure 3.5.

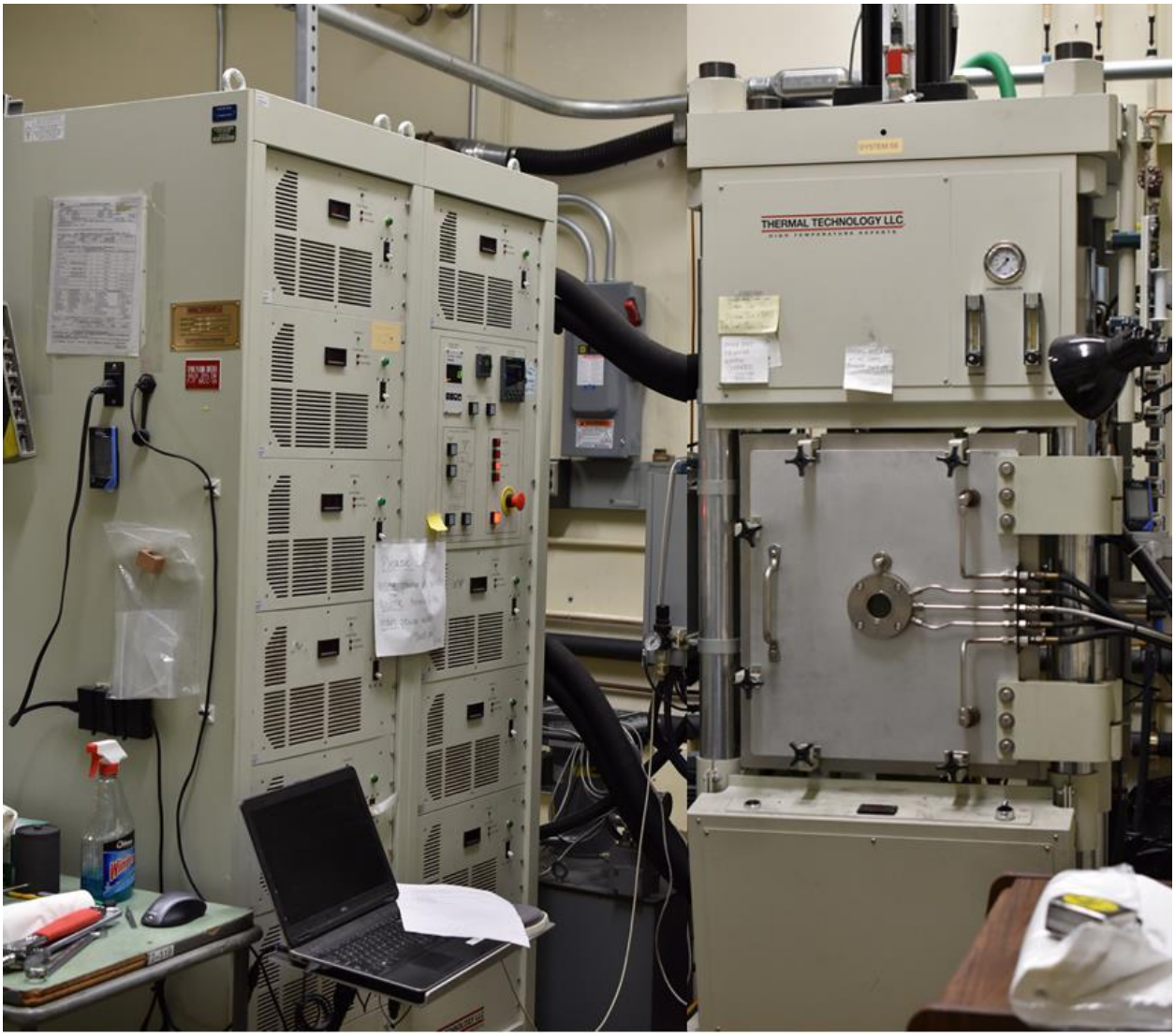

Figure 3.5. Thermal Technology LLC SPS 10-4 Advanced Technology furnace power supply (far left) and furnace pressing chamber (far right)

Other components that are essential to the function of the SPS instrument include the following: vacuum pumping system for evacuating the chamber and attaining a minimum of $5x10^{-2}$ mbar (preferably 10^{-4}), and a hydraulically controlled pressing system with adequately cooled rams to withstand the sintering temperature in the graphite die. The pressing cylinder was monitored manually through programmable software to ensure instantaneous levels of applied

force matched desired values. Water circulation systems are required to ensure the power feeder and electronics should have adequate water and air cooling for safe operation of equipment. Gas inlet systems purge the air from the chamber to pull a vacuum level required to begin the sintering process. The control console included temperature measurement tools to monitor the temperature of the graphite die compared to the programmed heating profile.

Back-scattered electron (BSE) scanning electron microscopy (SEM) was performed using a Zeiss 1550 VP SEM to observe phase homogeneity of the end members and alloys. X-ray diffraction (XRD) data was collected with a Phillips PANalytical X'Pert Pro diffractometer using Cu Kα radiation on sintered, compacted samples. Scans were performed from 10-70°2Θ at a rate of 1°/min. Rietveld refinements were utilized to determine the composition of the samples through refinement of the rare-earth occupancies. Rietveld refinement was performed using the GSAS-II crystallographic data analysis software.[17-18]

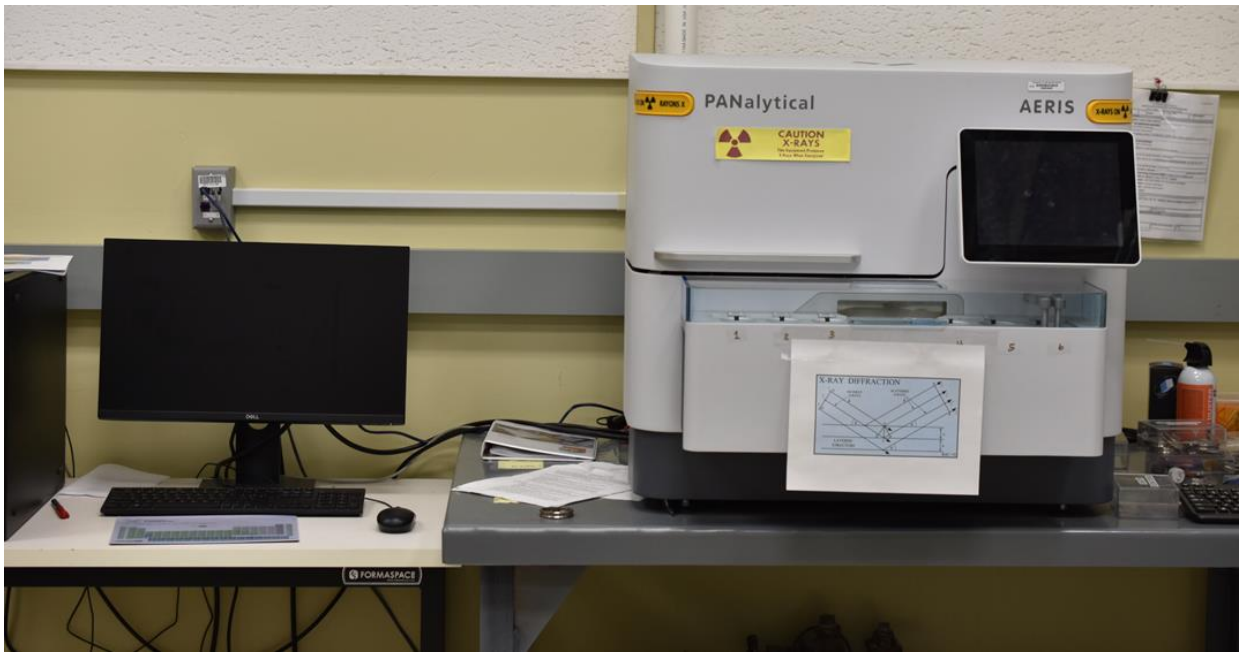

Figure 3.6. Phillips PANalytical X'Pert Pro diffractometer (right) and corresponding computer with HighScore Pro Analysis Software (left)

Structural data for the cubic phase with space group $I\bar{4}3d$ from Mitarov *et al.* was used for refinement.[19] In order to perform a stable refinement of the La occupancy, the occupancy on the Te position was held at 100% as no vacancies were expected.

A custom-built combined 4-point probe and Hall effect system was used to measure the electrical resistivity and Hall voltage using the Van der Pauw method.[20] Current between two adjacent probes on the sample edge induces a voltage between two additional probes on the edge of the sample, which is in the shape of a circular disk. Due to symmetry, reversing the polarity of both the voltmeter and current source results in the same resistance.[21-22] The Hall coefficient is a calculation of the induced Hall voltage orthogonal to both an electric and magnetic field. From the electrical resistivity and Hall voltage, carrier concentration and mobility are calculated as well.[23]

There are primary components that are essential to the function of the Hall instrument, include the following: 1 Tesla electromagnet, which allows for more space perpendicular to the magnetic field but a smaller pole gap for a higher magnetic field, and a vacuum vessel (minimum $5x10^{-3}$ mbar) with radiation shielding to minimize heat flow from the sample to the vessel. Resistive heaters surrounding the sample reach a maximum temperature of 1000°C. Typical experiments run the following heating profile: ramping from room temperature to 1000°C at a rate of 120°C/hour and cooling back to room temperature. Thermocouples, which control the heater response and accurately measure the sample temperature, are next to the sample that is attached to the stage. The dual-stage sample holder is composed of refractory metal bolts used to hold thick alumina plates together, thus doubling system throughput. The connections to the sample are made with four pressure contacts (aka four probes) connected by screws and posts to press against the top edges of the sample. 1.0-1.5 mm Molybdenum thin rods are utilized due to their flexibility and inert, non-magnetic qualities.

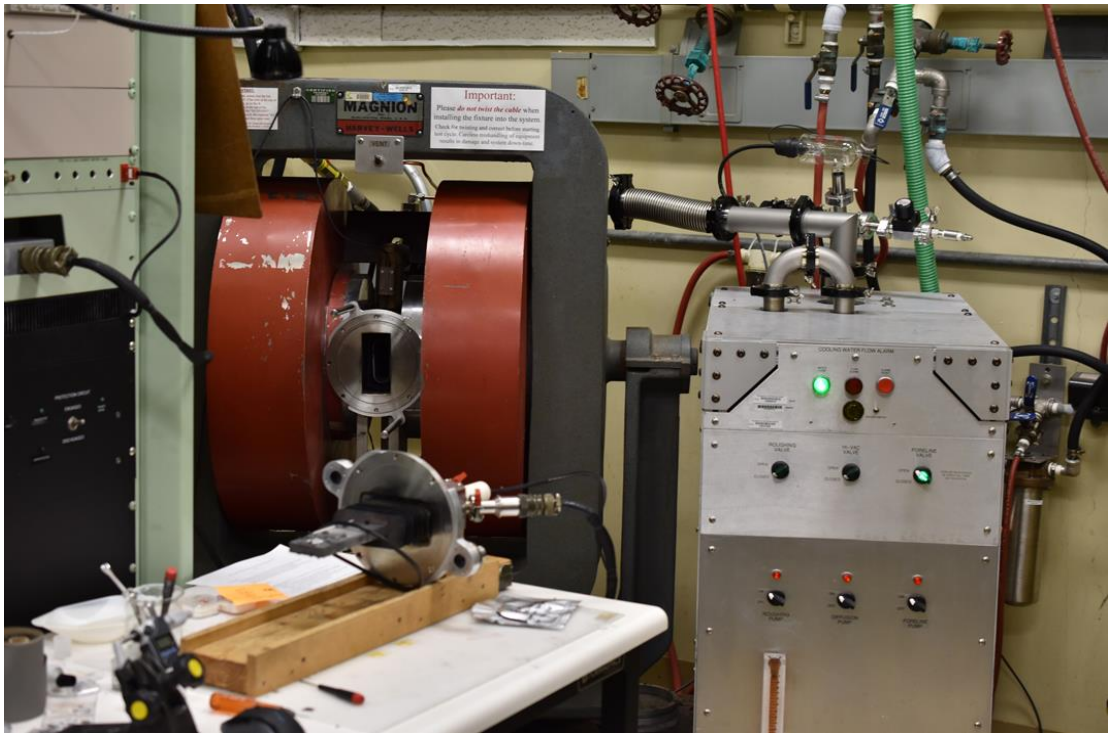

Figure 3.7. In-house Hall effect instrument with 1 Tesla magnet and vacuum control valves (right)

The Seebeck coefficient was measured using a custom-fabricated instrument.[24-25] In this high-temperature (~1700°C) apparatus, small thermal gradients are induced in the sample by light pulses transmitted via light pipes. In this apparatus, three IC instrumentation amplifiers are used to measure Seebeck voltage (dV) generated in the sample in response to the temperature gradient (dT). The outputs are plotted, and the slope is directly proportional to the Seebeck coefficient (see Figure 3.8).

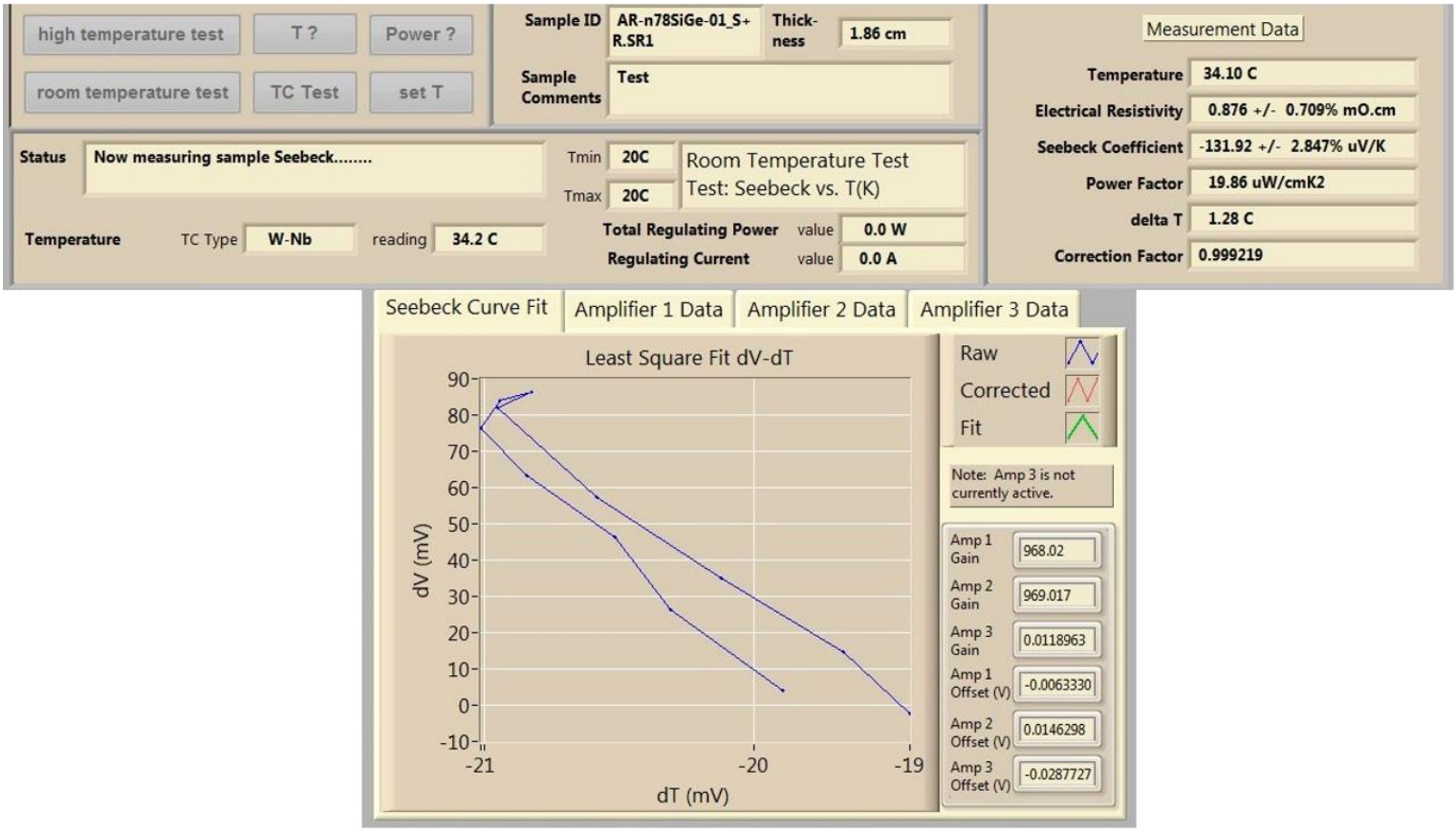

Figure 3.8. Plot of the least square fit of the difference in the voltage output from the amplifiers (dV) vs. the temperature gradient of the sample (dT) (bottom middle), and the corresponding Seebeck coefficient measurement data (top right)

Figure 3.9 highlights the outer insulation and the schematic diagram of the Seebeck coefficient apparatus. To measure the Seebeck voltage, the sample is placed between two sapphire disks. The W and Nb thermocouple wires are threaded through holes drilled in the sapphire disks, with the Nb wire directly contacting the sample. The sample and disks were pressed between two light pipes, with holes to accommodate the thermocouples wires on the light source side to deflect the light and shield the thermocouple junctions. The four furnace heater elements are fabricated from solid graphite plates and placed by heavy copper blocks outside the heater housing. The

heater housing is made of copper plates with water cooling tubes soldered to the outside walls. The graphite heater supply is a 150V dc 70-A Sorensen power supply with 280V ac three-phase 50-A input. The furnace brings a sample to a programmed temperature, where a small amount of current is applied through a resistor network. Two pulse lamps establish the hot and cold sides; the temperature of the hot side increases while the cold side decreases, so that the average temperature remains the same.[26]

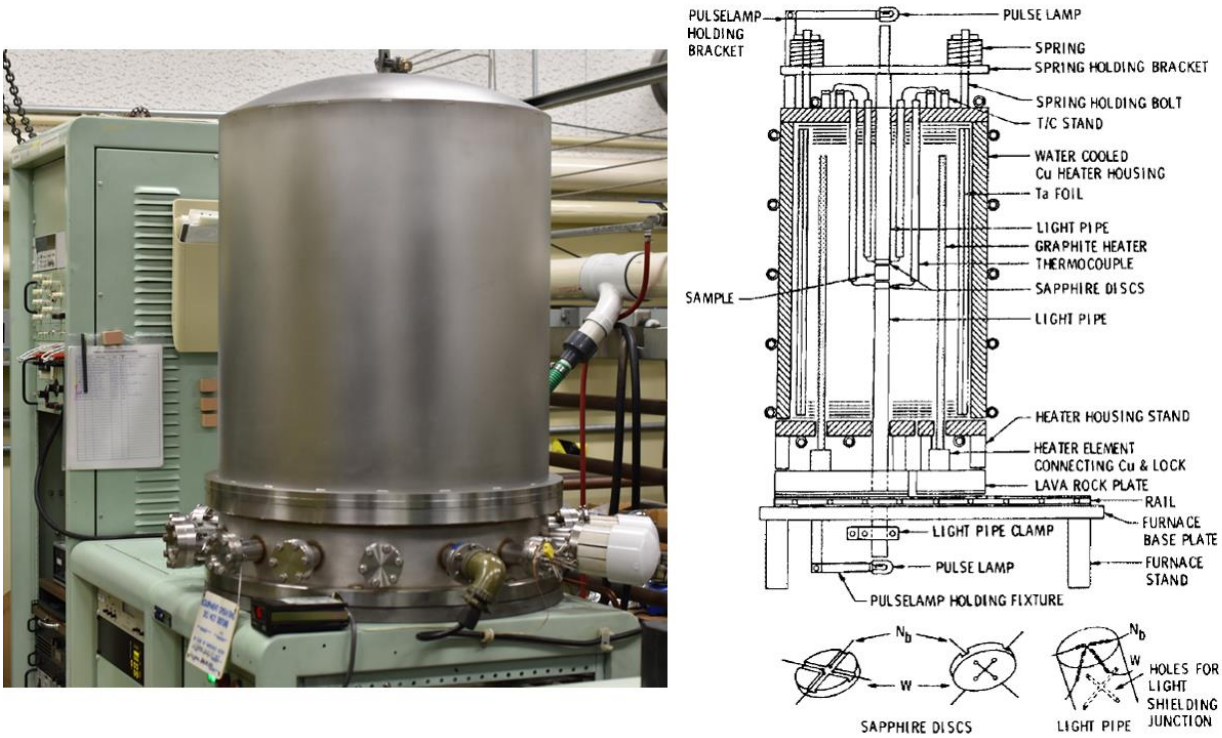

Figure 3.9. In-house Seebeck instrument, including outside (left) and inside schematic (right)

Thermal diffusivity was measured using a commercial Netzsch LFA 457 MicroFlash® system seen in Figure 3.10.[27-28] The measurement principle is as follows - the front side of a plane-parallel sample is heated by a short laser pulse. The absorbed heat induced propagates through the sample and causes a temperature increase on the rear surface. The temperature increase is

measured versus time using an infrared detector. The thermal diffusivity and the specific heat can be ascertained using the measured signal. If the density is known, the thermal conductivity can be determined by the following equation:

$$k = DC_p d \quad \textbf{Equation 3.1}$$

where k is the thermal conductivity, D is the thermal diffusivity, Cp is the specific heat capacity, and d is the sample density.

Short distances between the light source, sample and detector yield an excellent signal-to-noise ratio and allows for easy operation and sample change. There are many primary components that are essential to the function of the Hall instrument, include the following: The Nd: Glass laser has power output that is controlled by the software (18 J maximum pulse, 0.3 ms pulse length); an integrated laser beam enlargement system allows for homogeneous heating of samples between 6 and 25 mm in width. The forced-air cooled high temperature furnace allows measurements up to 1100℃, and is moved with a motorized hoist. A highly sensitive Indium Antimonide detector is used for high temperature measurements, and the automated sample changer allows for measurement of up to three samples at a time.[29-30]

Errors in electrical resistivity, Seebeck, and thermal conductivity were found to be approximately 5%, 20%, and 10%, respectively. The measured properties of the samples were not found to change with repeated thermal cycling, indicating high stability for the rare-earth vacancies.

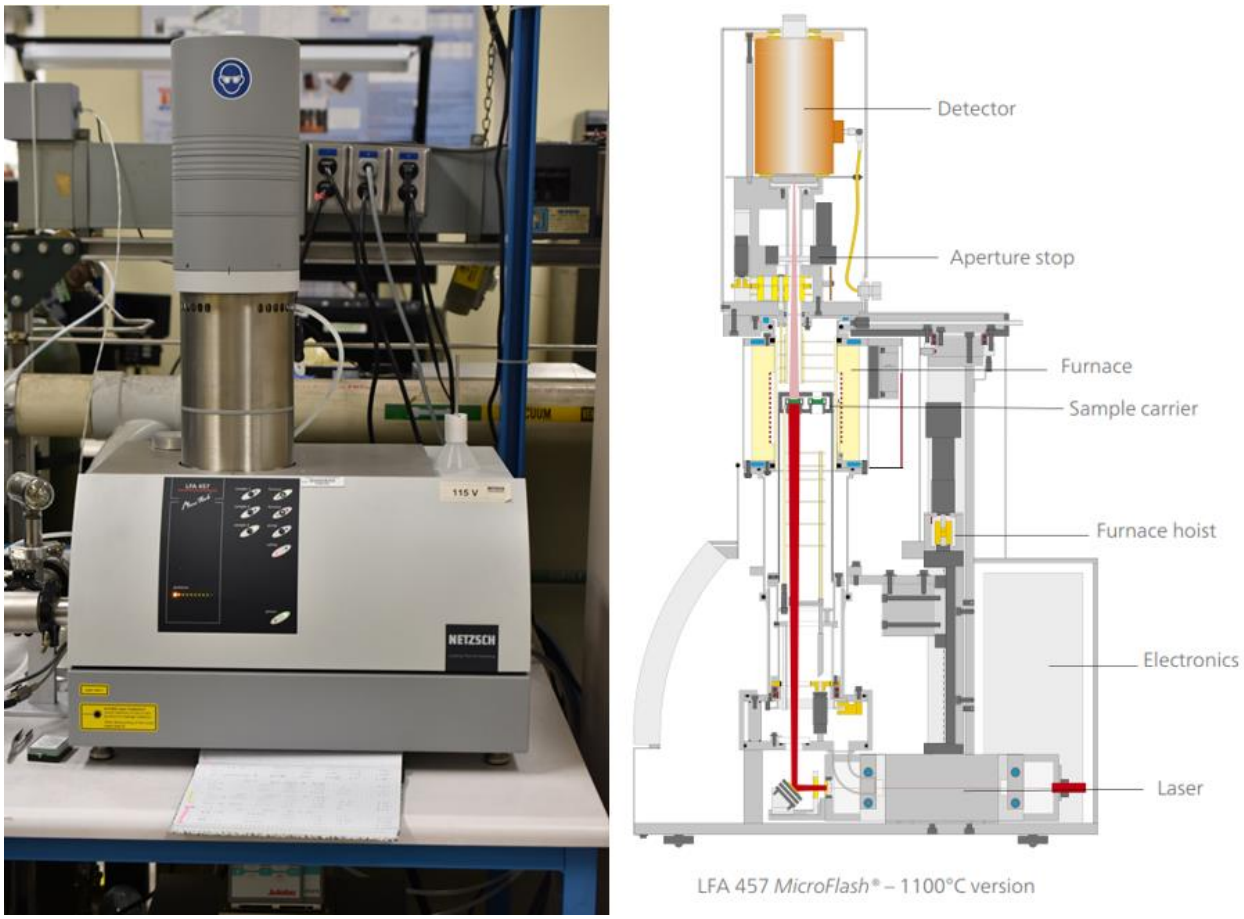

Figure 3.10. Netzsch LFA 457 MicroFlash thermal diffusivity instrument, including outside (left) and inside schematic (right)

A Nanoindenter, also at UCLA, was utilized to collect hardness measurements. The following method was used: Continuous stiffness method (CSM) with standard hardness, modulus and indenter tip calibration. The surface depth limit and strain rate were set to 2000nm and 0.05 respectively.[31] This approach can be used to derive elastic modulus and hardness by using stiffness and the load-and-unload curve measured by the CSM. Stiffness can be related to indentation force and depth, and the loading curve gradient is the gradient of the change in force and the square of the displacement. Shear and longitudinal moduli measurements using an ultrasound with a

customized measurement method were conducted at JPL (in collaboration with Dr. Douglas Hofmann) to assist with further mechanical analysis.[32] This method used reflection mode, in which the transducer performed the sending and receiving of the ultrasonic pulsed waves, and times taken for the waves to propagate through the samples were recorded.

3.3. Compositional and Structural Analysis for $La_{3-x}Pr_xTe_4$

Rietveld refinement analysis was performed to determine the success of alloying Pr atoms within the $La_{3-x}Te_4$ matrix and to calculate the differences in lattice parameters across the alloy. The diffraction pattern for the 5% $La_{3-x}Pr_xTe_4$ sample is representative of the other samples, as shown in Figure 3.11.

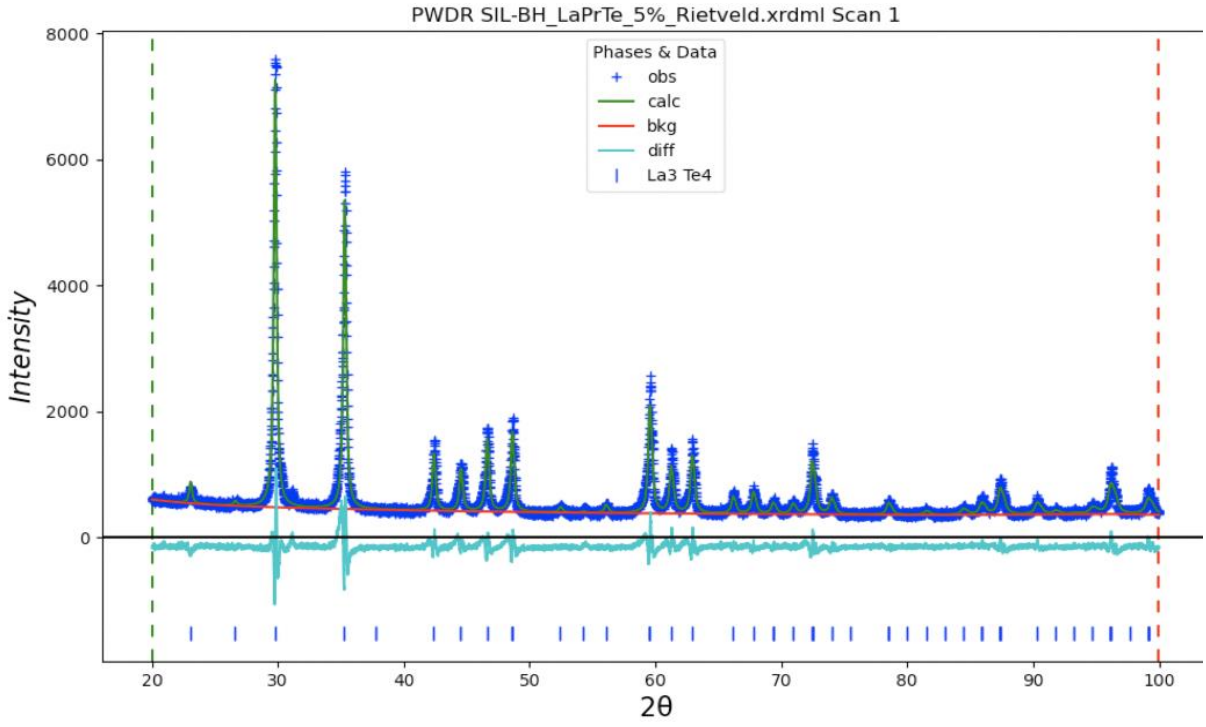

Figure 3.11. Rietveld refinement for 5% $La_{3-x}Pr_xTe_4$ sample with the calculated pattern, difference curve, and observed peaks are shown (indicated by green and light blue lines and blue check marks respectively)

To determine the lattice parameters, the deviation in diffraction angle from the theoretical Bragg position was studied; it has been previously shown that the fitting accuracy of lattice parameters is directly related to the well producibility of the peak shift.[33] The calculated lattice parameter for the 5% $La_{3-x}Pr_xTe_4$ alloy was 9.61 Å, which is slightly smaller than the lattice for La_3Te_4 (9.71 Å). As mentioned previously, to perform a stable refinement of the La occupancy, the occupancy on the Te position was held at 100% as no vacancies were expected. The determination of site-occupancy data for binary compounds by Rietveld refinement is a well-established procedure, and is thoroughly explained in literature.[34] This indicates an La occupancy of around 90.7%, which is slightly lower than expected but may be due to the refinement not accounting for the oxide phase present. To quantitatively evaluate the best fit of the data, the most well-accepted factors are the weighted-profile R_{wp}, which establishes the criterion of fit for the refinement, and goodness-of-fit, S, which is another useful reliability factor. Traditionally, lower R_{wp} and S values indicate a reliable fit. For all of the samples, the R_{wp} and S values were between 0.650-0.893% and 1.3-2.2 respectively, thus highlighting satisfactory fits. No secondary or oxide phases were detected, and the patterns correlate well with the parent La_3Te_4 and Pr_3Te_4 compounds.

Phase homogeneity of the samples was further verified by the use of backscattered electron (BSE) SEM on samples consolidated by SPS. Micrographs for all samples are shown in Figure 3.12. These images were typical of all samples and the uniform contrast reflects the phase homogeneity of the compounds. The dark areas in Figure 3.11 stem from trace amounts of residual porosity in the samples and the porosity was calculated to be between 2-5% using ImageJ analysis.

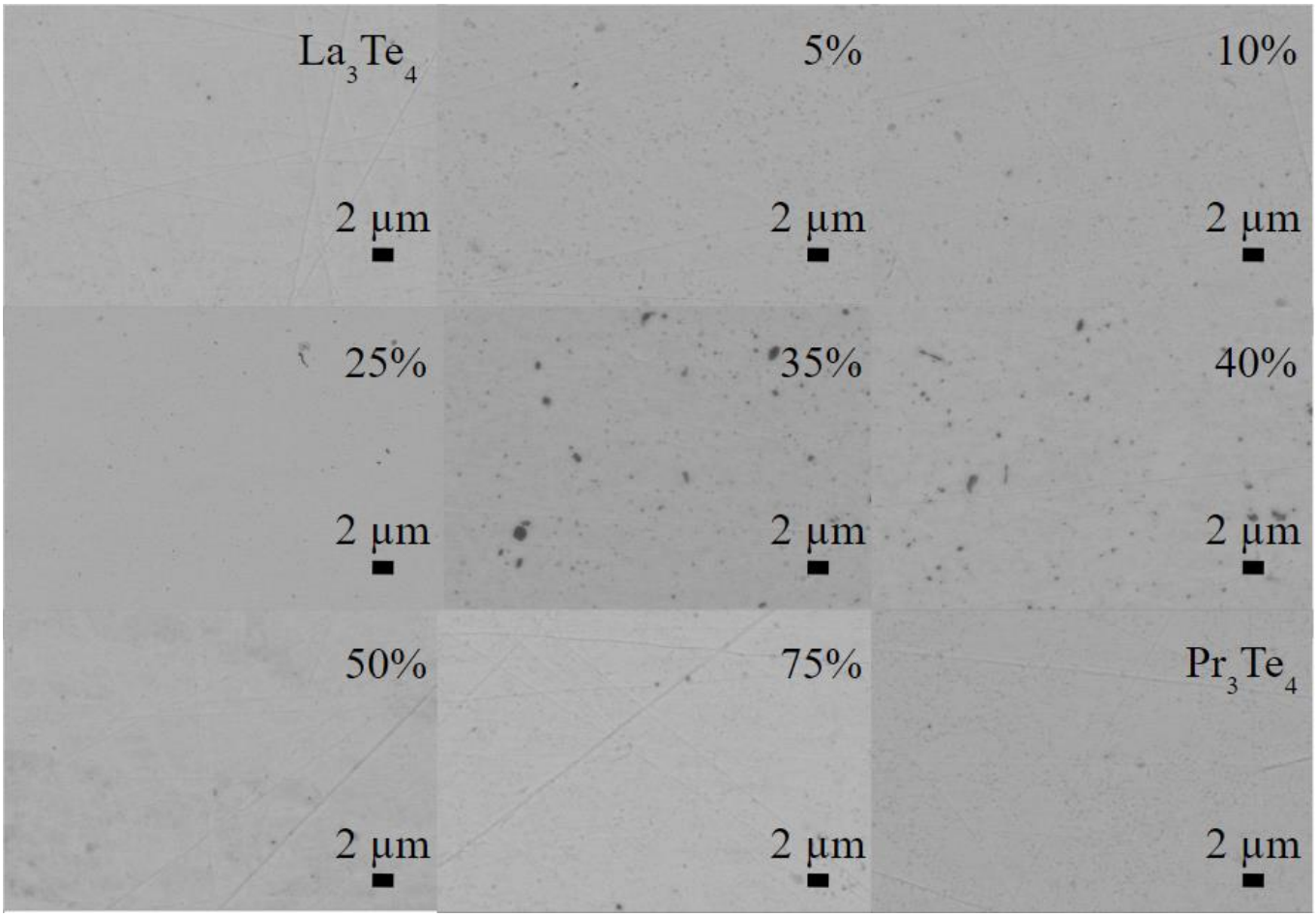

Figure 3.12. BSE SEM images of homogeneous $La_{3-x}Pr_xTe_4$ compacts. The dark regions are from residual porosity in the samples

3.4. Thermoelectric Properties of $La_{3-x}Pr_xTe_4$

Figure 3.13 showcases the resistivity measurements for the alloys as a function of temperature and composition. The end members (La_3Te_4 and Pr_3Te_4) have very similar resistivity measurements, and the alloys represent a range in resistivity. Generally, resistivity decreases up to 25%, then it increases; however, all of the resistivity measurements are within a very similar range.

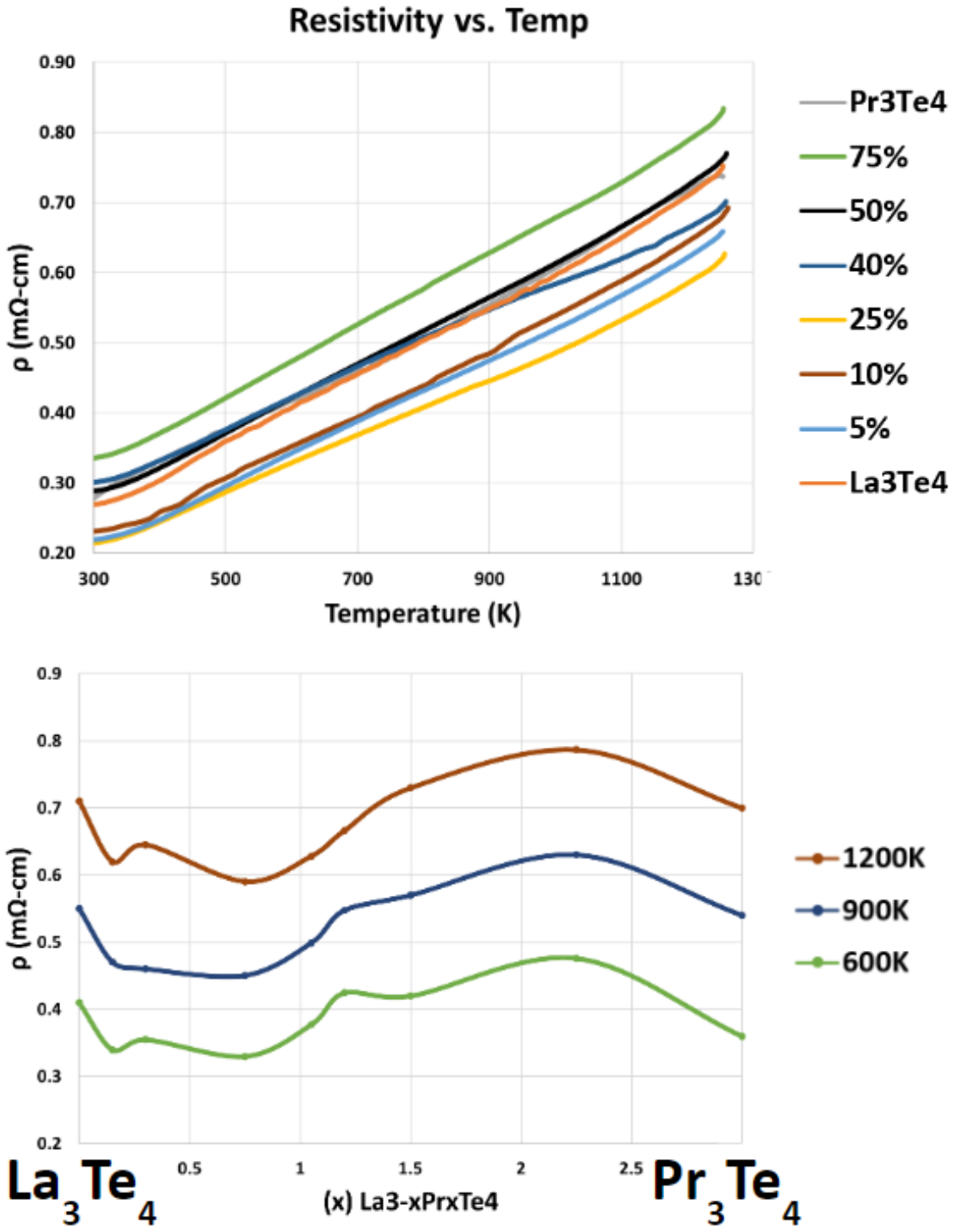

Figure 3.13. Resistivity of $La_{3-x}Pr_xTe_4$ as a function of temperature (top) and composition (bottom)

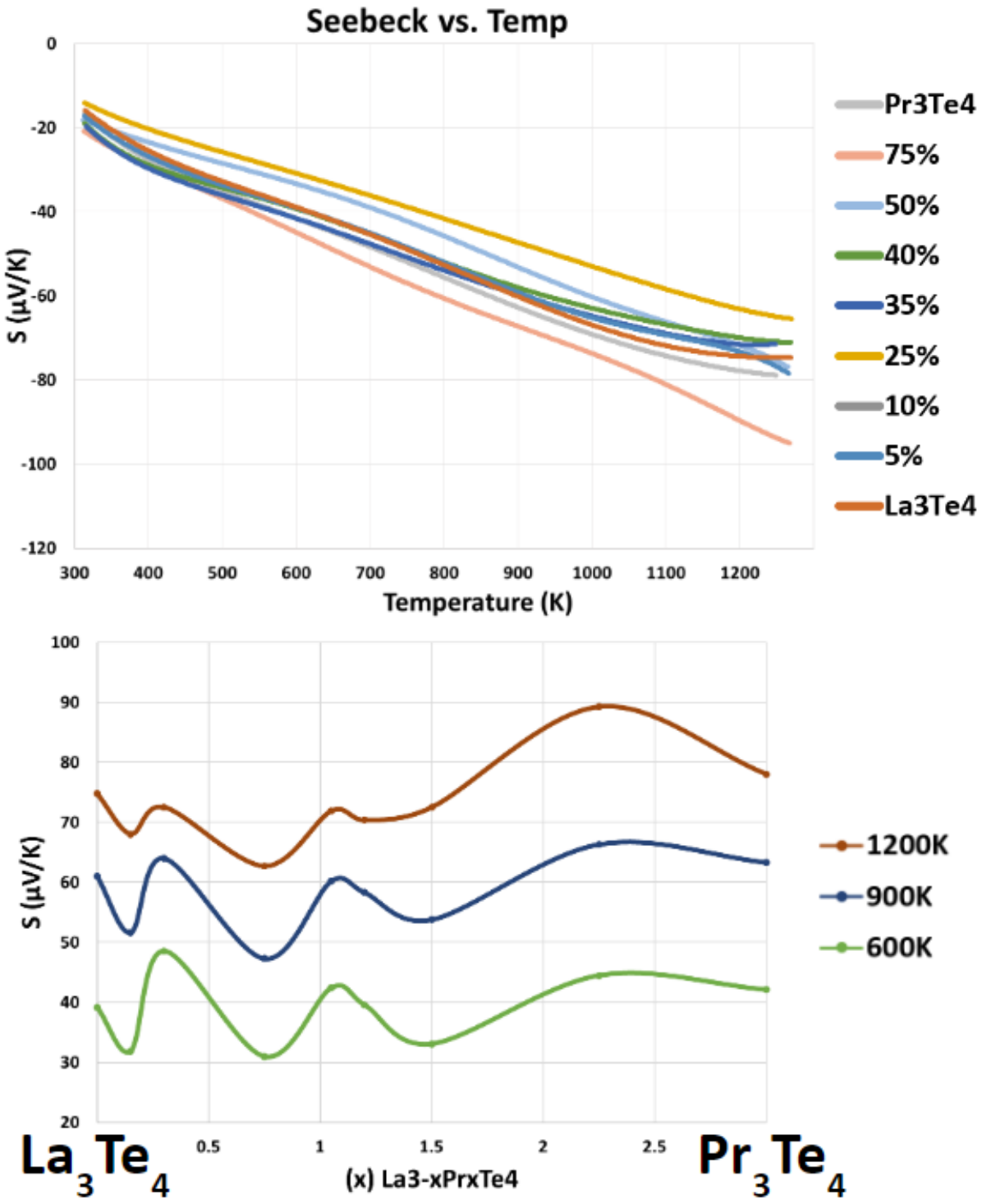

Figure 3.14. Seebeck coefficient of $La_{3-x}Pr_xTe_4$ as a function of temperature (top) and composition (bottom)

Figure 3.14 showcases the Seebeck measurements for the alloys. It's important to note the similarities in trends between resistivity and Seebeck; in this case, both of the end members have similar values once again, and the alloys display a range of values within that. Once again, there is a general decrease in Seebeck up to 25%, then an increase.

I believe that this trend of decreasing and increasing seen with the electronic properties can be attributed to alloy scattering. Alloy scattering refers to a random distribution of different atoms on the same lattice site resulting in a reduction of mobility.[35] This effect can even be seen with small percentages of substitution, then ultimately increases and reaches saturation at the end members (see example in figure 3.15).[36] This figure serves as an example of how drift mobility is affected by alloying, which is also taking place with the $La_{3-x}Pr_xTe_4$ system.

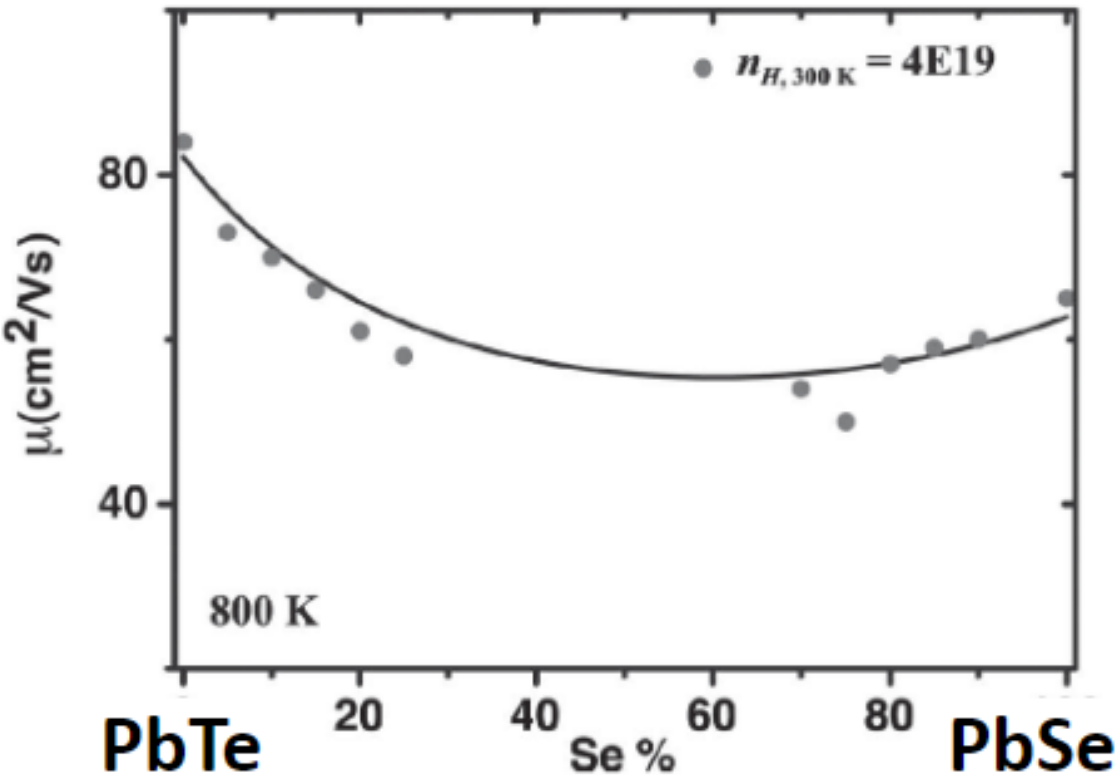

Figure 3.15. Drift mobility at 800K for $(PbTe)_{1-x}(PbSe)_x$ solid solutions

In the simple free electron (single parabolic band) Drude-Sommerfeld model, the weighted mobility is the drift mobility weighted by the density of states $g \propto (m^*)^{3/2}$:

$$\mu_W = \mu \left(\frac{m_s^*}{m_e} \right)^{\frac{3}{2}} \quad \textbf{Equation 3.2}$$

Where g is the density of states, μ_w is weighted mobility, μ is drift mobility, m_s^* is the density of states effective mass and m_e is the effective mass of an electron.

Drift mobility is the simple degenerate limit of the Drude-Sommerfeld model, and thus, drift mobility decreases with charge carrier concentration. The weighted mobility, however, is considered a non-degenerate value for mobility and does not change for samples with different doping. Analysis of the weighted mobility can elucidate the electronic structure and scattering mechanisms in materials and is particularly helpful in understanding and optimizing thermoelectric materials.[37]

The weighted mobility can be calculated from Seebeck and resistivity measurements using the following equation:

$$\mu_{\mathrm{w}} = 331 \frac{\mathrm{cm}^2}{\mathrm{Vs}} \left(\frac{m\Omega\mathrm{cm}}{\rho} \right) \left(\frac{T}{300\mathrm{K}} \right)^{-3/2} \left[\frac{\exp\left[\frac{|S|}{k_{\mathrm{B}}/e} - 2 \right]}{1 + \exp\left[-5\left(\frac{|S|}{k_{\mathrm{B}}/e} - 1 \right) \right]} + \frac{\frac{3}{\pi^2} \frac{|S|}{k_{\mathrm{B}}/e}}{1 + \exp\left[5\left(\frac{|S|}{k_{\mathrm{B}}/e} - 1 \right) \right]} \right] \quad \textbf{Equation 3.3}$$

Here ρ is the electrical resistivity, T is the absolute temperature, S is the Seebeck coefficient, and k_B/e =86.3 μV/K.

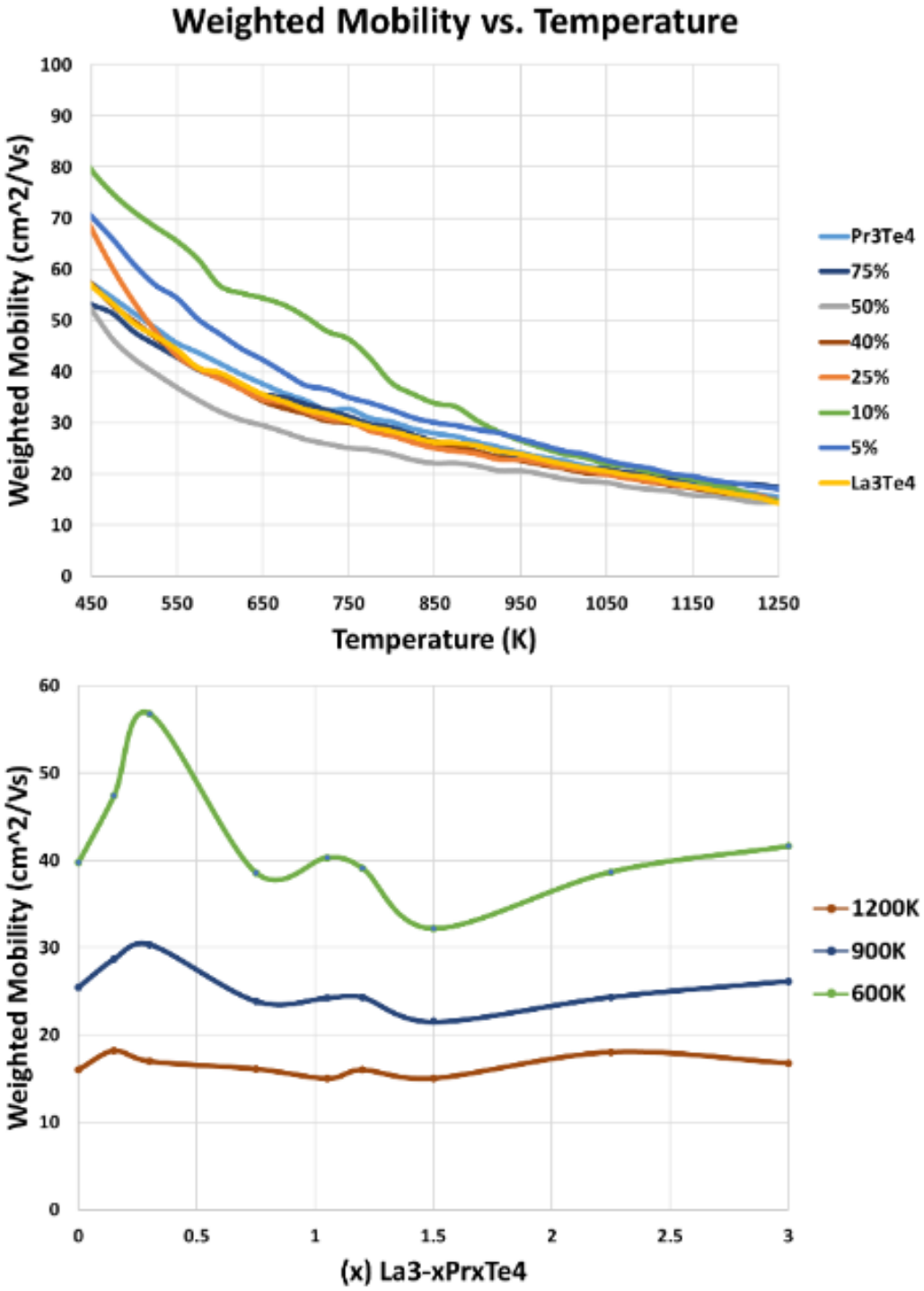

Figure 3.16. Weighted mobility of $La_{3-x}Pr_xTe_4$ as a function of temperature (top) and composition (bottom)

Weighted mobility can be used to identify charge transport mechanisms by examining the temperature dependence.[38] Overall there is a reduction in weighted mobility for the system with respect to temperature. Across the compositions, there are distinct differences in weighted mobility at lower temperatures across doping levels, but at higher temperatures the weighted mobilities are similar (see Figure 3.16).

It is expected that weighted mobility will decrease with temperature due to increased phonon scattering.[37] Weighted mobility can be used to compare experimental properties of materials to decide if different properties are due to differences in doping, electronic structure or scattering. Ideal materials that follow the single parabolic band model with a single parabolic band will have a weighted mobility that does not change with doping; any differences could be a sign of complexity in the band structure or scattering, such as non-parabolic bands or multiple bands.[38]

This reduction in weighted mobility gives insight about the band structure of the alloys; there is a slight increase in mobility with alloy concentrations below 25%, so those alloys could potentially be activating another band. This discussion of weighted mobility relies on single parabolic band and scattering assumptions; if these alloys diverge from this model, that would imply another band (or potentially multiple bands) within the band structure are being activated.

It is extremely important to investigate whether the weighted mobility of the alloys (which for the sake of simplicity is primarily assessed with Seebeck data) strays from the single parabolic band model. To accomplish this, the sample with the greatest weighted mobility deviation (10% alloy) was plotted against the Atiyah-Patodi-Singer (APS) boundary condition, as shown in Figure 3.17. This model was produced in collaboration with Max Wood's Seebeck data analysis website.[39]

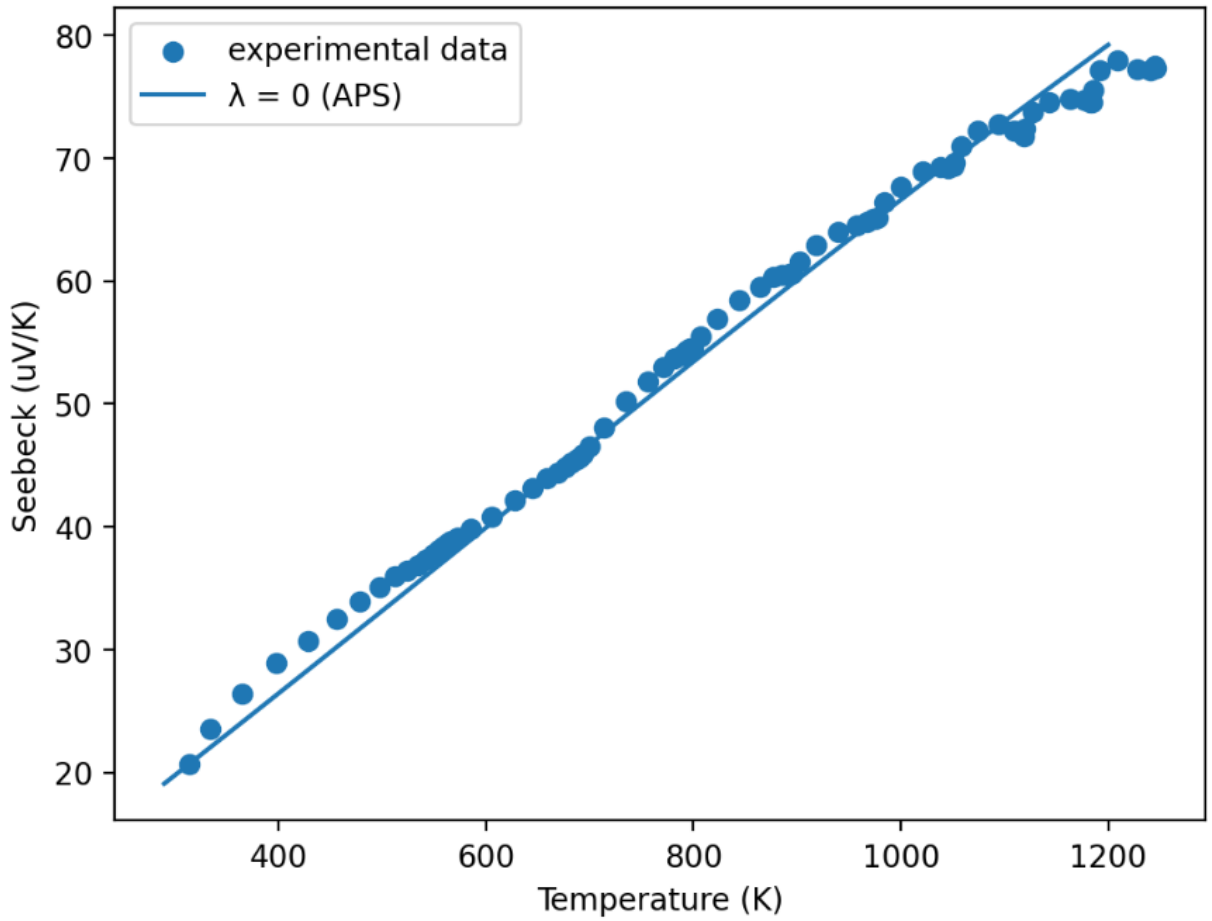

Figure 3.17. $La_{3-x}Pr_xTe_4$ 10% alloy plotted against the Atiyah-Patodi-Singer (APS) boundary condition for band structures

The Atiyah-Patodi-Singer (APS) model is a specific energy-band condition that we're applying to the Fermi-Dirac distribution.[40] It gives insight into the band edge states and requires that eigenvalues evaluated on the boundary should belong to the subspace of eigenvalues associated with positive or negative eigenvalues for the boundary operator.[41-42] To simplify, if

the following equation provides a solution, there exists an edge state satisfying the APS boundary condition, and the solution therefore satisfies the single parabolic band model:[43]

$$t\sqrt{\frac{t+E_j}{t-E_j}}I_{j-\frac{1}{2}}(\varepsilon_j R)=\left(\frac{j}{R}+\sqrt{\frac{j^2}{R^2}+t^2}\right)I_{j+\frac{1}{2}}(\varepsilon_j R) \quad \textbf{Equation 3.4}$$

Here, (E,t) denotes the parameter pair belonging to the domain defined by $|E_j|<|t|$. These parameters are defined by Cartesian coordinates and eigenvalue equations that are extensive and beyond the scope of this work.

Based on the APS boundary condition, which corresponds to the single parabolic band model, theoretical Seebeck values as a function of temperature were evaluated against the experimental Seebeck values for the $La_{3-x}Pr_xTe_4$ 10% alloy. Because we see a good correlation between the experimental data and the boundary condition, it can be concluded that the $La_{3-x}Pr_xTe_4$ alloys correspond well to the single parabolic band model and have no indications of complexity in the band structure or scattering.

The thermal conductivity of the alloys was calculated by multiplying the measured thermal diffusivity of the alloys, the density of the alloys determined by the Archimedes method, and the adjusted heat capacity of the alloys as shown in the following equation:

$$adjusted\ Cp\ \left({}^{J}/_{g/k}\right)=\frac{MW_{alloy}*Cp_{La_3Te_4}}{MW_{La_3Te_4}} \quad \textbf{Equation 3.5}$$

This equation correlates to the rule of mixtures, wherein the alloy properties are proportional to the starting material (in this case, La_3Te_4).

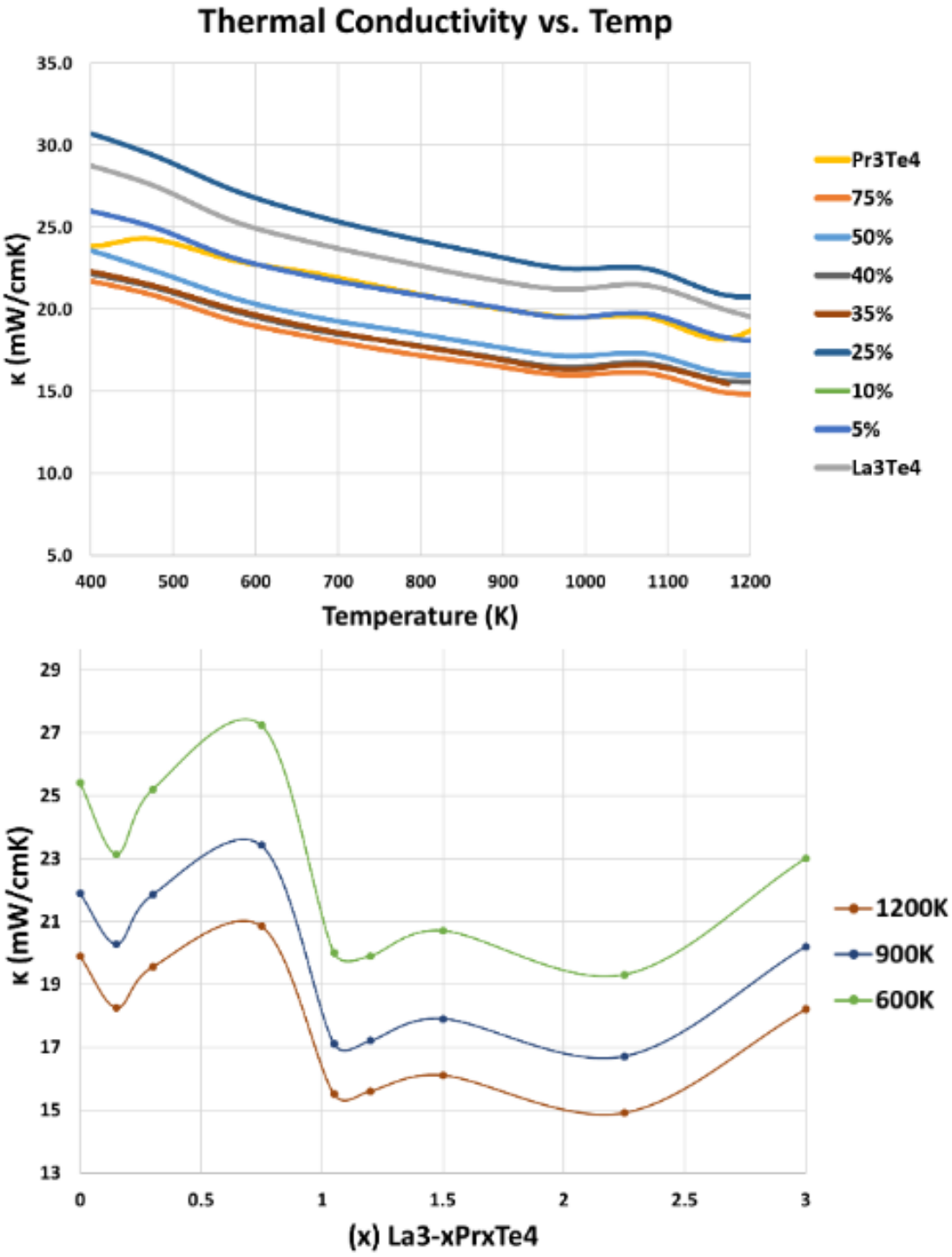

Figure 3.18. Thermal conductivity of $La_{3-x}Pr_xTe_4$ as a function of temperature (top) and composition (bottom)

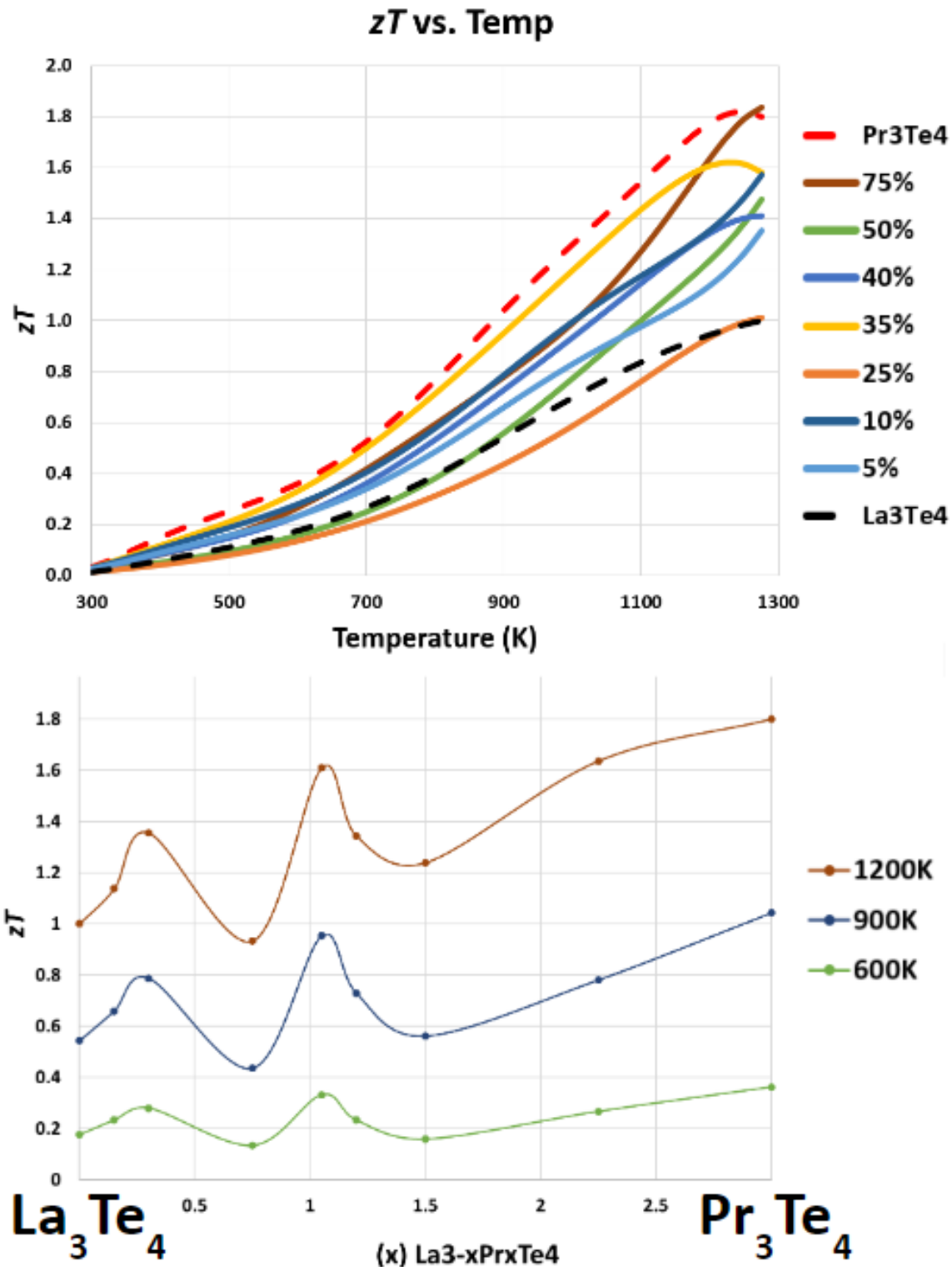

Figure 3.19. *ZT* of $La_{3-x}Pr_xTe_4$ as a function of temperature (top) and composition (bottom)

Thermal conductivity (shown in Figure 3.18) calculated according to the rule of mixtures shows an increase in thermal conductivity up to 25%, then decreases. Taking into consideration all of the electronic and thermal properties, *ZT* for this alloy system was calculated (Figure 3.19). According to the calculated *ZT* measurements, the end members Pr_3Te_4 and La_3Te_4 represent the highest and lowest average *ZT* values respectively. The *ZT* values for the alloys reside in between the two, with no discernible trend noted. These results correlate with the scientific understanding of the rule of mixtures, in which the properties of the alloys lie between the two starting materials (La_3Te_4 and Pr_3Te_4).

Part of our hypothesis included seeing improvements in mechanical properties as a result of solid solution strengthening, in which lattice strain produces a reduction in dislocation mobility, which is hypothesized to strengthen the alloys.[5-7]

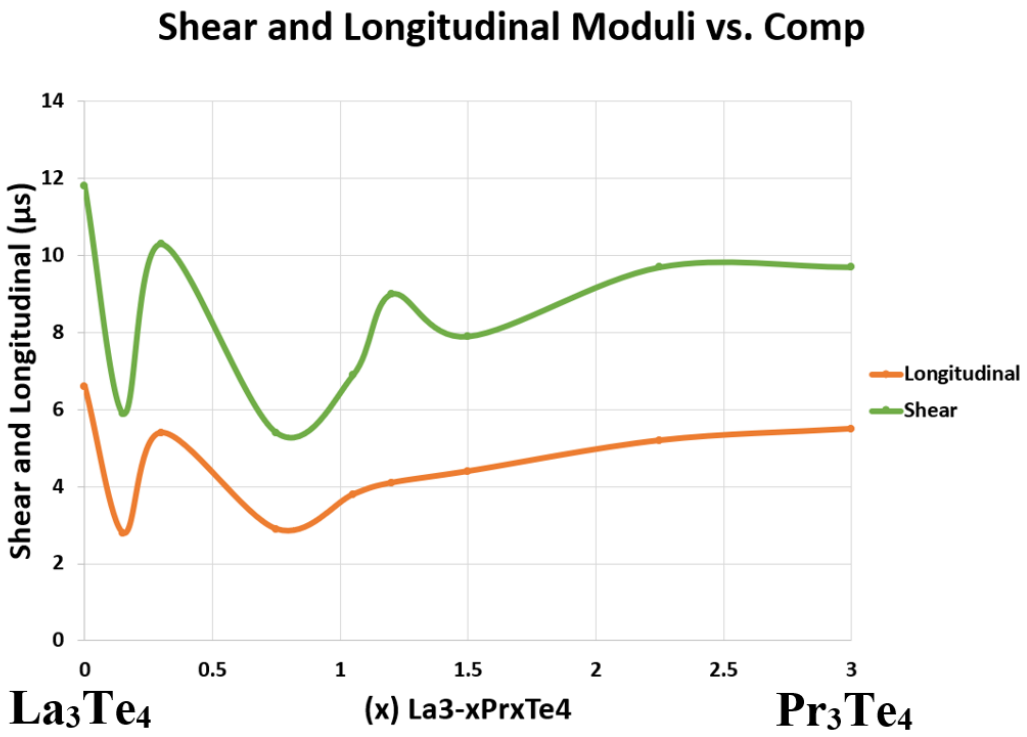

Figure 3.20. Shear and longitudinal moduli as a function of composition

Shear and longitudinal moduli were collected via ultrasound testing, a non-destructive testing technique to determine the propagation of ultrasonic waves in the alloys. These measurements help to qualitatively determine the dislocation density of the materials, as it has been shown that dislocations interact with sound waves.[44] Intuitively, a higher dislocation density would lead to lower dislocation mobility and therefore indicate an increase in the hardness of the material.[45] The times taken for the waves to propagate through the samples in both directions (shear and longitudinal) are recorded in Figure 3.20. There is no discernible trend across the alloys; however, there is a 50% decrease in both shear and longitudinal moduli from La_3Te_4 to the $La_{3-x}Pr_xTe_4$ 5% sample, which then increases again with the 10% sample and decreases again with the 25% sample. These differences in ultrasound measurements are indicative of differences in dislocation density; the longer shear and longitudinal times would indicate that these sound waves are being scattered by dislocations, thus indicating that these are relatively harder materials. Conversely, materials with shorter shear and longitudinal times have lower dislocation densities, and are therefore relatively less hard materials.

Shear and Longitudinal modulus measurements correlate to the speed of sound, which related to thermal conductivity as shown in the following equation:

where thermal conductivity (λ) is related to a constant (L), speed of sound (u) as well as the

$$\lambda = Lu(C_p\rho) \quad \textbf{Equation 3.6}$$

molar heat capacity (Cp) and density (ρ).[15] With this correlation, we see there is a similar trend between the shear and longitudinal moduli and the measured thermal conductivity (see Figure 3.21).

As we increase the percentage of Praseodymium within the La_3Te_4 matrix, there is a drastic decrease with the $La_{3-x}Pr_xTe_4$ 5% sample, followed by an increase with the 10% alloy in shear and longitudinal moduli and thermal conductivity, followed by another decrease with the 25% sample with another small change in slope, resulting in a much smaller increase past 50%. Note that the thermal conductivity is composed not only of the molar heat capacity and density, but also the thermal diffusivity; this can account for the small variations noted with the trends (especially around the 10% and 25% samples).

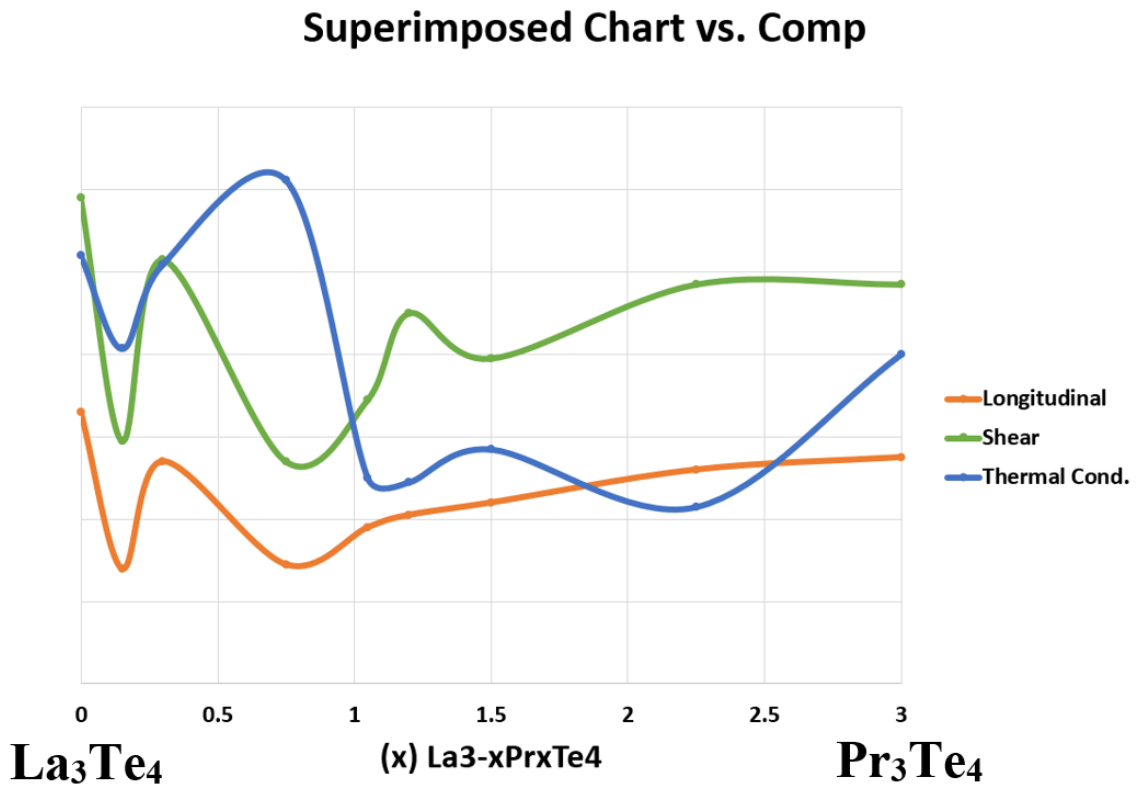

Figure 3.21. Shear and longitudinal moduli and thermal conductivity as a function of composition

Hardness measurements were also collected via a nanoindenter to detect any significant changes across the alloy. As previously stated, a reduction in dislocation mobility is hypothesized to strengthen the alloys; the ultrasound measurements gave insight into dislocation

density for each alloy and the end members. Results indicate that samples with higher shear and longitudinal moduli are due to sound wave scattering by dislocations (aka higher dislocation density), and thus lower dislocation mobility, resulting in relatively greater hardness for those materials. The measured hardness values are shown in Figure 3.22. Due to the margin of error associated with these measurements, no significant differences in hardness can be concluded. However, further analysis of mechanical properties of rare earth tellurides are shown in Appendix B.

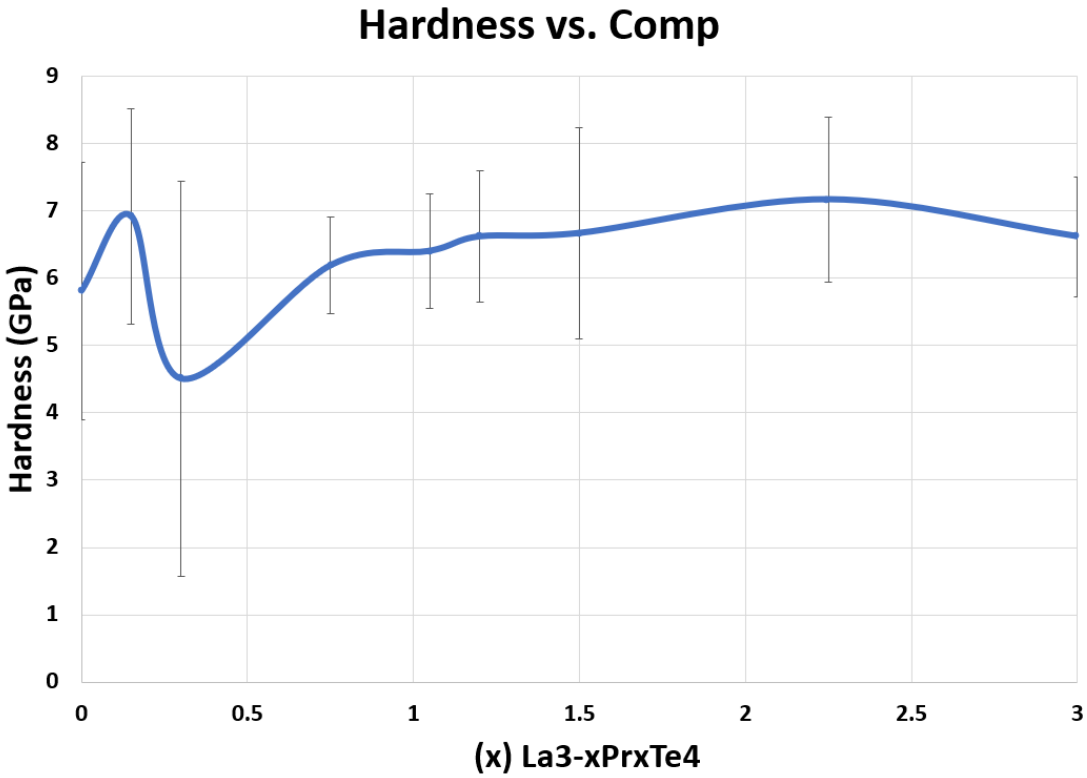

Figure 3.22. Hardness measurements of $La_{3-x}Pr_xTe_4$ as a function of composition

Results indicate that there are distinctive differences in electronic properties across the alloys, whereas there is a minimal change in thermal conductivity with respect to the end members. This may be due to the $La_{3-x}Pr_xTe_4$ system reaching a "glassy limit". This implies that the diffusion-mediated thermal transport, also known as the minimal thermal conductivity within

a system, has already been achieved, and alloying within the system does not provide any added benefits. Vast improvements in thermoelectric materials have been accomplished by approaching the minimal thermal conductivity for the systems, primarily through alloying.[46-47] Other techniques, such as band convergence and phonon scattering, have produced a similar effect.[48-49]

To verify this claim, the minimal thermal conductivity was calculated using the following equation:[50]

$$\kappa_{\text{diff}} \approx 0.76 n^{\frac{2}{3}} k_{\text{B}} \frac{1}{3}(2v_{\text{T}} + v_{\text{L}}) \quad \textbf{Equation 3.7}$$

Here, k_{diff} corresponds to the limit of entirely diffusive (diffusion mediated) thermal transport, k_B corresponds to the Boltzmann constant, and v_T and v_L corresponds to the transverse and longitudinal moduli respectively. *n* refers to the density of atoms and is calculated by the following equation:

$$(n = \frac{\#\,\text{atoms}}{\text{unit cell}} \times \frac{1}{V_{\text{uc}}}) \quad \textbf{Equation 3.8}$$

The calculated room-temperature k_{diff} and the experimental thermal conductivity values are compared in Figure 3.23.

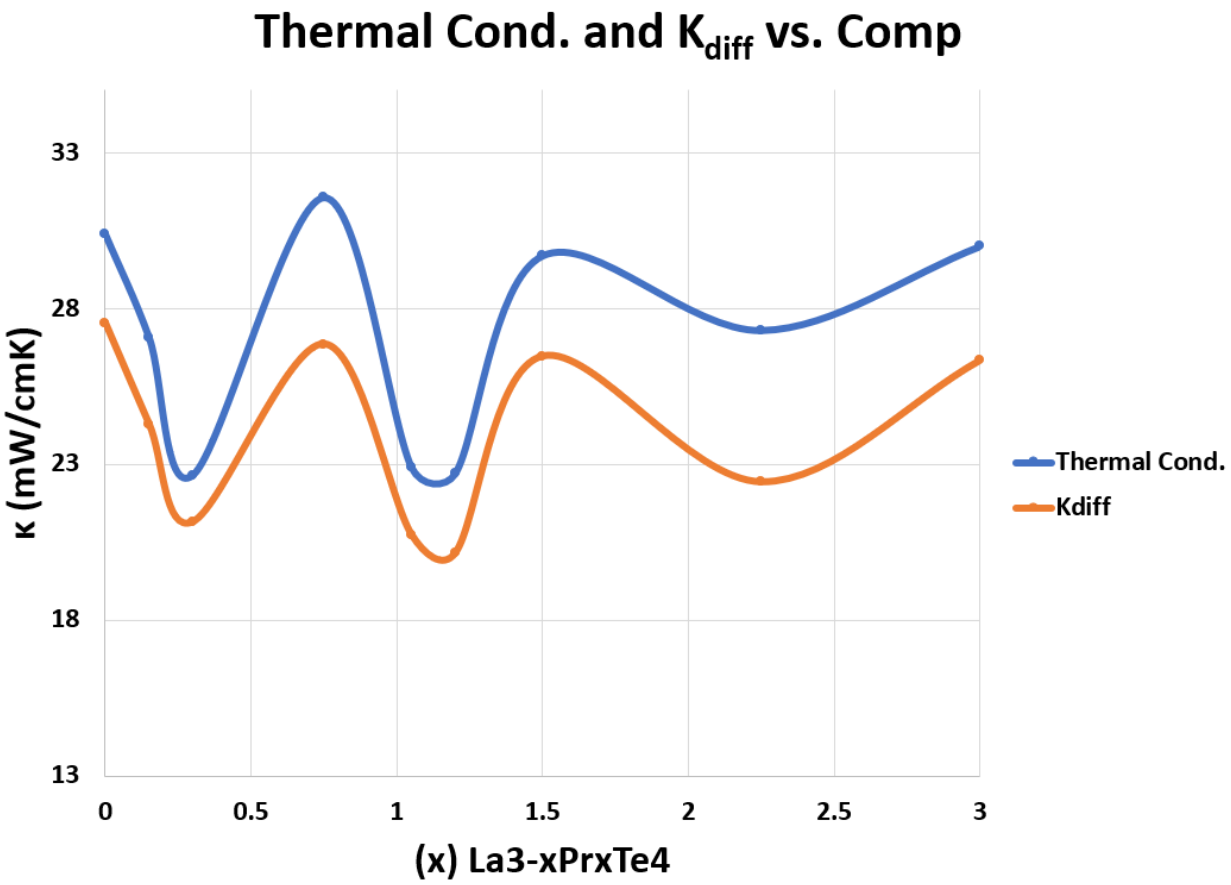

Figure 3.23. Comparison of calculated room-temperature minimal thermal conductivity (k_{diff}) and experimental thermal conductivity values (at room temperature)

There is a close correlation between the calculated minimal thermal conductivity and the experimental thermal conductivity values at room temperature. This illustrates that the "glassy limit" of the alloys has been achieved, and alloying within the system does not provide additional benefits in terms of reducing the thermal conductivity. However, this research illustrates that customization of thermoelectric properties can be achieved by tuning the doping levels within the $La_{3-x}Pr_xTe_4$ system.

3.5. Summary

Significant advancements in our comprehension of rare earth alloys and their effect on electronic and mechanical properties have been achieved through this research. It was hypothesized that alloying in the $La_{3-x}Pr_xTe_4$ system would tune the DOS via f-electrons, which will help reduce thermal conductivity because of point defect scattering. Indeed, there are significant differences in electronic properties across the alloys. Also, the rule of mixtures was scientifically proven due to the alloy thermoelectric properties residing between the properties of the end members. It was also hypothesized that alloying would improve mechanical properties via solid solution strengthening. Ultrasound measurements were successfully utilized to qualitatively determine the correlation between dislocation density and dislocation mobility, as well as their relation to material hardness. Hardness measurements indicate that the end members and the alloys all have similar hardness values within error.

3.6. References

[1] Cheikh, Dean, Hogan, Brea *et al*, "Praseodymium Telluride: A High-Temperature, High *ZT* Thermoelectric Material" , *Joule* 2, **2018**, https://doi.org/10.1016/j.joule.2018.01.013

[2] Cheikh, Dean. Synthesis and Characterization of Rare-Earth Tellurides and Their Composites For High-Temperature Thermoelectric Applications. UCLA, **2017**, 58–59, https://escholarship.org/uc/item/1ng766qh

[3] Chen, Zhiwei, Zhengzhong Jian, et al. "Lattice Dislocations Enhancing Thermoelectric PbTe in Addition to Band Convergence." *Advanced Materials*, 29, 23, **2017**, https://doi.org/10.1002/adma.201606768

[4] Zheng, Linglang, et al. "Interstitial Defects Improving Thermoelectric SnTe in Addition to Band Convergence." *ACS Energy Letters*, 2, 3, **2017**, 563–68, https://doi.org/10.1021/acsenergylett.6b00671

[5] Gao, L., et al. "Solid Solution Strengthening Behaviors in Binary Mg–Y Single Phase Alloys." *Journal of Alloys and Compounds*, 472, 1–2, **2009**, 234–40, https://doi.org/10.1016/j.jallcom.2008.04.049

[6] Shi, B. Q., et al. "Solid Solution Strengthening in Polycrystals of Mg–Sn Binary Alloys." *Journal of Alloys and Compounds*, 509, 7, **2011**, 3357–62, https://doi.org/10.1016/j.jallcom.2010.12.065

[7] Liu, Xiqin, et al. "First-Principles Study of Solid Solution Strengthening in Mg–X (X=Al, Er) Alloys." *Bulletin of Materials Science*, 42, 1, **2019**, https://doi.org/10.1007/s12034-018-1687-y

[8] Hu, Bo, et al. "Solid Solution Strengthening Mechanism in High Pressure Die Casting Al–Ce–Mg Alloys." *Materials Science and Engineering: A*, 812, **2021**, 141109, https://doi.org/10.1016/j.msea.2021.141109

[9] Mo, Ning, et al. "Understanding Solid Solution Strengthening at Elevated Temperatures in a Creep-Resistant Dilute Mg-Gd-Ca Alloy." *SSRN Electronic Journal*, **2019**, https://doi.org/10.2139/ssrn.3441466

[10] Huang, Wen-sen, et al. "Solid Solution Strengthening and Damping Capacity of Mg−Ga Binary Alloys." *Transactions of Nonferrous Metals Society of China*, 32, 9, **2022**, 2852–65, https://doi.org/10.1016/s1003-6326(22)65988-0

[11] Suryanarayana, Cury. "Mechanical Alloying And Milling". *CRC Press*, **2004**, http://dx.doi.org/10.1201/9780203020647

[12] Keviczky, L., et al. "Mathematics and Control Engineering of Grinding Technology: Ball Mill Grinding". *Springer Science & Business Media*, **2012**, https://doi.org/10.1007/978-94-009-2249-5

[13] Pickhardt, Wilm, et al. "Direct Mechanocatalysis: Using Milling Balls as Catalysts." *Chemistry – A European Journal*, 26, 57, **2020**, 12903–11, https://doi.org/10.1002/chem.202001177

[14] Zhang, Zhao-Hui, et al. "The Sintering Mechanism in Spark Plasma Sintering – Proof of the Occurrence of Spark Discharge." *Scripta Materialia*, 81, **2014**, 56–59, https://doi.org/10.1016/j.scriptamat.2014.03.011

[15] Cavaliere, Pasquale. "Spark Plasma Sintering of Materials: Advances in Processing and Applications". *Springer*, **2019**, https://doi.org/10.1007/978-3-030-05327-7

[16] Cao, Giacomo, et al. "Spark Plasma Sintering: Current Status, New Developments and Challenges: A Review of the Current Trends in SPS". *Elsevier*, **2019**, https://doi.org/10.1016/C2018-0-02428-7

[17] Toby, Brian H., and Robert B. Von Dreele. "GSAS-II: The Genesis of a Modern Open-Source All Purpose Crystallography Software Package." *Journal of Applied Crystallography*, 46, 2, **2013**, 544–49, https://doi.org/10.1107/s0021889813003531

[18] Von Dreele, Robert B. "The Development of GSAS-II." *Proceedings of the International Symposium on Crystallography*, Editora Edgard Blücher, **2015**, http://dx.doi.org/10.5151/phypro-sic100-003

[19] Mitarov, R.G., Tikhonov, V.V., Vasil'ev, L.N., Golubkov, A.V., and Smirnov, I.A. Specific heat of Pr_3Te_4 and La_3Te_4. Phys. Status Solidi A *30*, **1975**, 496–500.

[20] Borup, Kasper A., et al. "Measurement of the Electrical Resistivity and Hall Coefficient at High Temperatures." *Review of Scientific Instruments*, 83, 12, **2012**, https://doi.org/10.1063/1.4770124

[21] Peterson, Dirch H., et al. "Micro-four-point Probe Hall Effect Measurement Method." *Journal of Applied Physics*, 104, 10, **2008**, https://doi.org/10.1063/1.2949401

[22] Velicheti, D., et al. "Nondestructive Measurement of Hall Coefficient for Materials Characterization." *Journal of Nondestructive Evaluation*, 36, 49, **2017**, https://doi.org/10.1007/s10921-017-0426-4

[23] Green, M. A., and M. W. Gunn. "Four Point Probe Hall Effect and Resistivity Measurements upon Semiconductors." *Solid-State Electronics*, 15, 5, **1972**, 577–85, https://doi.org/10.1016/0038-1101(72)90159-1

[24] Wood, C., et al. "Measurement of Seebeck Coefficient Using a Light Pulse." *Review of Scientific Instruments*, 56, 5, **1985**, 719–22, https://doi.org/10.1063/1.1138213

[25] Kim, H.J et al. "System to Measure Thermal Conductivity and Seebeck Coefficient for Thermoelectrics." *NASA Langley Research Center Technical Memorandum - Unclassified*, **2012**.

[26] Wang, Hsin, et al. "Transport Properties of Bulk Thermoelectrics—An International Round-Robin Study, Part I: Seebeck Coefficient and Electrical Resistivity." *Journal of Electronic Materials*, 42, 4, **2013**, 654–64, https://doi.org/10.1007/s11664-012-2396-8

[27] Agne, Matthias T., et al. "Phase Transformation Contributions to Heat Capacity and Impact on Thermal Diffusivity, Thermal Conductivity, and Thermoelectric Performance." *Advanced Materials*, 31, 35, **2019**, 1902980, https://doi.org/10.1002/adma.201902980

[28] Beltrán-Pitarch, Braulio, et al. "Measurement of Thermal Conductivity and Thermal Diffusivity Using a Thermoelectric Module." *Measurement Science and Technology*, 28, 4, **2017**, 045902, https://doi.org/10.1088/1361-6501/aa5c30

[29] Wang, Hsin et al. "Transport Properties of Bulk Thermoelectrics: An International Round-Robin Study, Part II: Thermal Diffusivity, Specific Heat, and Thermal Conductivity." *Journal of Electronic Materials*, 42, 6, **2013**, 1073–84, https://doi.org/10.1007/s11664-013-2516-0

[30] Johra, Hicham. *Description of the Laser Flash Analysis Method for Thermal Diffusivity Measurement with the LFA 447*. Department of the Built Environment, Aalborg University, **2019**, http://doi.org/10.54337/aau312969074

[31] Huen, Wai Yeong, et al. "Relationship of Stiffness-Based Indentation Properties Using Continuous-Stiffness-Measurement Method." *Materials*, 13, 1, **2019**, 97, https://doi.org/10.3390/ma13010097

[32] Cafarelli, A., et al. "Speed of Sound in Rubber-Based Materials for Ultrasonic Phantoms." *Journal of Ultrasound*, 19, 4, **2016**, 251–56, https://doi.org/10.1007/s40477-016-0204-7

[33] Snyder et al, "Alloy Scattering of Phonons", *Materials Horizons*, 7, **2020**, 1452, https://doi.org/10.1039/c9mh01990a

[34] Yaqoob, Khurram, et al. "Comparison of the Site Occupancies Determined by Combined Rietveld Refinement and Density Functional Theory Calculations: Example of the Ternary Mo–Ni–Re σ Phase." *Inorganic Chemistry*, 51, 5, **2012**, 3071–78, https://doi.org/10.1021/ic202479y

[35] H. Wang et al, "The Criteria for Beneficial Disorder in Thermoelectric Solid Solutions", *Adv. Funct. Mater.*, 23, **2013**, https://doi.org/10.1002/adfm.201201576

[36] Mehrotra et al, "Atomistic Approach to Alloy Scattering in $Si_{1-x}Ge_x$", Appl. Phys. Lett. 98, **2011**, 173503, https://doi.org/10.1063/1.3583983

[37] Chin et al, "Alloy Scattering and Lattice Strain Effects on the Electron Mobility in In1-xGaxAs, *Solid-State Electronics*, 34, 10, **1991**, 1055-1063

[38] Snyder, G. Jeffrey, et al. "Weighted Mobility." *Advanced Materials*, 32, 25, 2020, https://doi.org/10.1002/adma.202001537

[39] https://xamwood-seebeck-temperature-app-seebeck-temp-app-xwjl7b.streamlit.app/

[40] Iwai, T., and B. Zhilinskii. "Band Rearrangement through the 2D-Dirac Equation: Comparing the APS and the Chiral Bag Boundary Conditions." *Indagationes Mathematicae*, vol. 27, no. 5, Dec. 2016, pp. 1081–106, https://doi.org/10.1016/j.indag.2015.11.010

[41] Kobayashi, Shun K., and Kazuya Yonekura. "Atiyah-Patodi-Singer Index Theorem from Axial Anomaly." *Progress of Theoretical and Experimental Physics*, 2021, https://doi.org/10.1093/ptep/ptab061

[42] Iwai, Toshihiro, and Boris Zhilinskii. "Local Description of Band Rearrangements." *Acta Applicandae Mathematicae*, 137, 1, 2014, 97–121, https://doi.org/10.1007/s10440-014-9992-y

[43] Iwai, Toshihiro, and Boris Zhilinskii. "Change in Energy Eigenvalues Against Parameters." *Trends in Mathematics*, Springer International Publishing, 2016, 233–53, http://dx.doi.org/10.1007/978-3-319-31756-4_19

[44] "The Interaction of Screw Dislocations and Sound Waves." *Proceedings of the Royal Society of London. Series A. Mathematical and Physical Sciences*, 209, 1097, 1951, 278–90, https://doi.org/10.1098/rspa.1951.0203

[45] Barra, Felipe, et al. "The Use of Ultrasound to Measure Dislocation Density." *JOM*, 67, 8, 2015, 1856–63, https://doi.org/10.1007/s11837-015-1458-9

[46] Hu, Jinsuo, et al. "Breaking the Minimum Limit of Thermal Conductivity of Mg3Sb2 Thermoelectric Mediated by Chemical Alloying Induced Lattice Instability." *Small*, 19, 33,. 2023, https://doi.org/10.1002/smll.202301382

[47] Fu, Tiezheng, et al. “Approaching the Minimum Lattice Thermal Conductivity of P-Type SnTe Thermoelectric Materials by Sb and Mg Alloying.” *Science Bulletin*, 64, 14, 2019,. 1024–30, https://doi.org/10.1016/j.scib.2019.06.007

[48] Gillet, Jean-Numa. “Ultralow Thermal Conductivity Minimum in Silicon Supercrystals with Weakly and Strongly Bonded Germanium Nanodots for Thermoelectrics.” *ACS Sustainable Chemistry & Engineering*, 1, 6, 2013, 611–18, https://doi.org/10.1021/sc400020c

[49] Ghosh, Sanyukta, et al. “Enhanced Thermoelectric Performance in the Ba0.3Co4Sb12/InSb Nanocomposite Originating from the Minimum Possible Lattice Thermal Conductivity.” *ACS Applied Materials & Interfaces*, 12, 43, 2020, 48729–40, https://doi.org/10.1021/acsami.0c17254

[50] Agne, Matthias T., Riley Hanus, et al. “Minimum Thermal Conductivity in the Context of Diffuson-Mediated Thermal Transport.” *Energy & Environmental Science*, 11, 3, 2018, 609–16, https://doi.org/10.1039/c7ee03256k

Chapter 4: $PrTe_{1.46}$-Ni Composites

4.1. Introduction

The phenomenon of direct conversion of a temperature difference to electric potential (Seebeck effect) or the electric potential to a temperature difference (Peltier effect) is known as the thermoelectric effect, and the thermoelectric efficiency of a material, as previously mentioned, is given by its dimensionless figure of merit (zT) value which can be expressed via the following equation:

$$ZT = \frac{\sigma \alpha^2}{\kappa} T \qquad \textbf{Equation 4.1}$$

where S is the Seebeck coefficient must increase and the electrical resistivity and thermal conductivity must decrease to improve the efficiency of these materials. However, due to the interdependent nature of these properties, it is challenging to change one property favorably. Extensive work has been performed in this field to achieve the "phonon-glass, electron crystal" phenomenon by exploring the ways to maintain low thermal conductivity at large electrical conductivities.[1] One way to circumvent this issue is to fabricate composite materials; these consist of bulk materials into which nanostructured features have been incorporated. In nano-thermoelectrics, the interconnected physical properties of Seebeck, electrical and thermal conductivity can be decoupled, thus achieving improved ZT values.[2]

Various approaches have been explored to enhance the thermoelectric efficiency by incorporating nanoparticles into the microstructure and improving grain refinements. The concept

of bulk nanocomposite thermoelectrics evolved as a result of combining the ideas of improved bulk and low-dimensional thermoelectric materials and, therefore, retain the superior characteristics of both of these counterparts that results in enhanced efficiency.

As mentioned in the previous chapter, alloying is the classical way to lower thermal conductivity in semiconductors; it can have a significant effect on reducing thermal conductivity while maintaining good charge carrier mobility. However, as seen in my research, there is a lower limit in terms of reducing thermal conductivity, which ultimately restricts *ZT* enhancements. Introducing nanoparticles of a different compound into a thermoelectric bulk matrix material can be a very efficient way to decouple thermoelectric properties. The nanoparticles create additional scattering centers to selectively scatter mid and long wavelength phonons, resulting in a reduction in thermal conductivity.[3] As the nanostructures also scatter charge carriers, any benefit from the nanostructuring can be obtained only if the mean free path (MFP) of phonons is considerably reduced to a greater extent in comparison to the MFP of charge carriers.[2-4] The metal nanoparticle islands act as barriers and obstruct the movement of low-energy electrons through the thermoelectric host material. Only electrons with adequate energy are therefore able to pass through the matrix/inclusion interface, which can facilitate the increase in Seebeck coefficient by lowering thermal conductivity. Table 4.1 compares the maximum *ZT* values for bulk versus nanostructured materials.[5]

The efficiency of the nanoparticle introduced into the matrix is based on a variety of factors which will be further explained, including the following: choice of nanoparticle, nanoparticle diameter, dimensions and volume percentage.

Choice of nanoparticle is an essential component of improving *ZT*, since poor choice could introduce high electrical resistance due to lattice mismatch and potential barriers at the interface between the nanoparticles and the bulk matrix material. It's also important to choose a nanoparticle such that the difference in atomic mass and bond stiffness to the matrix is significant, since these two parameters improve scattering. Soostman et al. noted that InSb-containing samples, which have the largest atomic mass difference with the PbTe matrix, exhibit the lowest lattice thermal conductivity, ~45% lower than pristine PbTe at room temperature.[6]

	Bulk		Nanostructured	
Material	ZT_{max}	Temperature at which ZT_{max} is observed	ZT_{max}	Temperature at which ZT_{max} is observed
Si	0.2	1200	0.7	1200
$Si_{80}Ge_{20}$ (*n*-type)	1.0	1200	1.3	1173
$Si_{80}Ge_{20}$ (*p*-type)	0.7	1200	0.95	1073
$(Bi,Sb)_2Te_3$	0.9	293	1.4	373
$CoSb_3$	0.45	700	0.71	700

Table 4.1. Comparison of maximum *ZT* values for bulk and nanostructured materials[5]

Nanoparticle diameter is another important parameter to consider. Characteristics of phonon scattering can be treated similar to scattering of electromagnetic waves on spherical particles, and can thus fall into two different regimes depending on the particle size and phonon wavelength.

This is described by the following equation:

where q is the wave vector, R is the particle radius, and χ is the size parameter. In the lower limit (aka the Rayleigh regime, $\chi << 1$), then scattering is primarily affected by the differences in atomic mass and bond stiffness as mentioned previously.

$$\chi = qR \quad \textbf{Equation 4.2}$$

For higher values of the size parameter ($\chi >> 1$), scattering is mainly affected by the particle diameter. Dean Cheikh's dissertation focused on the effect of $LaTe_{1.46}$-Ni composites with larger and smaller nickel inclusions. At an equivalent volume fraction, larger nickel particle sizes were found to decrease the thermal conductivity while leaving the power factor unaffected. This resulted in ZT values which were similar to the starting baseline composite used in this study. Composites made with smaller Ni particle size were found to increase resistivity and Seebeck coefficient, while also resulting in a decreased thermal conductivity.[7] Thermoelectric properties for $LaTe_{1.46}$-Ni composites are shown in Figure 4.1.

Nanocomposite dimensionality is another important parameter that has been shown to control Seebeck coefficient and electrical conductivity independently via quantum confinement, improving the density of states (DOS) near Fermi level, leading to the increment of power factor.[8] For example, the low-dimensional morphology and hollow structure bismuth telluride (Bi_2Te_3) nanotubes resulted in a 30% decrease in thermal conductivity with the electrical conductivity much less affected and thus to an increase in the figure of merit of the Bi_2Te_3-based material.[9]

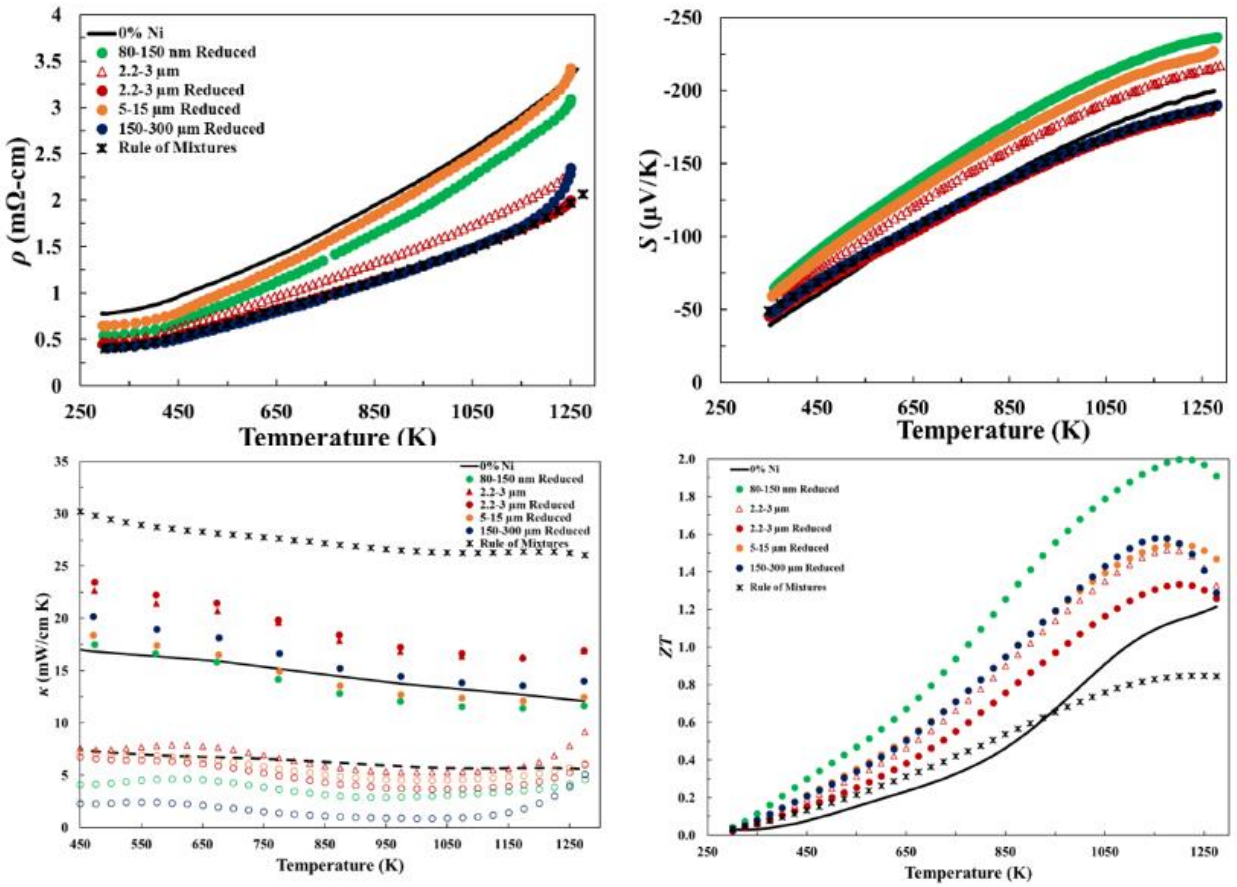

Figure 4.1. Thermoelectric properties of $LaTe_{1.46}$-Ni composites ranging in nanoparticle sizes (a) electrical resistivity, (b) Seebeck coefficient, (c) total thermal conductivity, and (d) dimensionless figure of merit[7]

The effect of volume percentages on nanoparticle thermoelectric performance has also been extensively studied, and the thermoelectric properties of $LaTe_{1.46}$-Ni composites ranging from 0-20 vol% is shown in Figure 4.2.[7,10] The electrical resistivities of the composites remain invariant up to 10 vol% Ni, after which it decreases (Figure 4.2(a)). The Seebeck coefficients of the composites remain unchanged until above 15 vol% loading (Figure 4.2(b)). However, the thermal conductivity begins to increase in composites with Ni loadings greater than 5 vol% (Figure 4.2(c)). As a result, the ZT of the $LaTe_{1.46}$-Ni composites remain at approximately 1.2 until the Ni loading fraction is increased above 15 vol% (Figure 4.2(d)).

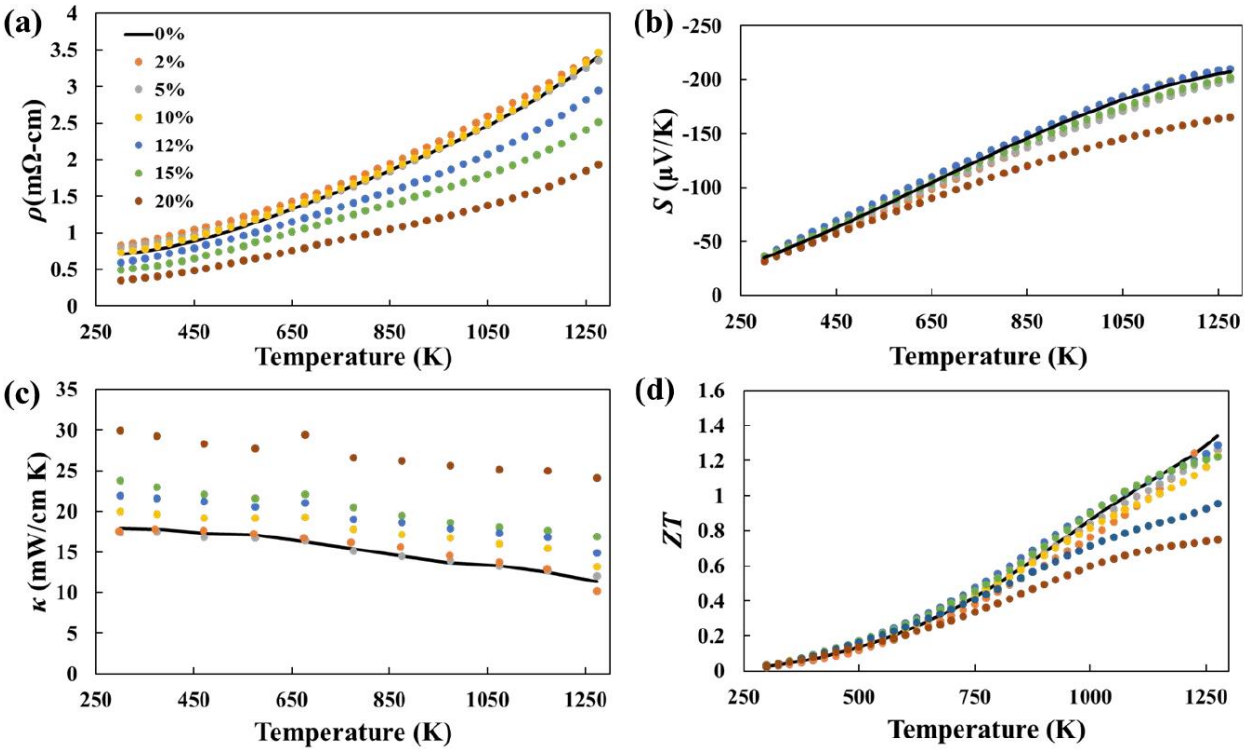

Figure 4.2. Thermoelectric properties of $LaTe_{1.46}$-Ni composites ranging from 0-20 vol%. (a) electrical resistivity, (b) Seebeck coefficient, (c) total thermal conductivity, and (d) dimensionless figure of merit[7, 10]

In this instance, no significant increase in *ZT* was observed; however, a consistent decrease in electrical resistivity is observed with an increase in Ni volume percentage. The primary mechanism responsible for the decrease in electrical resistivity has been referred to as "composite-assisted funneling of electrons (CAFE)" where the decrease is a result of the formation of low resistance pathways formed by the Ni inclusions.[11-15] Because the thermal conductivity of Ni is significantly greater than the $LaTe_{1.46}$ matrix, the Ni particles act as a thermal shunt, thus decreasing the temperature gradient across the inclusions.

In Chapter 3, we discussed the improvements in the Pr_3Te_4 system compared to La_3Te_4 due to the contribution of the *f*-electrons, resulting in the density of states moving closer to the Fermi level, thus improving the Seebeck coefficient and enhancing *zT*. However, Ni composites within

the $PrTe_{1.46}$ have not been previously investigated; thus, this research will discern how the CAFE effect exhibits itself within a $PrTe_{1.46}$ matrix. It is hypothesized that a slight increase in the CAFE effect will take place, where there is a slightly greater decrease in electrical resistivity compared to $LaTe_{1.46}$-Ni composites.

4.2. Experimental

In this study, Praseodymium Telluride was made using a previously reported mechanochemical synthetic procedure with a stoichiometry of $PrTe_{1.46}$ for optimal thermoelectric properties. All manipulations of the starting elements and synthesized powders were handled in an Ar-filled glovebox (H2O < 1 ppm, O2 < 0.1 ppm). Elemental Pr (99.9%, metals basis, HEFA Rare Earth) was combined with Te (99.999%, 5N Plus) and sealed under argon in a stainless steel vial with stainless steel balls. The vial was then placed in a ball mill and milled until a homogeneous $PrTe_{1.46}$ powder was synthesized. The same batch of $PrTe_{1.46}$ parent powder was used for all composites to ensure a constant carrier concentration in the matrix. Ni powders were procured from Alfa Aesar with the following particle sizes: 2.2-3 μm (99.9%, metals basis). The following volume fractions of Ni powder were then milled for 30 minutes with the $PrTe_{1.46}$ powder to disperse homogeneously the Ni particles: 5%, 10%, 15%. The blended powder was loaded into a 12.7 mm graphite die and the powders were compacted through spark plasma sintering (SPS) at temperatures above 1200 °C.

The sintered compacts had densities greater than 98% of the theoretical density, measured using the Archimedes method. Back-scattered electron (BSE) SEM was performed on the composites after sintering to observe the differences in the Ni microstructures, using the same experimental conditions as discussed in previous chapters. The volume fractions of the nickel inclusions were calculated using ImageJ analysis software on the SEM micrographs. Temperature-

dependent electrical resistivity was measured using a combined 4-point probe/Hall effect system. The high-temperature Seebeck coefficient was measured using a custom-fabricated system. Thermal diffusivity measurements were carried out using a commercial Netzsch LFA 457 laser flash analysis system. Extensive discussions of the instrumentation used to collect the experimental data for thermoelectric properties were presented in the previous chapter.

4.3. Results and Discussion

BSE SEM micrographs were collected for milled and pressed $PrTe_{1.46}$-Ni composites with as-received Ni powders (2.2-3 μm). Upon analyzing the microstructure of the composites, it was noted that there was no observable reaction between the nickel particles and the $PrTe_{1.46}$ matrix. The light regions in the images are the $PrTe_{1.46}$ matrix and the dark regions correspond to the Ni inclusions. This contrast is expected due to both Pr and Te having higher atomic numbers (Z) than Ni, which would make them appear brighter in BSE mode. Milling the samples helped to more evenly distribute the particles within the matrices across all volume percentages.

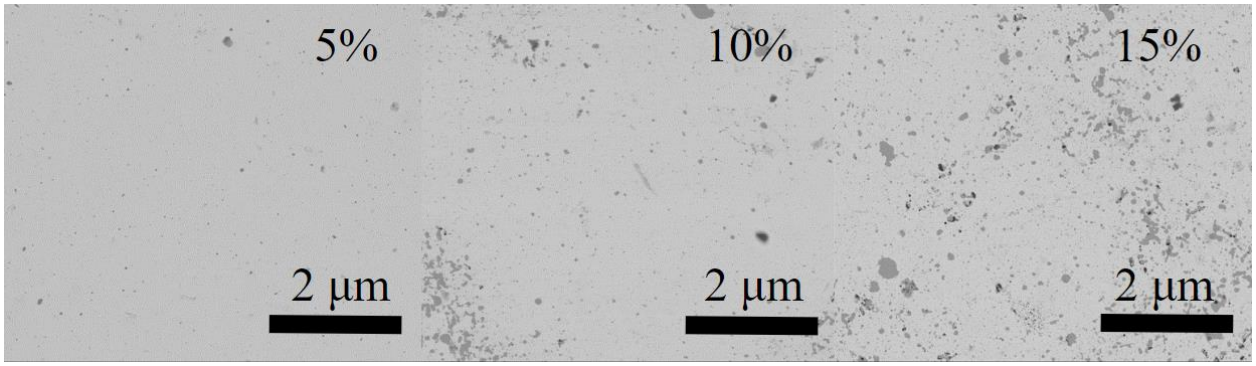

Figure 4.3. BSE SEM micrographs of 2.2-3 μm composites for milled samples at various volume fractions

In Table 4.2, Ni inclusion percentage via area coverage was calculated from SEM micrographs using ImageJ analysis, which match well with the nominal Ni fractions of 5, 10 and 15 vol% respectively.

Targeted Ni Inclusion (%)	Calculated Ni Inclusion (%)
5	4.7
10	11.8
15	14.3

Table 4.2. Ni inclusion percentage calculated from SEM micrographs using ImageJ analysis. The values match well with the nominal Ni volume fractions

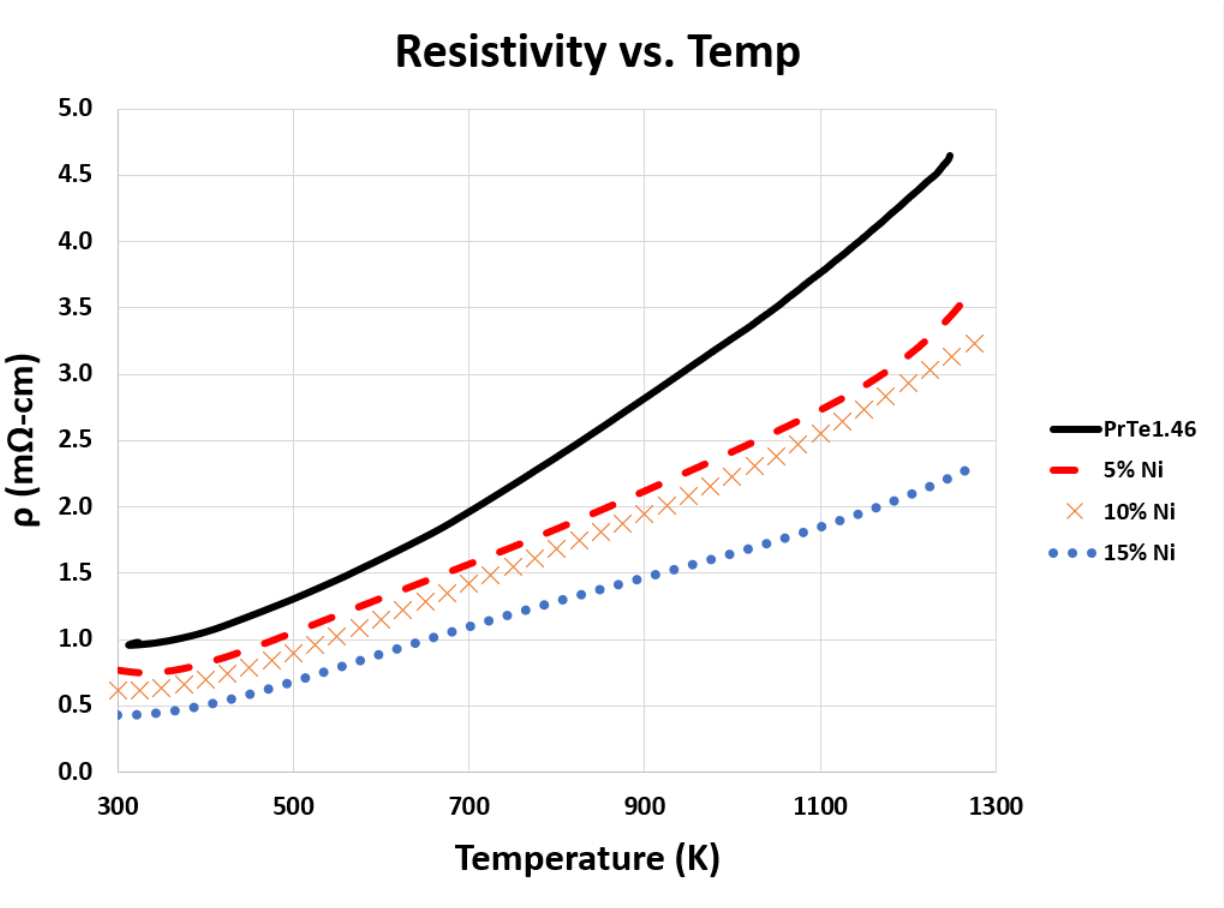

Figure 4.4. Temperature-dependent resistivity for $PrTe_{1.46}$-Ni composites made with the as-received 2.2-3 µm Ni powders

Figure 4.4 illustrates resistivity as a function of temperature for the $PrTe_{1.46}$-Ni composites. For the $PrTe_{1.46}$ parent batch as well as the $PrTe_{1.46}$-Ni composites, resistivity increases with temperature. This trend is expected based on a fundamental understanding of resistivity. Resistivity of metals and alloys is the sum of the contributions from thermal vibrations (ρ_t), impurities (ρ_i) and plastic deformation (ρ_d) - that is, scattering mechanisms that act independently of one another.

This is represented by the following equation (Matthiessen's rule):

$$\rho_{total} = \rho_t + \rho_i + \rho_d \quad \textbf{Equation 4.3}$$

For metals and alloys, the resistivity rises linearly with temperature. Thus,

$$\rho_{total} = \rho_0 + aT \quad \textbf{Equation 4.4}$$

where ρ_0 and a are constants for each particular metal, and T represents temperature. This dependence of the thermal resistivity component on temperature is due to the increase with temperature in thermal vibrations and other lattice irregularities (e.g.vacancies), which serve as electron scattering centers.[15]

We see a decrease in resistivity as we increase the volume percent of Ni present in the composite. All composites have resistivities lower than that of the baseline $PrTe_{1.46}$ sample. It is proposed that this ultimately verifies the CAFE effect, where the Ni inclusions are producing lower-resistance pathways in the matrix, ultimately reducing the electrical resistivity. As expected, increasing the Ni volume percentage, thus increasing the number of lower-resistance pathways, would continue to reduce electrical resistivity. This same effect is seen in $LaTe_{1.46}$-Ni composites; however, this effect did not take place until 12% Ni was incorporated into the composites (see Figure 4.2.). Thus, $PrTe_{1.46}$-Ni composites show a reduction in resistivity at smaller Ni volume percentages compared to $LaTe_{1.46}$-Ni.

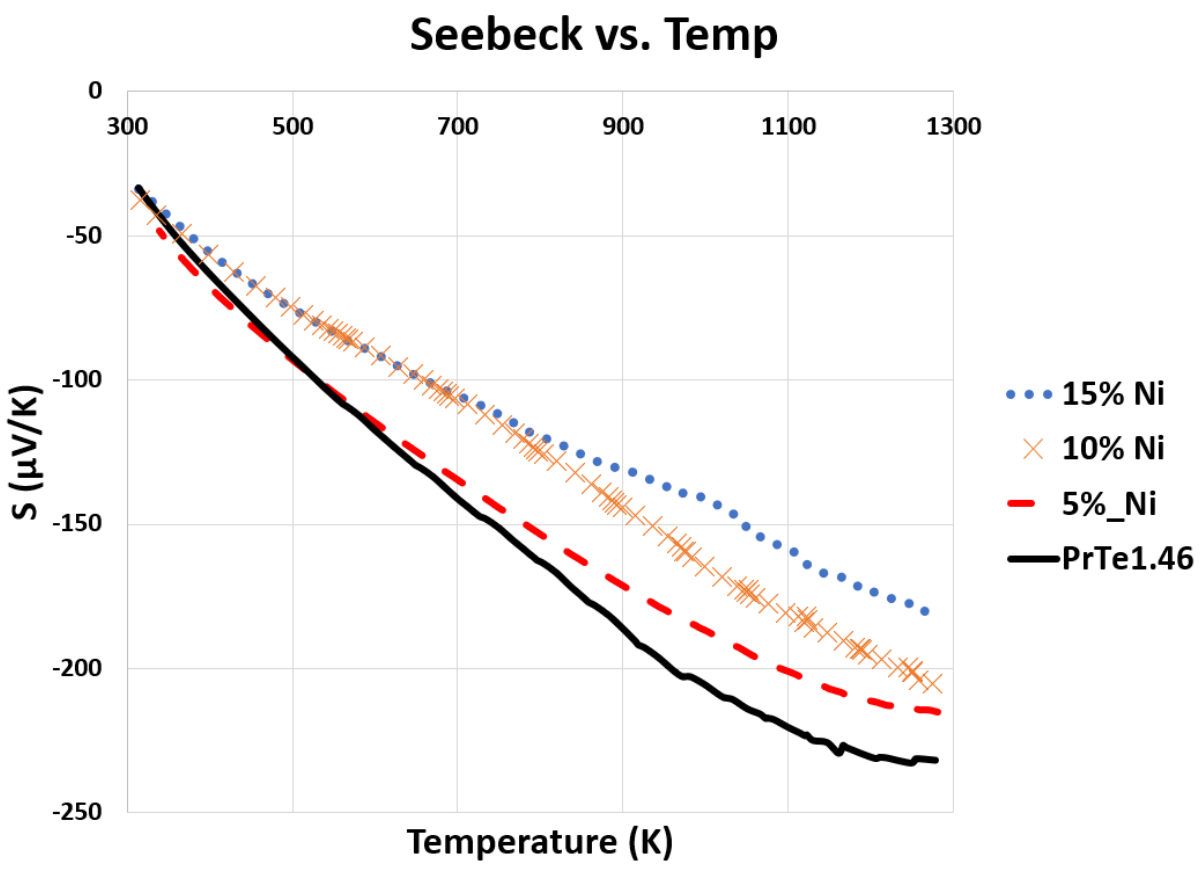

Figure 4.5. Temperature-dependent Seebeck coefficient for $PrTe_{1.46}$-Ni composites made with the as-received 2.2-3 μm Ni powders

Temperature-dependent Seebeck coefficients are shown in Figure 4.5. In this case, there is a continual decrease in Seebeck as more Ni is introduced into the composite.

As seen in Figure 4.2, the delayed onset of reduction in the Seebeck coefficient with respect to reduction in electrical resistivity for $LaTe_{1.46}$-Ni composites was attributed to large differences in the thermal conductivities between the inclusions and matrix. Since the thermal conductivity of Ni is significantly larger than that of the $LaTe_{1.46}$ matrix, the Ni particles act as thermal shunts resulting in smaller temperature differences across the inclusions.

Therefore, from an electrical standpoint, the Ni inclusions behave similar to voids which have been shown to have little impact on the Seebeck coefficient of bulk materials.[16] However, this does not seem to be a factor for $PrTe_{1.46}$-Ni composites, where there is no delayed reduction in Seebeck values. The underlying cause of this decrease at smaller Ni volume percentages is still under investigation; however, this trend corresponds to their respective decreases in resistivity. This likely indicates that the samples have become conductive enough that the resistivities and Seebeck coefficients are no longer decoupled, as was initially expected and hypothesized. Thus, $PrTe_{1.46}$-Ni composites show a reduction in Seebeck at smaller Ni volume percentages compared to $LaTe_{1.46}$-Ni.

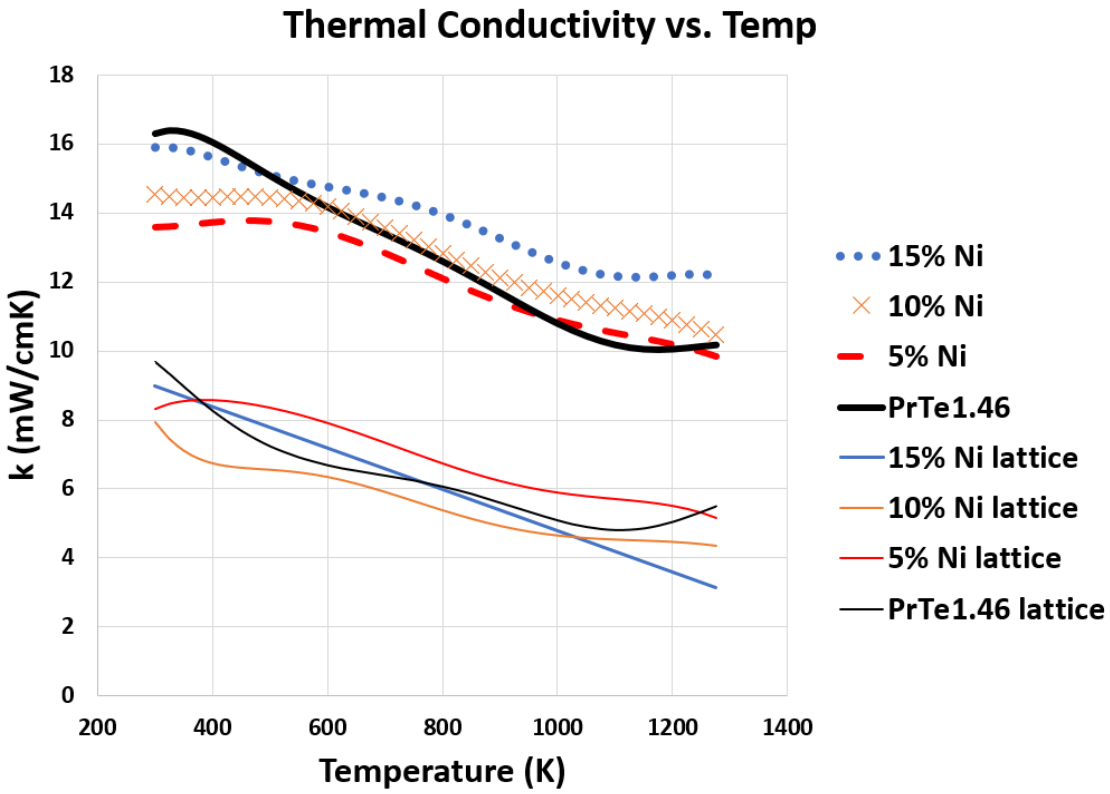

Figure 4.6. Temperature-dependent thermal conductivity for $PrTe_{1.46}$-Ni composites made with the as-received 2.2-3 µm Ni powders

The high-temperature heat capacity of the 2.2-3 μm composite which was previously measured was used in this research.[7] The thermal conductivities of the composites were calculated by combining the measured heat capacity with thermal diffusivity measurements. The solid lines indicate the lattice thermal conductivities calculated from the Wiedemann-Franz law using a temperature-dependent Lorenz number generated using a single parabolic band approximation.[17] The following equation illustrates the Wiedemann-Franz law:

where k represents thermal conductivity, σ is the electrical conductivity, T is the absolute

$$L = \frac{k}{\sigma T} \quad \textbf{Equation 4.5}$$

temperature, and L is the Lorenz number.

The total thermal conductivities of the composites increase slightly with an increase in Ni volume percentage compared to the baseline $PrTe_{1.46}$ sample. However, this increase is slight and could be attributed to the margin of error of the instrumentation. The lattice thermal conductivity results in a similar pattern, where all of the values are closely related and within the margin of error. This could also be attributed to an error in calculating a temperature-dependent Lorenz number using the single parabolic band model for a multiband system, since both $LaTe_{1.46}$ and $PrTe_{1.46}$ have multiple bands near the Fermi level.[18] The metallic character of the Ni reduces the Seebeck coefficient and increases the thermal conductivity following the progression toward more metallic behavior. This is a very similar trend to $LaTe_{1.42}$-Ni composites (Figure 4.2.); however,

because there is no significant decoupling that is occurring with $PrTe_{1.46}$, we see a slight decrease in Seebeck and slight increase in thermal conductivity at lower Ni volume percentages.

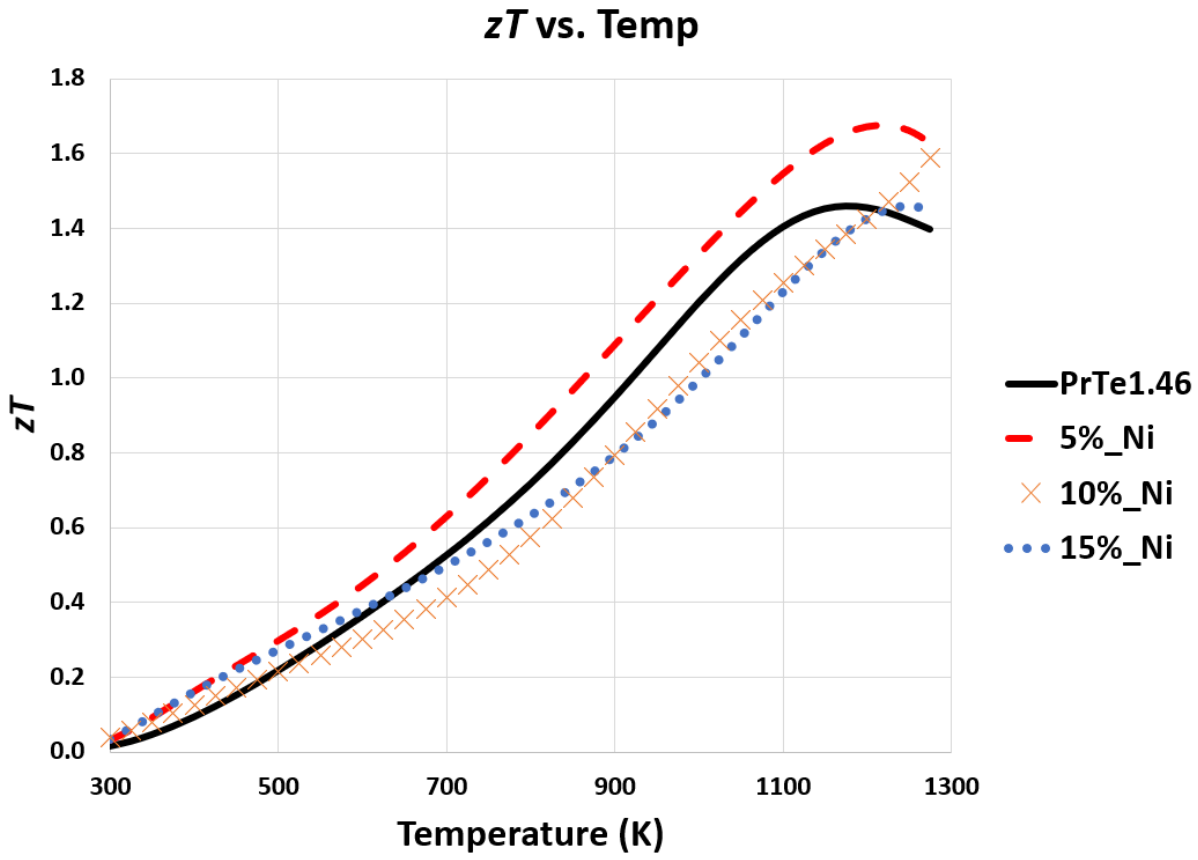

Figure 4.7. Thermoelectric figure of merit as a function of temperature for $PrTe_{1.46}$-Ni composites

The dimensionless figure of merit was calculated by combining all of the measured thermoelectric properties. Compared to the baseline $PrTe_{1.46}$, 5% volume $PrTe_{1.46}$-Ni composites resulted in an improvement in average *ZT* across all temperature ranges. Even though the average *ZT* slightly decreased for the 10% and 15% volume Ni composites, they still exceeded the peak *ZT* in the higher temperature range seen in the $PrTe_{1.46}$ baseline sample.

With the CAFE effect, as demonstrated in $LaTe_{1.46}$-Ni composites, increasing Ni volume percentage resulted in the following: a reduction in resistivity starting at 10% volume Ni as a result

of the formation of low-resistance pathways formed by the Ni inclusions; a decrease in Seebeck at 15% volume Ni due to Seebeck and resistivity decoupling; and an increase in total thermal conductivity starting at 5% volume Ni as a result of the progression toward metallic behavior.

However, in $PrTe_{1.46}$-Ni composites, the following trends were observed: there is a 21% reduction in resistivity at 5% volume Ni, resulting in a more significant decrease in resistivity compared to $LaTe_{1.46}$-Ni composites; Seebeck decreases starting at 5% volume Ni, suggesting that Seebeck and resistivity have not fully decoupled; and an increase in total thermal conductivity, although the total thermal conductivity is 50% lower compared to $LaTe_{1.46}$-Ni composites. While the reduction in resistivity would lead one to conclude that the CAFE effect has been demonstrated, the fact that the Seebeck and resistivity measurements have not decoupled would suggest that the CAFE effect is limited in this system, and other factors are more significantly contributing to the improvement in *ZT*.

Results for $LaTe_{1.46}$-Ni composites suggest that there is a minimum threshold for the amount of Ni required to decrease the resistivity of composites, implying that there is a proximity criterion between the Ni particles. Even though milling was employed to facilitate the distribution of Ni particles within the matrix, it is hypothesized that the proximity criterion for Ni particles was not reached for the $PrTe_{1.46}$-Ni composites, and thus the CAFE effect was not fully achieved.

4.4. Summary

$PrTe_{1.46}$-Ni composites were successfully synthesized and their thermoelectric properties were measured. As the volume fraction of Ni within the composite increased, there was an overall reduction in both resistivity and Seebeck while thermal conductivity was relatively unaffected. This resulted in *ZT* values for 5% volume Ni that increased the average *ZT*, while the 10% and 15% volume Ni resulted in an improvement in peak *ZT* at 1275K. While the exact

mechanism that leads to the improvement in *ZT* requires further investigation, it is proposed that the resultant increase cannot be attributed to the CAFE effect due to the Seebeck and resistivity coupling. This is still a significant finding, as the overall improvement in *ZT* attributed to $PrTe_{1.46}$ compared to $LaTe_{1.46}$ is slightly improved with $PrTe_{1.46}$-Ni composites.

4.5. References

[1] Rowe, David. "Introduction." *CRC Handbook of Thermoelectrics*, CRC Press, **1995**, http://dx.doi.org/10.1201/9781420049718.ch1

[2] Ma, Yi, et al. "Composite Thermoelectric Materials with Embedded Nanoparticles." *Journal of Materials Science*, 48, 7, 2012, 2767–78, https://doi.org/10.1007/s10853-012-6976-z

[3] Masood, Khalid Bin, et al. "Nanostructured Thermoelectric Materials." *Thermoelectricity and Advanced Thermoelectric Materials*, Elsevier, **2021**, 261–311, http://dx.doi.org/10.1016/b978-0-12-819984-8.00005-9

[4] Nan, Ce-Wen, and Quanxi Jia. "Obtaining Ultimate Functionalities in Nanocomposites: Design, Control, and Fabrication." *MRS Bulletin*, 40, 9, **2015**, 719–24, https://doi.org/10.1557/mrs.2015.196

[5] Vaqueiro, Paz, and Anthony V. Powell. "Recent Developments in Nanostructured Materials for High-Performance Thermoelectrics." *Journal of Materials Chemistry*, 20, 43, **2010**, 9577, https://doi.org/10.1039/c0jm01193b

[6] Sootsman, Joseph R., et al. "Strong Reduction of Thermal Conductivity in Nanostructured PbTe Prepared by Matrix Encapsulation." *Chemistry of Materials*, 18, 21, **2006**, 4993–95, https://doi.org/10.1021/cm0612090

[7] Cheikh, Dean. Synthesis and Characterization of Rare-Earth Tellurides and Their Composites For High-Temperature Thermoelectric Applications. UCLA, **2017**, 58–59, https://escholarship.org/uc/item/1ng766qh

[8] Al-Otaibi, Jawaher, and G. P. Srivastava. "Size and Dimensionality Dependent Phonon Conductivity in Nanocomposites." *Journal of Physics: Condensed Matter*, 28, 14, **2016**, 145304, https://doi.org/10.1088/0953-8984/28/14/145304

[9] Zhao, X. B., et al. "Bismuth Telluride Nanotubes and the Effects on the Thermoelectric Properties of Nanotube-Containing Nanocomposites." *Applied Physics Letters*, 86, 6, **2005**, https://doi.org/10.1063/1.1863440

[10] J. M. Ma, Improving the Mechanical Strength and Power Conversion Efficiency of High Temperature Thermoelectrics, Doctoral Dissertation, University of California, Los Angeles, **2014**

[11] Singh, Deobrat, and Rajeev Ahuja. "Dimensionality Effects in High-performance Thermoelectric Materials: Computational and Experimental Progress in Energy Harvesting Applications." *WIREs Computational Molecular Science*, 12, 1, **2021**, https://doi.org/10.1002/wcms.1547

[12] Thesberg, Mischa, et al. “On the Effectiveness of the Thermoelectric Energy Filtering Mechanism in Low-Dimensional Superlattices and Nano-Composites.” *Journal of Applied Physics*, 120, 23, **2016**, https://doi.org/10.1063/1.4972192

[13] Vineis, Christopher J., et al. “ChemInform Abstract: Nanostructured Thermoelectrics: Big Efficiency Gains from Small Features.” *ChemInform*, 41, 47,. **2010**, https://doi.org/10.1002/chin.201047216

[14] Dresselhaus, M. S., et al. “New Directions for Low-Dimensional Thermoelectric Materials.” *Advanced Materials*, 19, 8, **2007**, 1043–53, https://doi.org/10.1002/adma.200600527

[15] Minnich, A. J., et al. “Bulk Nanostructured Thermoelectric Materials: Current Research and Future Prospects.” *Energy & Environmental Science*, 2, 5, **2009**, 466, https://doi.org/10.1039/b822664b

[15] Callister Jr, William D. “Materials Science and Engineering - An Introduction (5th Ed.).” *Anti-Corrosion Methods and Materials*, 47, 1, **2000**, https://doi.org/10.1108/acmm.2000.12847aae.001

[16] Rowe, D M. “Electrical Properties of Hot-Pressed Germanium-Silicon-Boron Alloys.” *Journal of Physics D: Applied Physics*, 8, 9, **1975**, 1092–103, https://doi.org/10.1088/0022-3727/8/9/014

[17] Kim, Hyun-Sik, et al. “Characterization of Lorenz Number with Seebeck Coefficient Measurement.” *APL Materials*, 3, 4, **2015**, https://doi.org/10.1063/1.4908244

[18] May, Andre et al. “Influence of Band Structure on the Large Thermoelectric Performance of Lanthanum Telluride.” *Physical Review B*, 79, 15, 2009, https://doi.org/10.1103/physrevb.79.153101

Chapter 5: Conclusions and Future Work

5.1. Oxidation Study of RE_3Te_4 (RE = La, Pr, Nd)

The purpose of the first topic examined in this work was to better understand the oxidation kinetics and mechanisms of rare earth tellurides (primarily Pr_3Te_4 and Nd_3Te_4 as they compare to La_3Te_4). From a qualitative perspective, it has been noted that these materials are especially prone to oxidation; however, a quantitative analysis had not been explored in depth previously. Based on the differences across RE_3Te_4 in terms of electronic properties, it is hypothesized that there will be distinct differences for RE_3Te_4 in terms of oxidation mechanisms and kinetics as well, potentially as a result of differences in activation energy and formation rates of different rare earth oxides.

Results show that there is a distinctive difference in oxidation rates (and potentially mechanisms) for different rare earth tellurides (RE_3Te_4). Research indicates that rare earth tellurides experience similar oxidation mechanisms, but at distinct rates. Pr_3Te_4 and Nd_3Te_4 oxidize kinetically faster compared to La_3Te_4, which would suggest there is less time for the formation of intermediate phases. Future studies should explore high-temperature x-ray diffraction (HT XRD) measurements at fixed temperatures to understand the formation of intermediary phases and provide better insight into oxidation mechanisms.

5.2. $La(Pr)_{3-x}Te_4$ Alloys

The second topic examined in this work evaluated how alloying in the $La_{3-x}Pr_xTe_4$ system would tune the DOS via f-electrons, which will thus help reduce thermal conductivity because of point defect phonon scattering. Additionally, it was hypothesized that alloying would improve mechanical properties via solid solution strengthening; therefore, hardness of the $La_{3-x}Pr_xTe_4$

alloys would increase with an increase in concentration of Pr_xTe_4 that goes into the solid solution. Previous research has shown the crucial role of vacancies (x) on elastic and mechanical properties in $RE_{3-x}Te_4$, and highlights the unique, underappreciated, and poorly understood nature of mechanical properties in thermoelectric materials, which may vary considerably across a wide range of doping levels (see Appendix B).

As a direct result of this research, significant advancements in our comprehension of rare earth alloys and their effect on electronic and mechanical properties have been achieved through this research. It was hypothesized that alloying in the $La_{3-x}Pr_xTe_4$ system would tune the DOS via f-electrons, which will help reduce thermal conductivity because of point defect scattering. Indeed, there are significant differences in electronic properties across the alloys. Also, the rule of mixtures was scientifically proven due to the thermoelectric properties of the alloys residing between the properties of the end members. It was also hypothesized that alloying would improve mechanical properties via solid solution strengthening. Hardness measurements indicate that the end members and the alloys all have similar hardness values within error. Future studies will continue to expand on the impact of alloying on mechanical properties, and further computational analysis of the band structure tuning via *f*-electrons.

5.3. $PrTe_{1.46}$-Ni Composites

The final topic examined in this work was focused on discerning how the CAFE effect exhibits itself within a $PrTe_{1.46}$ matrix. It was hypothesized that a slight increase in the CAFE effect would take place, where there would be a slightly greater decrease in electrical resistivity compared to $LaTe_{1.46}$-Ni composites with no effect on Seebeck until higher volume percentages of Ni were achieved. Research indicates that the CAFE effect was not fully achieved in the

$PrTe_{1.46}$-Ni composites, since the resulting thermoelectric properties were dissimilar to the proven CAFE effect present in $LaTe_{1.46}$-Ni composites. For instance, at 5% vol Ni in $PrTe_{1.46}$, Seebeck immediately begins to decrease; this is unexpected, since Seebeck and resistivity are classically decoupled through the CAFE effect. However, the resultant 21% reduction in resistivity attributes to an improvement in average *ZT* for 5% volume Ni, while the 10% and 15% volume Ni resulted in an improvement in peak *ZT* at 1275K.

Further work should be conducted to better understand how the CAFE effect can be activated within $PrTe_{1.46}$-Ni composites, and what distinctions between $LaTe_{1.46}$-Ni and $PrTe_{1.46}$-Ni results in finite distinctions in thermoelectric property trends.

Appendix A Supporting Information for Chapter 3 (Electronic Properties For $Pr_{3-x}Te_4$)

Joule

CellPress

Article

Praseodymium Telluride: A High-Temperature, High-ZT Thermoelectric Material

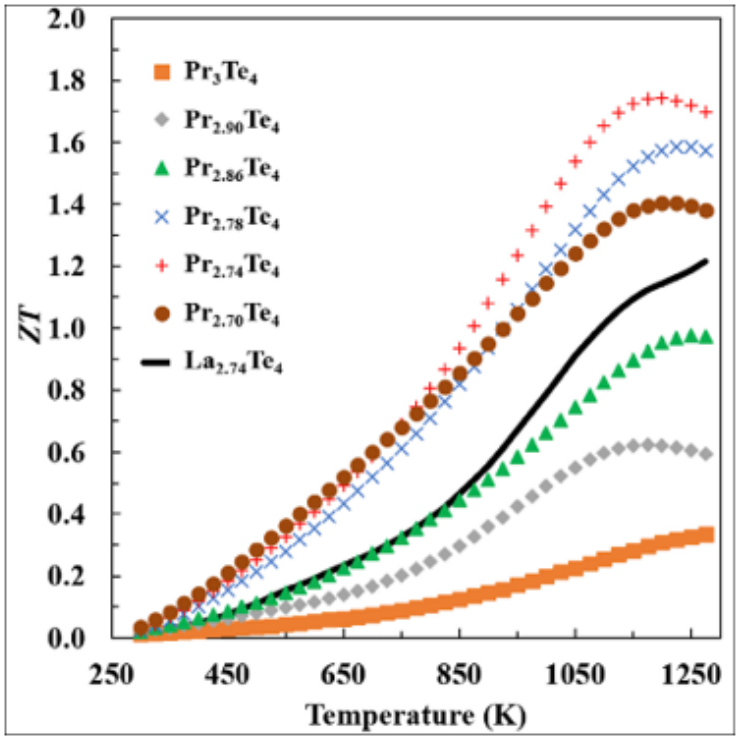

Praseodymium is known to have interesting optical and electronic properties but has been underutilized in the thermoelectric community. We synthesized a series of $Pr_{3-x}Te_4$ compounds and verified their phase purity and composition via Rietveld refinement of X-ray data, wavelength dispersive spectroscopy, and Hall carrier concentration with excellent agreement with the nominal stoichiometry. Measurement of transport properties indicate we were able to achieve a peak ZT = 1.7 at 1,200 K, the highest figure of merit reported above 1,000 K.

Dean Cheikh, Brea E. Hogan, Trinh Vo, ..., Bruce S. Dunn, Jean-Pierre Fleurial, Sabah K. Bux

sabah.k.bux@jpl.nasa.gov

HIGHLIGHTS

Praseodymium has been known to have interesting optical and electronic properties

Investigated the effects of *4f* electrons in Pr as a method of improving *ZT*

$Pr_{2.74}Te_4$ possesses a peak ZT = 1.7 at 1,200 K, the highest *ZT* reported above 1,000 K

Cheikh et al., Joule 2, 698-709
April 18, 2018 © 2018 Elsevier Inc.
https://doi.org/10.1016/j.joule.2018.01.013

Joule

CellPress

Article

Praseodymium Telluride: A High-Temperature, High-*ZT* Thermoelectric Material

Dean Cheikh,[1,2] Brea E. Hogan,[2] Trinh Vo,[2] Paul Von Allmen,[2] Kathleen Lee,[2] David M. Smiadak,[3] Alexandra Zevalkink,[3] Bruce S. Dunn,[1] Jean-Pierre Fleurial,[2] and Sabah K. Bux[2,4,*]

SUMMARY

Refractory rare-earth tellurides with the Th_3P_4 structure type have attracted considerable interest as high-performance thermoelectric materials since the 1980s due to their high dimensionless figure of merit (*ZT*). Extensive work has been conducted on $La_{3-x}Te_4$ with peak *ZT* values greater than 1.1 at 1,273 K. The high *ZT* of $La_{3-x}Te_4$ is in part due to a large peak in the density of states near the Fermi level from the La *5d* states. Here, we revisit $Pr_{3-x}Te_4$, for which our electronic structure calculations predict a favorable modification of the density of states by the introduction of praseodymium's *4f* electrons. This was experimentally verified by preparing $Pr_{3-x}Te_4$ samples with varying Pr vacancy concentrations using a mechanochemical synthesis approach. The thermoelectric properties were measured and a *ZT* of 1.7 at 1,200 K was achieved with $Pr_{2.74}Te_4$. The 50% improvement in peak *ZT* compared with $La_{3-x}Te_4$ resulted from an increased effective mass, improved Seebeck coefficient, and lower thermal conductivity.

INTRODUCTION

Thermoelectric materials have been integrated into solid-state energy conversion devices, which can either function as electrical power generators or be utilized as heat pumps for electronic refrigeration. Si-Ge alloys, PbTe, and Te-Ag-Ge-Sb (TAGS) have been successfully integrated into radioisotope thermoelectric generators (RTGs) to enable deep space and planetary scientific exploration of our solar system for more than 50 years. RTGs have demonstrated long-term reliability and longevity, as evidenced by the *Voyager 1* and *Voyager 2* missions operating continuously for over 40 years.[1]

While systems built using heritage thermoelectric materials have demonstrated high reliability, one limiting factor is the fact that they exhibit modest thermal-to-electric energy conversion efficiency (approximately 6.5% at the system's beginning-of-life, BOL). This is because their average dimensionless figure of merit (*ZT*) values over their operating temperature range are significantly lower than 1 (about 0.80 for PbTe/TAGS materials across a 811–483 K temperature range and 0.55 for Si-Ge alloys over a 1,273–573 K temperature range).[2–5] The dimensionless thermoelectric figure of merit is defined as $ZT = \frac{S^2 T}{\rho \kappa}$, where *S* is the Seebeck coefficient, *T* is temperature, r is electrical resistivity, and k is thermal conductivity. Therefore, identifying materials that possess a high Seebeck coefficient, low resistivity, and low thermal conductivity would allow for larger scientific payloads, decrease the amount of radioisotope heat-source fuel used, and reduce the weight of the RTG for a given power level.[6]

Context & Scale

Thermoelectric generators have been an enabling technology for reliably powering many long-lived space science and exploration missions by the National Aeronautics and Space Administration such as the *Voyager* missions and the recent Mars rover, *Curiosity*. A significant increase in conversion efficiency by materials such as $Pr_{3-x}Te_4$ would translate into a reduction in the amount of expensive heat-source fuel and could allow for an increase in the available power as well as more capable payloads for a given mission. Beyond space applications, higher efficiencies would benefit the recent surge of interest in implementing thermoelectrics for terrestrial applications such as waste heat recovery from automobiles and industrial processes.

Lanthanum telluride ($La_{3-x}Te_4$) has been identified as a potential material for high-temperature thermoelectric applications.[3] $La_{3-x}Te_4$ possesses the defect thorium phosphide (Th_3P_4) structure type, with 28 atoms per unit cell, which accommodates vacancies on up to one-ninth of the rare-earth sites. Each La atom donates three electrons and each tellurium atom accepts two electrons, resulting in one free electron per La_3Te_4 formula unit. Therefore, the carrier concentration is tied to the number of La vacancies and the electronic properties can be tuned between metallic behavior when $x = 0$ (La_3Te_4) and semi-insulating when $x = 0.33$ ($La_{2.67}Te_4$). Additionally, $La_{3-x}Te_4$ exhibits a relatively low lattice thermal conductivity resulting from the complexity of the Th_3P_4 structure type, electron-phonon scattering from the high carrier concentration, and phonon scattering from vacancies. As a result, $La_{3-x}Te_4$ has a high peak ZT of 1.1 at 1,273 K for $x = 0.23$.[7]

Other rare-earth tellurides possessing the Th_3P_4 structure type have also been studied for potential use as thermoelectric materials.[4,8–14] This is due to their stability in the high-temperature range of interest for RTGs and the large ZT values exhibited by some of the compounds.[4,15] However, reproducibility of the thermoelectric properties of specific stoichiometry of these compounds has proved challenging. Melt synthesis or solid-state reactions of the elemental species were used extensively in reports examining the rare-earth tellurides.[16–18] These techniques often require high temperatures (>2,000 K) and typically result in inhomogeneous samples. The large difference in melting points between tellurium (722 K) and the rare-earth elements (1,193 K for lanthanum and 1,208 K for praseodymium) leads to vapor-phase loss of tellurium and alters the final stoichiometry of the products, which are very sensitive to stoichiometric deviations due to vacancy doping. Additionally, the oxygen sensitivity of the rare-earth elements and tellurides is problematic, especially at elevated temperatures. Recently it has been demonstrated that mechanochemical synthesis can be used to synthesize $La_{3-x}Te_4$ at low temperatures.[7] The use of mechanochemical synthesis circumvents the challenges associated with high-temperature synthetic techniques by mechanochemically synthesizing $La_{3-x}Te_4$ product in a closed system (ball mill vial) operating at room temperature, thereby allowing samples to be prepared reproducibly with precise stoichiometry and in a short period of time.

The band structure of $La_{3-x}Te_4$ has been shown to be favorable for a large Seebeck coefficient due to heavy conduction bands.[19] The electronic density of states (DOS) in the conduction band of $La_{3-x}Te_4$ is composed almost entirely of La states, while the Te states dominate the valence band.[19,20] A large Seebeck coefficient can be achieved at high carrier concentrations due to a sharp peak in the DOS near the Fermi level in the conduction band. Modifications of the DOS to further improve the Seebeck coefficient have been attempted using divalent substitutions of Ca and Yb on the La site, but were found to have little impact on the thermoelectric properties.[21,22] Examination of the DOS of $La_{3-x}Te_4$ reveals that while the main contribution to the peak in the conduction band comes from the La *5d* orbital, there is also contribution from the *4f* states. The smaller contribution of the *4f* orbitals results from the absence of *f* electrons in La *4f* shell. However, since the *4f* states are located above the Fermi level, an increase in the DOS or sharpening of the peak at the Fermi level by introduction of *4f* electrons could increase the Seebeck coefficient and ultimately the thermoelectric performance of the material.

Previously we have studied the effects of $Ce_{3-x}Te_4$, where Ce possesses 1 electron in the valence shell. We found that the thermoelectric properties of $Ce_{3-x}Te_4$ were similar to that of $La_{3-x}Te_4$[20] (also J.P. Fleurial, personal communication). To investigate the effects of the *4f* electrons on the DOS, we studied $Pr_{3-x}Te_4$, where the Pr

[1]Department of Materials Science and Engineering, University of California, Los Angeles, Los Angeles, CA 90095, USA

[2]Thermal Energy Conversion Research and Advancement Group, Jet Propulsion Laboratory/California Institute of Technology, 4800 Oak Grove Drive, Pasadena, CA 91109, USA

[3]Department of Materials Science and Engineering, Michigan State University, East Lansing, MI 48824, USA

[4]Lead Contact

*Correspondence: sabah.k.bux@jpl.nasa.gov

https://doi.org/10.1016/j.joule.2018.01.013

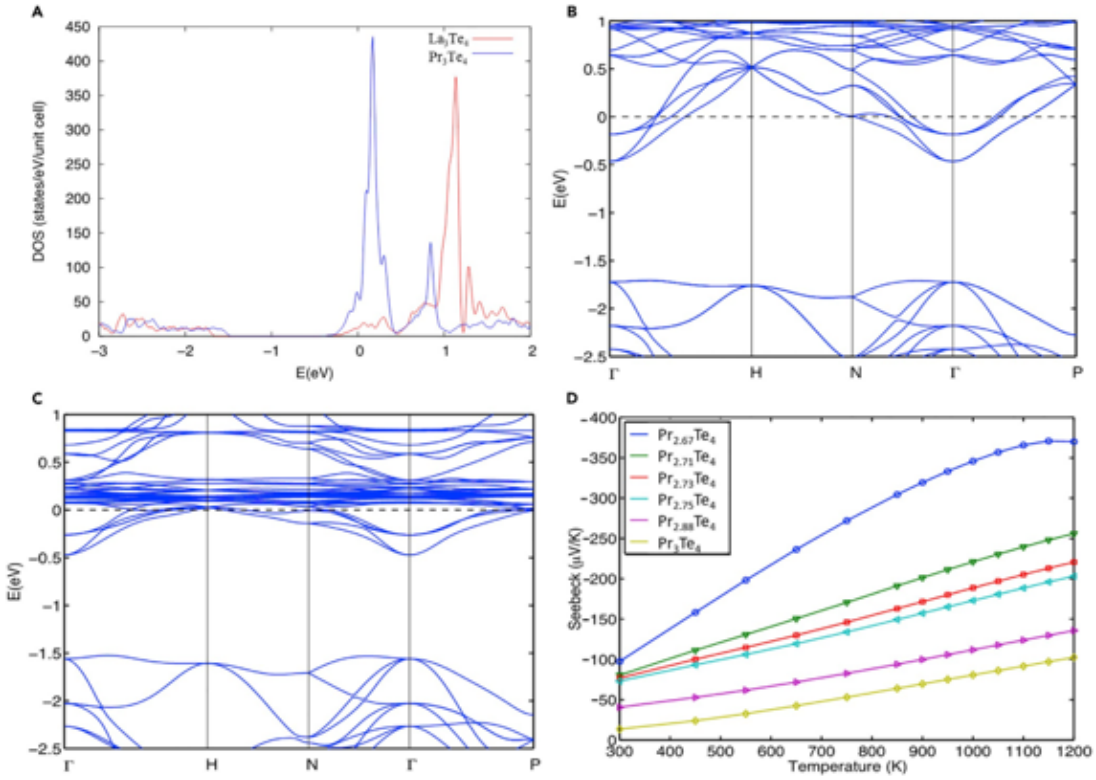

Figure 1. Calculated Electronic Band Structure of Pr_3Te_4 and La_3Te_4

(A) Comparison of density of states (DOS) of La_3Te_4 and Pr_3Te_4. The Fermi level is defined as $E_f = 0$ for both compounds.

(B) Calculated electronic band structure diagram of La_3Te_4.

(C) Calculated electronic band structure diagram of Pr_3Te_4.

(D) Seebeck coefficient of Pr_3Te_4 as a function of temperature and rare-earth vacancy concentration.

atoms include three *4f* valence electrons in the valence shell. This addition of *f* electrons has given Pr-containing compounds novel optical, magnetic, and superconducting properties.[25–25] While the electronic properties of $Pr_{3-x}Te_4$ have been previously reported, the use of melt synthesis led to inconsistencies in reported values.[4,26,27] To avoid these issues, we employed mechanochemical synthesis to produce $Pr_{3-x}Te_4$ samples with increasing vacancy concentrations and measured the thermoelectric properties.

RESULTS AND DISCUSSION

Pr_3Te_4 Electronic Structure

Band engineering is one of the key tools for optimizing *ZT* of complex materials. An important difference between Pr_3Te_4 and La_3Te_4 is the presence of three additional *f* electrons in Pr. We have studied the band structures and DOS of these two materials to understand the extent to which the *f* states affect the thermoelectric properties. Figure 1A compares the DOS of La_3Te_4 and Pr_3Te_4. The sharp peaks observed in the DOS of both compounds are mainly associated with the *f* orbitals (see discussion in the next paragraph). While the *f* peak in La_3Te_4 is located far above the Fermi level, the *f* peak in Pr_3Te_4

is situated near and at the Fermi level, resulting in a higher DOS in the energy range of interest to n-type thermoelectric materials. This enhancement in DOS at the Fermi level is one of the important requirements for improving transport properties. To have an enhanced transport property, the Fermi energy for the experimental value of the electron density should be close enough to the resonance in the DOS such that band contributions to *ZT* become dominant. An example of this observation can be found for the case of Ce_3Te_4, where the *f* peak is too far from the Fermi level to significantly contribute to the Seebeck coefficient at practical experimental conditions.[20]

The role of *f* electrons on the electronic properties can be further investigated by comparing partial DOS of La_3Te_4 and Pr_3Te_4. As seen from Figures S1 and S2, the main contribution to the DOS peak in the La_3Te_4 and Pr_3Te_4 comes from *5d* and *4f* orbitals of La and Pr, respectively. However, because the La *4f* peak in La_3Te_4 is located far from the Fermi level, significant contribution to the DOS and, thus, transport property at and near the Fermi level relies mostly on La *5d* orbitals for La_3Te_4. On the other hand, although the two peaks (the large and small ones) observed in Pr_3Te_4 DOS are also mainly contributed by the *f* orbitals and *d* orbitals, the contribution from the *f* orbitals dominates at the Fermi level. Consequently, for Pr_3Te_4 it is expected that the presence of three *f* electrons in Pr atoms would enhance the transport properties, compared with La atoms with no electrons in the *f* shells. In addition, Figures S1 and S2 also show a gap that separates the *f* peak from other lower energy states (with energy of less than ~1.4 eV) in both cases. The gap is ~0.91eV for Pr_3Te_4, which is smaller than that of La_3Te_4 (~1.01 eV). While the main contribution to the DOS peak is the *4f* orbitals, far below the Fermi level in the valence band at the energy of ~1.4 eV, Te *5p* orbitals are found to contribute the most to the DOS.

To acquire further insight into the difference in electronic properties of La_3Te_4 and Pr_3Te_4, we examined the band structures of both compounds. Figures 1B and 1C show the band structures of La_3Te_4 and Pr_3Te_4. Slightly above the Fermi level in the band structure of Pr_3Te_4 a denser region of flat bands is observed, which originates from the *4f* orbitals of Pr atoms. Further above the Fermi level (~0.5 eV), significant changes in the band structure are also observed for the case of Pr_3Te_4, especially at the H, N, and G points. The bands become flatter, and band degeneracy is changed dramatically. Due to the effect of *f* orbitals, the bands at the G point have smaller curvatures for the Pr_3Te_4 case than for La_3Te_4. Consequently, the effective masses are expected to be larger for Pr_3Te_4 than for La_3Te_4.

The Seebeck coefficients for Pr_3Te_4 and La_3Te_4 are computed using standard expressions derived from the linearized Boltzmann Transport Equation and the rigid band approximation to describe the variation of electron concentration due to vacancies.[19,28,29] In the rigidband approximation, the band structure of the studied compounds is assumed to be unchanged when varying the electron concentration; only the position of the Fermi energy is adjusted. Figure 1D presents the Seebeck coefficients of Pr_3Te_4 as a function of temperature and carrier concentration. Here the Seebeck coefficient increases with increasing temperature, and decreases with increasing carrier concentration. Figure S3 compares the Seebeck coefficient of both compounds. The plot shows larger Seebeck coefficients for Pr_3Te_4 than for La_3Te_4 for all carrier concentrations of interest (10^{20}–10^{22} cm^{-3}). The results are consistent with the increase in DOS due to the presence of *f* electrons observed near and at Fermi energy.

Sample Characterization

Densified, sintered compacts were ground using a mortar and pestle and their phase purities analyzed using powder X-ray diffraction (XRD). The diffraction pattern shown

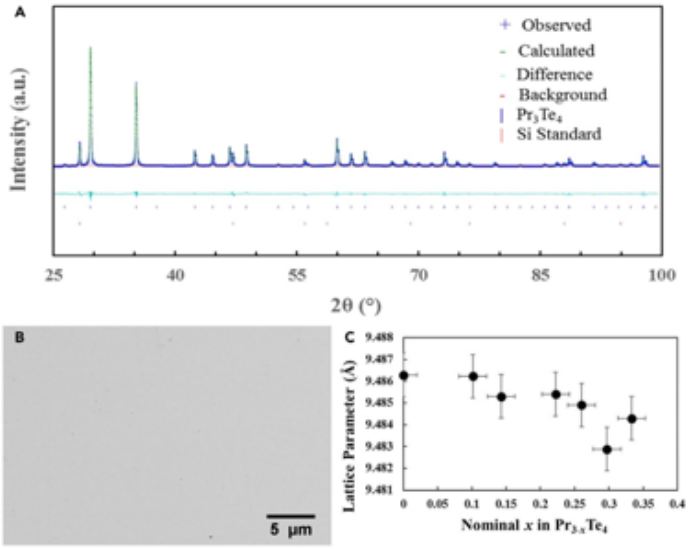

Figure 2. Phase and Compositional Analysis of $Pr_{3-x}Te_4$ Samples

(A) X-ray diffraction pattern of $Pr_{2.74}Te_4$ mixed with a Si internal standard. The pattern is representative of the diffraction patterns of other $Pr_{3-x}Te_4$ samples in this study, with no secondary or oxide phases present. Rietveld refinement was performed and the calculated pattern and difference curve are shown. The fit from the Rietveld analysis is in agreement with the Pr_3Te_4 phase. The goodness of fit was found to be 2.39 and wR = 0.770%.

(B) BSE micrograph of the polished surface of the $Pr_{2.74}Te_4$ sample. The uniformity of the image contrast reflects the homogeneity of the samples. Dark regions in the image are from the small amount of residual porosity present in the sample.

(C) Lattice parameter calculated from Rietveld analysis as a function of vacancy concentration. Error bars in lattice parameters represent the diffractometer limit of G0.001 Å and error bars in x represent 5%.

in Figure 2A is of a representative sample. No secondary or oxide phases were detected, and the pattern correlated with the Pr_3Te_4 pattern previously reported.[28] Phase homogeneity of the samples further verified by the backscattered electrons (BSE) on samples consolidated by spark plasma sintering (SPS) as shown in Figure 2B is typical of all samples, and the uniform contrast reflects the phase homogeneity of the sample. The dark areas in Figure 2B resulted from trace amounts of residual porosity in the sample. From Figure 2B, the porosity was calculated to be approximately 2.5%.

To determine the composition of each sample, we employed both wavelength dispersive X-ray spectroscopy (WDS) (on sintered samples) and Rietveld analysis (on ground compacts). These values were compared with nominal compositions in Table 1. Ten WDS measurements were averaged for each value given. WDS and nominal compositions were in good agreement for all compositions, as were the values calculated from Rietveld for samples near the compositions Pr_3Te_4 and $Pr_{2.67}Te_4$. The Rietveld calculations were found to underestimate the vacancy concentrations for intermediate compositions due to the XRD scan quality not having the necessary resolution for consistent calculation of the fractional occupancy, although the values are in good agreement with the nominal compositions. The lattice parameter for each sample was also determined from Rietveld analysis, as shown in Figure 2C. There was little change in the lattice parameter when the maximum number of vacancies was introduced, which

Table 1. Nominal Sample Composition Compared with Compositions Measured from WDS and Rietveld Analysis

Nominal Composition	WDS Composition	Rietveld Composition
Pr_3Te_4	$Pr_{3.00}Te_4$	$Pr_{3.00}Te_4$
$Pr_{2.95}Te_4$	$Pr_{2.93}Te_4$	$Pr_{2.92}Te_4$
$Pr_{2.85}Te_4$	$Pr_{2.89}Te_4$	$Pr_{2.91}Te_4$
$Pr_{2.78}Te_4$	$Pr_{2.79}Te_4$	$Pr_{2.86}Te_4$
$Pr_{2.74}Te_4$	$Pr_{2.79}Te_4$	$Pr_{2.79}Te_4$
$Pr_{2.70}Te_4$	$Pr_{2.79}Te_4$	$Pr_{2.68}Te_4$
$Pr_{2.67}Te_4$	$Pr_{2.8}Te_4$	$Pr_{2.67}Te_4$

The nominal and WDS compositions were in good agreement with one another. Compositions calculated via Rietveld analysis were in good agreement with nominal and WDS compositions for samples near Pr_3Te_4 and $Pr_{2.667}Te_4$, but samples with intermediate compositions were found to underestimate the vacancy concentrations.

is consistent with prior structural investigations of $Pr_{3-x}Te_4$.[28,29] The small change in lattice parameter is also observed in $La_{3-x}Te_4$; however, the mass density of $La_{3-x}Te_4$ is constant at 6.58 g cm^{-3} whereas that of $Pr_{3-x}Te_4$ is 7.27 g cm^{-3} when x = 0 and 6.91 g cm^{-3} when x = 0.33.[19,30–32] The difference in the density behavior as a function or rare-earth atomic vacancies for these two materials is not well understood and warrants further investigation.

Electronic Transport Properties

Electrical resistivity as a function of temperature was measured, and is shown in Figure 3A along with values previously reported for $La_{3-x}Te_4$.[19] All samples exhibited behavior expected for a degenerately doped semiconductor. The resistivity of the samples increased with increasing vacancy concentration due to the reduction in carrier concentration. Measurements made on samples with x = 0.33 were conducted but the high resistivity of the samples presented difficulties in making ohmic contacts, which resulted in inaccurate Van der Pauw resistivity values. The resistivity of $Pr_{3-x}Te_4$ samples trends well with the values of $La_{3-x}Te_4$ for lower vacancy concentrations. However, at higher vacancy concentrations the $Pr_{3-x}Te_4$ samples exhibited higher resistivity values than $La_{3-x}Te_4$ with equivalent vacancy concentrations.

The temperature-dependent Seebeck coefficient is shown in Figure 3B. The Seebeck coefficient increased with increasing vacancy due to the reduction in carrier concentration, as expected. Similar to what was observed with the high-temperature resistivity, the $Pr_{3-x}Te_4$ samples with lower vacancy concentrations were found to be similar to those of $La_{3-x}Te_4$, and at higher vacancy concentrations the $Pr_{3-x}Te_4$ samples yielded higher Seebeck coefficients compared with $La_{3-x}Te_4$. Specifically, the $Pr_{2.74}Te_4$ composition exhibited a 25% increase in the Seebeck coefficient when compared with $La_{2.74}Te_4$. The improved Seebeck coefficient of $Pr_{2.74}Te_4$ resulted in an increased power factor (sS^2) over $La_{2.74}Te_4$ (Figure 3C).

An effective mass of m^* = 3.5m_e and 2.13m_e were calculated for $Pr_{2.74}Te_4$ and $La_{2.74}Te_4$, respectively, using a single parabolic band model (Figure S8). An effective mass of 2.13m_e matches well with previously reported values for $La_{3-x}Te_4$, which range from 1.6m_e to 2.75m_e.[4,7,9] The increased effective mass of $Pr_{2.74}Te_4$ over $La_{2.74}Te_4$ is consistent with the observed increase in the Seebeck coefficient at equivalent vacancy concentrations, and supports the hypothesis that the *4f* electrons modified the band structure favorably over $La_{3-x}Te_4$.

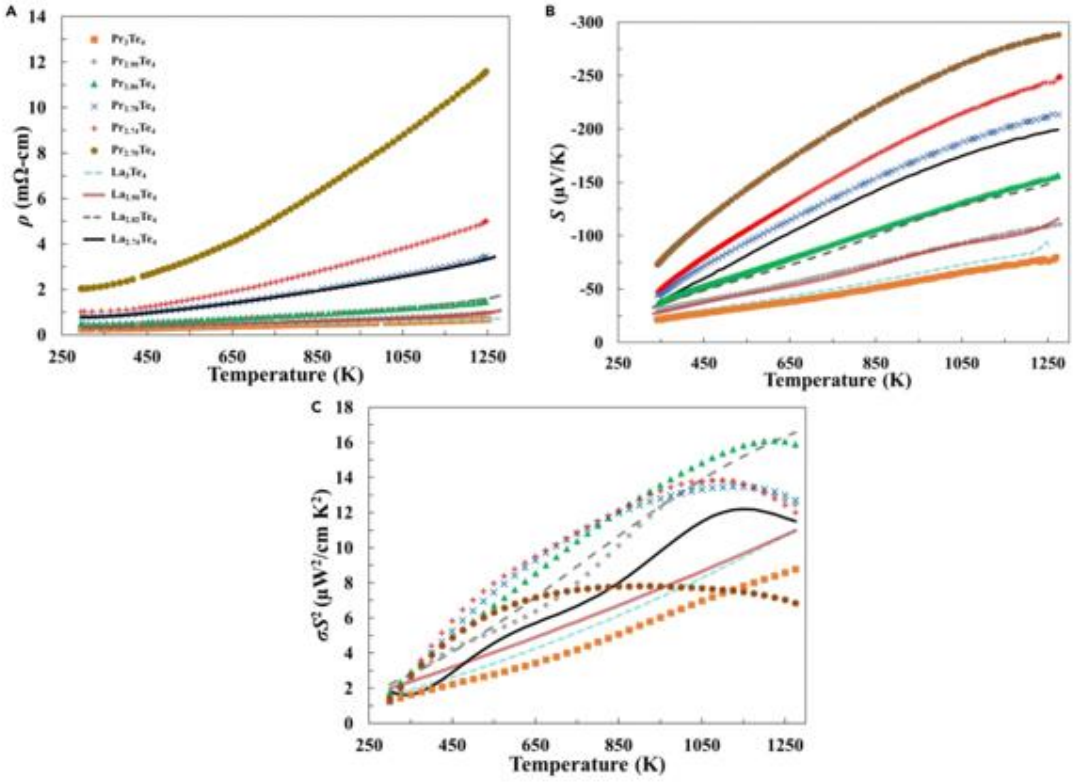

Figure 3. High-Temperature Electronic Properties of $Pr_{3-x}Te_4$ Samples

(A) Temperature-dependent resistivity of $Pr_{3-x}Te_4$ samples compared with that of $La_{3-x}Te_4$.[7] The samples are indicated by their nominal compositions. The higher vacancy concentration $Pr_{3-x}Te_4$ samples had resistivities much higher than equivalently vacancy doped $La_{3-x}Te_4$.

(B) Seebeck coefficient as a function of temperature of $Pr_{3-x}Te_4$ samples compared with that of $La_{3-x}Te_4$.[7] $Pr_{3-x}Te_4$ samples at higher vacancy concentrations exhibited significantly larger Seebeck values compared with $La_{3-x}Te_4$.

(C) Temperature-dependent power factor (αS^2) of $Pr_{3-x}Te_4$ and $La_{3-x}Te_4$ samples. An increase was observed for $Pr_{2.74}Te_4$ over $La_{2.74}Te_4$ across the temperature range measured.

Thermal Transport Properties

The total thermal conductivity is shown in Figure 4A and was calculated from $k = DC_pd$, where D is the measured thermal diffusivity, C_p is the measured heat capacity (Figure S9), and d is the sample density (Table S2). Thermal conductivities were found to range from 5 to 35 mW cm^{-1} K^{-1}, with the thermal conductivity decreasing with increasing vacancy concentration. This was expected, as the total thermal conductivity is composed of two components, the electronic and lattice thermal conductivities, and is given by $k = k_e + k_l$. Therefore the increased vacancy concentration had a reduced electronic term from the corresponding decreased carrier concentration. This behavior is similar to that previously reported for $La_{3-x}Te_4$.

When samples with equivalent vacancy concentrations were compared, it was found that $Pr_{3-x}Te_4$ samples exhibited a significantly lower thermal conductivity than $La_{3-x}Te_4$. To determine whether this decrease was due to a change in the electronic or lattice contributions, we calculated the lattice thermal contribution. The lattice

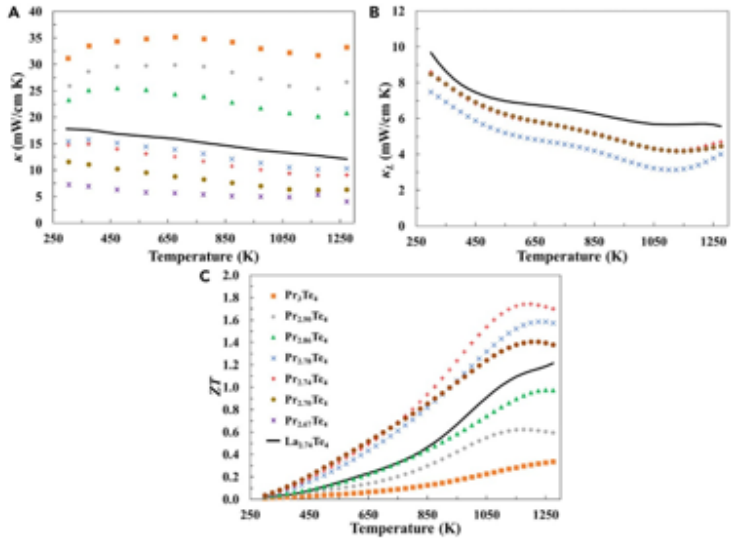

Figure 4. Temperature-Dependent Thermal Conductivity and Dimensionless Figure of Merit of $Pr_{3-x}Te_4$

(A) Total thermal conductivities of $Pr_{3-x}Te_4$ compared with $La_{2.74}Te_4$.[7]

(B) Lattice thermal conductivities calculated using the Wiedemann-Franz law. $Pr_{3-x}Te_4$ samples with higher carrier concentrations were omitted due to strong deviation from the Wiedemann-Franz law.

(C) Temperature-dependent thermoelectric figure of merit, *ZT*, as a function of temperature. The optimized *ZT* for $La_{3-x}Te_4$ is shown for comparison. The error in *ZT* is approximately 30%.[7]

thermal conductivity was found by first calculating the electronic contribution using the Wiedemann-Franz law $\kappa_e = LsT$, where *L* is the Lorenz number and s is the electrical conductivity; the electronic contribution was then subtracted from the total thermal conductivity. A simplified variable Lorenz number was used, which was calculated as a function of Seebeck coefficient using the approximation $L = 1.5 + \exp(-|S|/116)$ and resulted in Lorenz numbers between 1.5 and 2.2 3 10^{21} WU K^{-2}.[33]

Figure 4B shows the calculated lattice contributions to the total thermal conductivity, κ_L, for vacancy concentrations similar to $La_{2.74}Te_4$. The intrinsically low κ_L resulted from the complexity of the Th_3P_4, which promoted substantial Umklapp scattering of acoustic phonons.[22] κ_L values for the $Pr_{3-x}Te_4$ samples were found to be similar to one another and lower than that calculated for $La_{2.74}Te_4$ from room temperature to 1,275 K. To investigate the origin of the reduced κ_L in $Pr_{3-x}Te_4$, we measured the elastic moduli and sound velocities of both $La_{2.74}Te_4$ and $Pr_{2.74}Te_4$ from room temperature up to 573 K. The elastic moduli $Pr_{2.74}Te_4$ was found to be slightly lower than $La_{2.74}Te_4$. Combined with the higher density of $Pr_{2.74}Te_4$, this led to a small decrease in the speed of sound (Figure S4), which is consistent with the lower κ_L.

Thermoelectric Figure of Merit

Combining the electronic and thermal transport properties, the *ZT* was calculated as a function of temperature (Figure 4C), with a propagated error of 30%. *ZT* was found to increase with increasing vacancy concentration until $x = 0.26$ and then began to decrease. A peak *ZT* of 1.7 at 1,200 K was achieved. This represents a 50%

improvement over the optimized *ZT* of 1.1 reported for $La_{3-x}Te_4$.[7] The improvement in *ZT* resulted from the large increase in the Seebeck coefficient from the electronic states introduced by the 4*f* electron in addition to the lower thermal conductivity, which resulted from a decreased lattice contribution.

Conclusion

Density functional theory was used to calculate the DOS and energy band diagram for Pr_3Te_4. It was found that the 4*f* electrons of Pr cause a sharp increase in the DOS near the conduction band edge when compared with $La_{3-x}Te_4$. The increase in the DOS was predicted to improve the Seebeck coefficient of *n*-type $Pr_{3-x}Te_4$. A series of $Pr_{3-x}Te_4$ samples with varying vacancy concentrations were successfully synthesized using mechanochemical methods. The stoichiometry and phase purity were analyzed through a combination of WDS and XRD. The electronic and thermal properties were measured and $Pr_{3-x}Te_4$ exhibited a 25% improvement in the Seebeck coefficient over $La_{3-x}Te_4$ near optimal vacancy concentration levels. Additionally, $Pr_{3-x}Te_4$ was found to have decreased thermal conductivity due to a smaller lattice contribution than $La_{3-x}Te_4$. The increased Seebeck coefficient and reduced thermal conductivity resulted in a peak *ZT* of 1.7 at 1,200 K. The successful theoretical prediction and experimental verification of the modified band structure of $Pr_{3-x}Te_4$ due to the 4*f* electrons suggests that further improvements can be made by incorporating other rare-earth elements.

EXPERIMENTAL PROCEDURES

Synthesis

A mechanochemical approach was used to synthesize samples of the desired stoichiometry. Elemental Pr (99.9%, Stanford Materials) and Te shot (99.999, 5N Plus) were combined and sealed under argon in stainless-steel ball mill vials with stainless-steel balls. They were then milled (SPEX SamplePrep 8000) for over 10 hr until homogeneous black powders of $Pr_{3-x}Te_4$ were produced. The powders were then densified in graphite dies through SPS at a pressure of 80 MPa and at temperatures above 1,200°C for 30 min under vacuum. The Archimedes method was used to measure density, and the compacted samples were found to be 97% dense or greater of theoretical values (Table S2).

Characterization

XRD data were collected with a Phillips PANalytical X'Pert Pro diffractometer using Cu Ka radiation. Compacted samples were ground using a mortar and pestle and then mixed with Si powder (−325 mesh, 99.999%, Alfa Aesar) to use as an internal standard during Rietveld analysis. Due to the $Pr_{3-x}Te_4$ powders being highly air sensitive, the powders were sealed with 1-mm thick Kapton film on an Si zero background holder under argon. Scans were performed over a 2q range of 25°–100°, with a 0.02° step size and a time of 11.5 s per step. Rietveld refinement was done using GSAS-II crystallographic data analysis software.[34] Structural data for the cubic phase with space group $I\bar{4}3d$ from Mitarov et al. was used for refinement.[30] To perform a stable refinement of the Pr occupancy, the occupancy on the Te position was held at 100% as no vacancies were expected.

WDS was performed to assess the elemental compositions of the sintered compacts. A JEOL JXA-8200 electron probe microanalyzer was utilized, with $PrPO_4$ and elemental Te as the standards. Ten points were measured for each sample and the elemental compositions were averaged to determine the composition of the samples. Backscattered electron scanning electron microscopy images were taken on a Zeiss 1550 VP scanning electron microscope.

A custom-built combined 4-point probe and Hall effect system was used to measure the electrical resistivity and Hall voltage, from which the carrier concentration and mobility were calculated.[35] The Seebeck coefficient was measured using a custom-fabricated instrument.[36] Thermal diffusivity was measured using a commercial Netzsch LFA 457 system and specific heat capacity was measured using a Netzsch DSC 404. The thermal conductivity was calculated by $k = DC_p d$, where k is the thermal conductivity, D is the thermal diffusivity, C_p is the specific heat capacity, and d is the sample density. Errors in electrical resistivity, Seebeck, and thermal conductivity were found to be approximately 5%, 20%, and 10%, respectively. The measured properties of the samples were not found to change with repeated thermal cycling, indicating high stability for the rare-earth vacancies.

High-temperature resonant ultrasound spectroscopy (RUS) measurements from 300 K to 573 K (300°C) were performed on bulk samples using a Magnaflux-RUS Quasar 4000 system under flowing argon to minimize oxidation with a frequency range of 0–500 kHz with 16.67-Hz step size. Data were analyzed using the Quasar2000 ClyModel software package.

DFT Calculations

The structural relaxation and electronic properties of La_3Te_4 and Pr_3Te_4 were computed with the open-source DFT software package Quantum Espresso.[37] It is well known that the f states in rare-earth compounds are not adequately described by standard local density approximation (LDA) and generalized-gradient approximation due to strong electronic correlation effects.[38,39] To address this shortcoming, PBE plus on-site Coulomb interaction (PBE + U) was used in this work.[40–42] The on-site Coulomb interaction serves to correct the self-interaction for the f electrons localized at the rare-earth sites. Projected augmented wave (PAW) potentials generated with the AUTOPAW program were used for La and Pr with an energy cutoff of 60 Ry for the wave functions and a charge density cutoff of 540 Ry.[43,44] Since Pr_3Te_4 and La_3Te_4 are metallic, the Mazari-Vanderbilt smearing scheme was used to expedite the convergence toward self-consistency.[45] Brillouin zone k-point sampling of 13 3 13 3 13 and 17 3 17 3 17 were used for the structural relaxation and transport property calculations (Seebeck coefficient), respectively. The choice of energy cutoff and k points was derived from the details of convergence tests.

La_3Te_4 and Pr_3Te_4 have the Th_3P_4 structure, belonging to the cubic crystal system and space group $I\bar{4}3d$.[4,7] The atomic positions of both structures were relaxed for various fixed lattice parameters. The lattice parameter corresponding to the minimum total energy is found to be 9.70 Å for La_3Te_4, in good agreement with the experimental values of 9.622 Å [7]. For Pr_3Te_4, we computed the lattice constant for several values of U. We found that U = 4.0 eV gives a relaxed lattice constant of 9.50 Å, in excellent agreement with the experimental value of 9.482 Å, with an error of ~0.2%.[30] At room or higher temperatures, both materials are paramagnetic. For this reason, we discuss the electronic properties of Pr_3Te_4 for non-spin polarized calculations, since it more closely describes the properties of Pr_3Te_4 at or above room temperature.

SUPPLEMENTAL INFORMATION

Supplemental Information includes nine figures and two tables and can be found with this article online at https://doi.org/10.1016/j.joule.2018.01.013.

ACKNOWLEDGMENTS

This work was performed at the California Institute of Technology/Jet Propulsion Laboratory under contract with the National Aeronautics and Space Administration. This work was supported by the NASA Science Missions Directorate under the Radioisotope Power Systems Program's Thermoelectric Technology Development Project.

AUTHOR CONTRIBUTIONS

Conceptualization, D.C., B.S.D., J.-P.F., and S.K.B.; Investigation, D.C., B.E.H., T.V., P.V.A., K.L., and D.S.; Formal Analysis, D.C., B.E.H., T.V., D.M.S., and A.Z.; Resources, A.Z., J.-P.F., and S.K.B.; Writing – Original Draft, D.C. and A.Z.; Writing – Review & Editing, K.L., D.M.S., A.Z., and S.K.B.; Supervision, B.S.D., J.-P.F., and S.K.B.; Funding Acquisition, J.-P.F. and S.K.B.

DECLARATION OF INTERESTS

The authors declare no competing interests.

Received: October 30, 2017
Revised: December 14, 2017
Accepted: January 26, 2018
Published: February 19, 2018

REFERENCES

1. Rowe, D.M. (1995). CRC Handbook of Thermoelectric Materials (CRC Press).
2. Yang, J., and Caillat, T. (2006). Thermoelectric materials for space and automotive power generation. MRS Bull. *31*, 224–229.
3. Fleurial, J.-P. (2009). Thermoelectric power generation materials: technology and application opportunities. JOM *61*, 74–85.
4. Wood, C. (1988). Materials for thermoelectric energy conversion. Rep. Prog. Phys. *51*, 459–539.
5. Vining, C.B., and Fleurial, J.-P. (1993). Silicon-Germanium: An Overview of Recent Development (AIP Press), pp. 87–120.
6. Snyder, G.J., and Toberer, E.S. (2008). Complex thermoelectric materials. Nat. Mater. *7*, 105–114.
7. May, A.F., Fleurial, J.-P., and Snyder, G.J. (2008). Thermoelectric performance of lanthanum telluride produced via mechanical alloying. Phys. Rev. B *78*, 125205.
8. Cutler, M., Leavy, J.F., and Fitzpatrick, R.L. (1964). Electronic transport in semimetallic cerium sulfide. Phys. Rev. *133*, A1143.
9. Cutler, M., and Leavy, J.F. (1964). Electronic transport in high-resistivity cerium sulfide. Phys. Rev. *133*, A1153.
10. Cutler, M., Fitzpatrick, R.L., and Leavy, J.F. (1963). The conduction band of cerium sulfide $Ce_{3-x}S_4$. J. Phys. Chem. Solid. *24*, 319–327.
11. Zhuze, P., Sergeeva, V.M., and Golikova, O.A. (1970). Kinetic processes in rare-earth chalcogenides having the composition Ln_3X_4. Sov. Phys. Solid State *11*, 2071.
12. Gadzhiev, G., Ismailov, S.M., Abdullaev, K.K., Kuramshin, M.M., and Orudzev, Z.M. (2001). Thermal and electrical properties of gadolinium sulfides at high temperatures. High Temp. *39*, 407–412.
13. Taher, S.M., and Gruber, J.B. (2001). Thermoelectric efficiency of rare earth sesquisulfides. Mat. Res. Bull. *16*, 1407–1412.
14. Vickery, R.C., and Muir, H.M. (1961). Thermoelectric properties of rare earth chalcogenides. Adv. Energy Convers. *1*, 179–186.
15. Wood, C., Lockwood, A., Parker, J., Zoltan, A., Zoltan, D., Danielson, L.R., and Raag, V. (1985). Thermoelectric properties of lanthanum sulfide. J. Appl. Phys. *58*, 1542–1547.
16. Danielson, L.R., Raag, V., and Wood, C. (1985). Thermoelectric properties of rare earth chalcogenides. Intersociety Adv. Energy Convers. Eng. Conf. Proc. *3*, 3.531–3.535.
17. Eliseev, A.A., Yaremchuk, E.I., Kuznetsov, Y.G., Volkova, E.S., Rzhevkin, A.A., and Andreeva, L.I. (1964). Tellurium lantana. Russ. J. Inorg. Chem. *9*, 876–881.
18. Ramsey, T.H., Steinfink, H., and Weiss, E.J. (1965). The phase equilibria and crystal chemistry of the rare earth-group VI systems. IV. Lanthanum-tellurium. Inorg. Chem. *4*, 1154–1157.
19. May, A.F., Singh, D.J., and Snyder, G.J. (2009). Influence of band structure on the large thermoelectric performance of lanthanum telluride. Phys. Rev. B *9*, 153101.
20. Vo, T., von Allmen, P., Huang, C.-H., Ma, J.M., Bux, S.K., and Fleurial, J.-P. (2014). Electronic and thermoelectric properties of Ce_3Te_4 and La_3Te_4 computed with density functional theory with on-site Coulomb interaction correction. J. Appl. Phys. *116*, 133701.
21. May, A.F., Fleurial, J.-P., and Snyder, G.J. (2010). Thermoelectric performance of lanthanum telluride produced via mechanical alloying. Chem. Mater. *22*, 2995–2999.
22. Ma, J.M., Clarke, S.M., Zeier, W.G., Vo, T., von Allmen, P., Snyder, G.J., Kaner, R.B., Fleurial, J.-P., and Bux, S.K. (2015). Mechanochemical synthesis and high temperature thermoelectric properties of calcium-doped lanthanum telluride $La_{3-x}Ca_xTe_4$. J. Mater. Chem. C *3*, 10459–10466.
23. Weber, M.J. (1979). Methods of Experimental Physics (Academic Press), Chp. 3.
24. Wu, W., Xuan, Y., Yin, J.N., and Xie, J. (2015). Influence of praseodymium doping concentration on the structural and optical properties of strontium molybdate crystals. Res. Chem. Inter. *41*, 2479–2488.
25. Lamberti, V.E., Rodriguez, M.A., Trybulski, J.D., and Navrotsky, A. (1996). Praseodymium and high-temperature superconductivity: thermodynamic, structural, and critical correlations. J. Mater. Res. *11*, 1061–1064.
26. Gschneidner, K.A., Nakahara, J.F., Beaudry, B.J., and Takeshita, T. (1987). Lanthanide refractory semiconductors based on the Th_3P_4 structure. Mat. Res. Soc. Symp. Proc. *97*, 359–370.
27. Golikova, O.A., Rudnev, M., Sergeeva, M., Kazanin, M.M., and Tsaplina, E.N. (1976). On the conductivity of rare-earth metal chalcogenides $Ln_{3-x}X_4$ ($0 < x < 0.33$). Phys. Status Solidi A *37*, 199–203.

28. Ashcroft, N.W., and Mermin, N.D. (1976). Solid State Physics (Harcourt College Publisher).

29. Mott, N.F., and Jones, H. (1936). The Theory of the Properties of Metals and Alloys (The Clarendon Press).

30. Mitarov, R.G., Tikhonov, V.V., Vasiliev, L.N., Golubkov, A.V., and Smirnov, I.A. (1975). Specific heat of Pr_3Te_4 and La_3Te_4. Phys. Status Solidi A *30*, 496–500.

31. Yanenkach, E.I., Eliseev, A.A., Vigdova, E.S., and Antonova, L.I. (1967). X-ray study of praseodymium tellurides. Inorg. Chem. *3*, 2184–2189.

32. Cox, W.L., Steinfink, H., and Bradley, W.F. (1966). The structure refinement of La_2Te_3, a Th_3P_4 type structure. Inorg. Chem. *5*, 318–319.

33. Kim, H.S., Gibbs, Z.M., Tang, Y., Wang, H., and Snyder, G.J. (2015). Characterization of Lorenz number with Seebeck coefficient measurement. APL Mater. *3*, 041506.

34. Toby, B.H., and Von Dreele, R.B. (2013). GSAS-II: the genesis of a modern open-source all purpose crystallography software package. J. App. Cryst. *46*, 544–549.

35. Borup, K.A., Toberer, E.S., Zoltan, L.D., Nakatsukasa, G., Errico, M., Fleurial, J.-P., Iversen, B.B., and Snyder, G.J. (2012). Measurement of the electrical resistivity and Hall coefficient at high temperatures. Rev. Sci. Instr. *83*, 123902.

36. Wood, C., Zoltan, D., and Stapfer, G. (1985). Measurement of Seebeck coefficient using a light pulse. Rev. Sci. Instr. *56*, 719–722.

37. Giannozzi, P., Baroni, S., Bonini, N., Calandra, M., Car, R., Cavazzoni, C., Ceresoli, D., Chiarotti, G.L., Cococcioni, M., Dabo, I., et al. (2009). QUANTUM ESPRESSO: a modular and open-source software project for quantum simulations of materials. J Phys Condens Matter. *21*, 395502.

38. Kohn, W., and Sham, L.J. (1965). Self-consistent equations including exchange and correlation effects. Phys. Rev. *140*, A1133.

39. Perdew, J.P., Burke, K., and Ernzerhof, M. (1996). Generalized gradient approximation made simple. Phys. Rev. Lett. *77*, 3865.

40. Anisimov, V.I., Zaanen, J., and Andersen, O.K. (1991). Band theory and Mott insulators: Hubbard U instead of Stoner I. Phys. Rev. B *44*, 943.

41. Anisimov, V.I., Solovyev, I.V., Korotin, M.A., Czyżyk, M.T., and Sawatzky, G.A. (1993). Density-functional theory and NiO photoemission spectra. Phys. Rev. B *48*, 16929.

42. Cococcioni, M., and De Gironcoli, S. (2005). Linear response approach to the calculation of the effective interaction parameters in the LDA+ U method. Phys. Rev. B *71*, 035105.

43. Holzwarth, N.A.W., Tackett, A.R., and Matthews, G.E. (2001). A Projector Augmented Wave (PAW) code for electronic structure calculations, Part I: atompaw for generating atom-centered functions. Comput. Phys. Comm. *135*, 329–347.

44. Tackett, A.R., Holzwarth, N.A.W., and Matthews, G.E. (2001). A Projector Augmented Wave (PAW) code for electronic structure calculations, Part II: atompaw for periodic solids in a plane wave basis. Comput. Phys. Comm. *135*, 348–376.

45. Marzari, N., Vanderbilt, D., De Vita, A., and Payne, M.C. (1999). Thermal contraction and disordering of the Al (110) surface. Phys. Rev. Lett. *82*, 3296.

Appendix B Supporting Information for Chapter 3 (Mechanical Properties for $RE_{3-x}Te_4$)

Materials Today Physics 32 (2023) 101016

Contents lists available at ScienceDirect

Materials Today Physics

journal homepage: www.journals.elsevier.com/materials-today-physics

Using vacancies to tune mechanical and elastic properties in $La_{3-x}Te_4$, $Nd_{3-x}Te_4$, and $Pr_{3-x}Te_4$ rare earth telluride thermoelectric materials

James P. Male [a,b], Brea Hogan [b,c], Max Wood [b], Dean Cheikh [b], G. Jeffrey Snyder [a,*], Sabah K. Bux [b]

[a] Department of Materials Science & Engineering, Northwestern University, Evanston, IL, USA
[b] Thermal Energy Conversion Material Research Group, Jet Propulsion Laboratory/California Institute of Technology, Pasadena, CA, 91109, USA
[c] Department of Materials Science and Engineering, University of California, Los Angeles, CA, 90095, USA

ARTICLE INFO

Keywords:
Thermoelectrics
Doping
Hardness
Mechanical properties
Thermal expansion

ABSTRACT

Elastic and mechanical properties in advanced $RE_{3-x}Te_4$ (RE = La, Pr, Nd) thermoelectric materials are found to depend considerably on cation vacancy concentration x. Increasing x, which simultaneously reduces charge carrier concentration from metal-like to semiconductor-like, leads to significant stiffening of elastic constants due to charge carrier effects. The coefficient of thermal expansion in $La_{3-x}Te_4$ determined by high temperature X-ray diffraction correspondingly decreases with x, indicating that thermal expansion may be tuned by x in $RE_{3-x}Te_4$ materials systems. Vickers indentation hardness and fracture toughness tests show similarly significant effects of x on hardness and mode I fracture toughness, both of which decrease with increasing x. The mechanical property trends are counter-intuitive and merit further investigation, but demonstrate overall that higher x in $RE_{3-x}Te_4$ leads to more brittle behavior. The combined results show the importance of intrinsic defects in $RE_{3-x}Te_4$ and the potential to tune the mechanical performance of $RE_{3-x}Te_4$ for practical implementation in next-generation thermoelectric devices.

1. Introduction

Rare earth (RE) tellurides (RE_3Te_4) with the Th_3P_4 structure type are promising high-temperature (> 1000 K) thermoelectric materials for converting waste heat to electricity [1–7]. The operating temperature range for RE_3Te_4 materials makes them particularly good candidates for next-generation radioisotope thermoelectric generators, which produce power in deep space from high-temperature decaying nuclear material [8–10]. However, as in many promising thermoelectric materials like PbTe [11], $Yb_{14}MnSb_{11}$ [12], and Bi_2Te_3 [13], practical implementation of RE_3Te_4 is difficult due to shortcomings in the seldom-studied mechanical and elastic properties [14].

RE_3Te_4 materials are degenerately doped n-type by native electron count when the cation site is fully filled. The 9 donated electrons from 3 RE cations surpass the 8 accepted by the Te anion, leading to one excess electron per formula unit. Electron concentrations in vacancy-free RE_3Te_4 materials ($\sim 4.5 \times 10^{22}$ cm^{-3}) far exceed typical optimal doping levels for thermoelectric performance ($\sim 10^{20}$ cm^{-3} [15]), meaning carrier concentrations must be lowered by adding vacancies or extrinsic dopants [1,5,15]. Most RE_3Te_4 materials of interest for thermoelectrics can reach "charge balance" by accommodating up to $x = 1/3$ RE vacancies in $RE_{3-x}Te_4$ without deviating from the Th_3P_4 structure. Therefore, a wide single phase region exists between the metallic RE_3Te_4 and the semiconducting RE_2Te_3 stoichiometries, across which vacancies (and carrier concentration) can be finely tuned [1,16].

Since $RE_{3-x}Te_4$'s were first identified as good thermoelectric materials in the mid 20th century [16,17], $RE_{3-x}Te_4$ materials with RE = La, Pr, and Nd have received the most attention for thermoelectric use [1–3,5,15]. The similar chemistry between the RE elements leads to similar character between the $RE_{3-x}Te_4$ materials, although additional, heavy mass f-states in $Pr_{3-x}Te_4$ and $Nd_{3-x}Te_4$ (due to higher f electron count) may increase thermoelectric performance relative to $La_{3-x}Te_4$ [2,3].

For any of the n-type $RE_{3-x}Te_4$ materials mentioned above to be practically useful in deep space applications, they must integrate well with other parts of the thermoelectric device including the interconnects, hot/cold shoes, the p-type leg, and other thermoelectric materials used for segmentation. Materials with vastly different elastic properties or thermal expansion coefficients may crack or delaminate

* Corresponding author.
E-mail address: jeff.snyder@northwestern.edu (G.J. Snyder).

https://doi.org/10.1016/j.mtphys.2023.101016
Received 12 December 2022; Received in revised form 7 February 2023; Accepted 12 February 2023
Available online 15 February 2023

from stresses caused by large temperature gradients [18]. Thermoelectrics used for space missions in particular are subjected to mechanical stresses at every stage of development, including machining and sectioning of materials, vibrations during launch, and high-temperature creep during long-term operation [19]. Unfortunately, thermoelectric materials tend to have poor mechanical properties, and some impressive thermoelectric materials synthesized in laboratories may fail to see usage without addressing mechanical shortcomings [20].

The available literature on mechanical performance in thermoelectric materials suffers from difficulties with mechanical property testing. Good thermoelectric materials are often too expensive and brittle – and their synthesis too arduous – to achieve the form factor and quantity required for standardized mechanical property tests like tensile tests and notched three-point bend tests. Instead, initial forays into quantifying mechanical performance in thermoelectric materials tend to rely on computational models or cheaper experiments like Vickers hardness tests [14,20–24]. Vickers microhardness measurements and fracture toughness estimated from Vickers indentation cracks were reported in $La_{2.74}Te_4$ (x near the optimum for high-temperature performance) by Ma et al. [14], who later measured reduced spalling from indentation tests and increased strength when compositing $La_{2.74}Te_4$ with metallic Ni or Co [25,26]. Li et al. took a computational approach, determining the shear strain of La_3Te_4 using density functional theory [24]. The effects of changing the RE element or x in $RE_{3-x}Te_4$ are thus far unexplored – a clear shortcoming in the quest to make these materials resilient for deep space power generation.

Elastic property measurements are relatively facile compared to mechanical property testes in $RE_{3-x}Te_4$ samples, as they typically do not require unique geometries or large sample quantities. Elastic measurements are available in several Th_3P_4 structure compounds with interesting thermoelectric and/or superconducting properties, often with values reported as a function of vacancy concentration [1,4,27–31]. Reported elastic properties can vary among authors, even within a single system like $La_{3-x}Te_4$ [1,29,30], but one key finding remains consistent: the crystal lattice *stiffens* as vacancies are introduced into Th_3P_4 structure materials ($Th_{3-x}P_4$). Sound velocities (measured directly or calculated from Debye temperatures), show stiffening from vacancies upwards of 30% in $La_{3-x}S_4$ and between 5 and 20% for $La_{3-x}Te_4$. Bond stiffening from vacancies is an initially surprising result, but may result from reduced electronic carrier concentrations (an effect recently called charge carrier mediated softening) [30,31]. A key consideration thus far overlooked is the relation between such stiffening and the mechanical performance of $RE_{3-x}Te_4$ thermoelectric materials. The role of vacancies and bond stiffness on mechanical properties and thermal expansion should be significant, and may hold the key to tuning and improving mechanical performance.

In this study, we utilize speed of sound measurements, Vickers microhardness tests, and X-ray diffraction to explore the interrelation between mechanical properties, elastic properties, and thermal expansion in $RE_{3-x}Te_4$ (RE = La, Pr, Nd) thermoelectric materials. We perform all measurements on $RE_{3-x}Te_4$ samples with different x to explore trends with changing vacancy concentrations and electronic carrier concentrations.

2. Results & discussion

Polycrystalline average speed of sound (v_s) measurements in $La_{3-x}Te_4$, $Pr_{3-x}Te_4$, and $Nd_{3-x}Te_4$ show linearly increasing v_s with increasing cation vacancy concentrations (x) up to $x = 1/3$ (Fig. 1). Elastic moduli determined using an isotropic polycrystalline approximation are included in Table 1. The choice of rare earth (RE) cation in $RE_{3-x}Te_4$ appears insignificant for elastic properties, which trend similarly with x in $La_{3-x}Te_4$, $Nd_{3-x}Te_4$, and $Pr_{3-x}Te_4$. In all three systems, v_s increases as much as 7%, a change comparable to other systems like PbTe where lattice softening is intentionally introduced through heavy defect engineering [34]. The 7% stiffening is also consistent with other

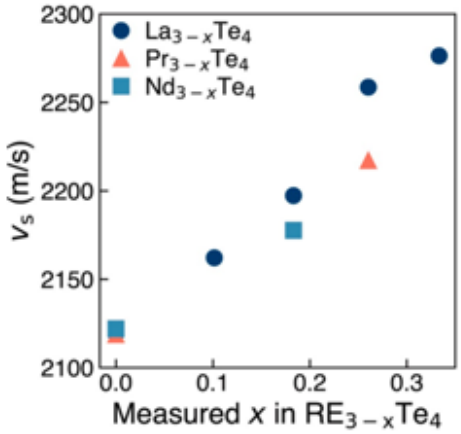

Fig. 1. (a) Linear increase in polycrystalline average speed of sound (v_s) with increasing nominally measured x in $RE_{3-x}Te_4$ (RE = La, Pr, Nd).

$RE_{3-x}Te_4$ literature [1,28,29,31], although the work by Delaire et al. [30] shows more drastic stiffening in $La_{3-x}Te_4$, potentially due to differences in measurement method.

Elastic stiffening with increasing vacancy concentrations may not appear intuitive. One might expect high point defect concentrations to cause disorder, weaken bonds, and decrease v_s, as seen in other materials systems [20,34–37]. However, the $RE_{3-x}Te_4$ materials explored here have uniquely wide ranges of Hall carrier concentrations (n_H) associated with the cation vacancies. For example, the nominal n_H between La_3Te_4 ($x = 0$) and La_2Te_3 ($x = 1/3$) from vacancy count in Table 1 spans several orders of magnitude, from a metal-like n_H towards zero (in reality, La_2Te_3 has a low n_H similar to an intrinsic semiconductor [1]). Softer bonds in RE_3Te_4 with $x = 0$ (one electron per formula unit by charge counting) likely result from the high concentration of excess electrons. Extra electrons may occupy antibonding orbitals, and/or shield ionic bonds, leading to weaker bonding overall. This effect has been observed previously in a host of thermoelectric materials (including $RE_{3-x}Te_4$ materials) [31] and was dubbed "charge carrier softening".

Vickers microhardness also trends linearly with increasing x in $RE_{3-x}Te_4$ materials (Fig. 2a), ultimately decreasing about 15% from $x = 0$ to $x = 0.33$ in $La_{3-x}Te_4$. Hardness is virtually identical between the three $RE_{3-x}Te_4$ samples explored in this study suggesting that, like elastic properties, hardness is largely unaffected by choice of RE element in $RE_{3-x}Te_4$ systems. Vickers microhardness tests were used to probe mechanical properties given the cost and difficulty of synthesizing brittle $RE_{3-x}Te_4$ to the dimensions and quantity necessary for more thorough mechanical testing. Despite the simplicity of the method, the changing hardness as a function of vacancy concentration presented in Fig. 2a provides an illustrative view into the effect of changing x on mechanical properties.

Fracture toughness decreases linearly in Fig. 2b (up to 22% in $La_{3-x}Te_4$) as vacancies are added to the $RE_{3-x}Te_4$ samples – similar to the trend in mechanical hardness. A seemingly less drastic effect on K_c with increasing x in $Nd_{3-x}Te_4$ merits further exploration, although additional samples with $x > 0.26$ were not studied here due to a potential phase transition [3]. Fracture toughness represents the ability of a material to resist crack propagation under stress, with different forms of fracture toughness designating different modes of crack opening. Here, we approximate the tensile crack opening fracture toughness mode, K_c, using crack lengths extending from each corner of the Vickers indentation pyramid (see inset in Fig. 2b for example) following a Vickers indentation fracture toughness test (VIF). Such cracking behavior is common in brittle materials as opposed to ductile materials, in which a propagating crack may be blunted or deflected due to local

Table 1

Summary of measurements on $RE_{3-x}Te_4$ (RE = La, Pr, Nd) including the calculated n-type Hall carrier concentration n_e from electron counting, longitudinal and transverse speed of sounds (v_L and v_T respectively), polycrystalline average speed of sound calculated using the isotropic approximation $\left(v_{avg} = \left(\frac{1}{3}\left[1/v_L^3 + 2/v_T^3\right]\right)^{-1/3}\right)$, bulk modulus (K) and shear modulus (G) calculated from v_L and v_T, Vickers microhardness from a 0.2 kgf load (HV0.2) and mode I fracture toughness (K_{Ic}) estimated using the Vickers indentation fracture toughness method following the Shetty model.

Nominal	Calc. n_e ($\times 10^{21}$ cm^{-3})	v_L (m/s)	v_T (m/s)	v_{avg} (m/s)	K (GPa)	G (GPa)	HV0.2 (MPa)	K_{Ic} MPa$\sqrt{m}$
La_3Te_4	4.4	3607	1895	2119	56.7	24.8	451(6)	0.72(2)
$La_{2.88}Te_4$	3.1	3650	1934	2162	58.3	26.2	422(6)	0.68(3)
$La_{2.82}Te_4$	2.0	3633	1969	2197	56.8	27.4	407(8)	0.67(4)
$La_{2.74}Te_4$	0.99	3715	2025	2258	59.6	29.3	395(6)	0.60(5)
La_2Te_3	0	3696	2043	2276	58.5	30.1	392(10)	0.59(2)
Pr_3Te_4	4.7	3586	1895	2119	58.6	26.1	454(6)	0.71(4)
$Pr_{2.74}Te_4$	1.0	3630	1988	2217	54.4	27.2	400(7)	0.68(1)
Nd_3Te_4	4.8	3539	1900	2122	57.5	26.8	453(8)	0.72(3)
$Nd_{2.92}Te_4$	2.2	3557	1953	2178	54.9	27.7	402(9)	0.72(4)

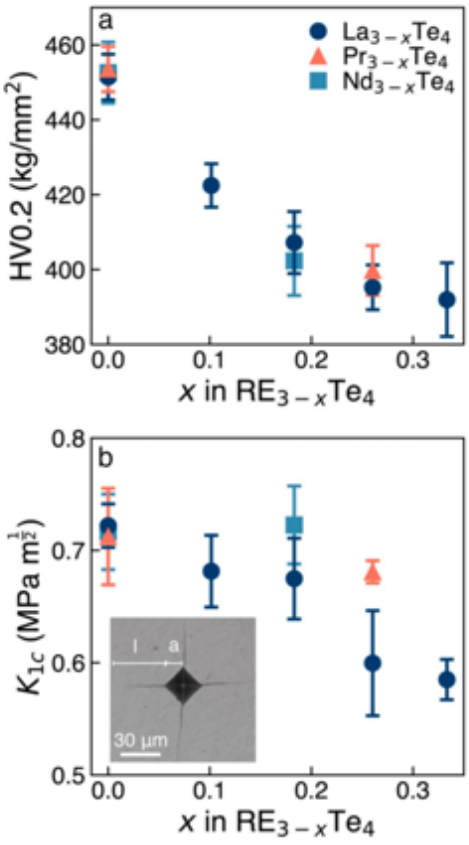

Fig. 2. (a) Measured Vickers hardness from 0.2 kgf indent (HV0.2) in $RE_{3-x}Te_4$ (RE = La, Pr, Nd) versus cation vacancy concentration x. (b) Mode I fracture toughness K_{Ic} estimated from Vickers indentation crack lengths using the Shetty equation [32,33]. Error bars in both plots represent the first standard deviation from > 5 indents. The inset in (b) shows an example 0.2 kgf Vickers indent taken on a $Pr_{3-x}Te_4$ sample with x = 0.26, with indications of the l and a parameters used to estimate K_{Ic}

plastic deformation near the crack tip. Notably, the significant decrease in K_{Ic} with x follows the qualitatively perceived brittleness of the samples. Samples with $x \approx 0$ were fairly robust and stayed intact during polishing, while samples with high x easily broke into several pieces despite extreme care in handling. A similar, qualitative increase in brittleness with x was also reported in the $La_{3-x}S_4$ system [38].

While the VIF method has serious shortcomings in accurately discerning K_{Ic} [39,40], it remains a powerful tool for comparing mechanical properties between different samples [41]. More accurate tests of fracture toughness like notched three-point bend tests are thus far unavailable in the $RE_{3-x}Te_4$ literature and will require a large undertaking to prepare adequate numbers of samples. Regardless, we remain focused on the mechanical property trends with vacancies rather than absolute values of K_{Ic} and we expect the decreasing K_{Ic} with x trend to remain. Our chosen VIF method follows the work of Shetty [32,41,42]. Shetty's model works well for brittle materials that experience Palmqvist surface cracking upon indentation. Palmqvist cracking can be assumed when surface crack lengths are less than $\frac{a}{2}$, the length of half of an indentation pyramid, which is true for all measurements in this study. A simplified version of Shetty's model, which is valid when the Poisson's ratio ν is near 0.25 is given by $K_{Ic} = 0.0319P/(al^{1/2})$, where P is the indenter load, a is the half length of the Vickers indentation, and l is the average crack length measured from the corner of the indentation [41]. Ma, using the same model, reported K_{Ic} = 0.67 MPam$^{1/2}$ in $La_{2.74}Te_4$ (x = 0.26) with a 0.2 kgf indentation load [14], similar to our finding of 0.60 MPam$^{1/2}$.

Notably, the samples with the lowest hardness and K_{Ic} in Fig. 2 (highest x samples) also have the stiffest elastic properties in Fig. 1. Hardness is a complicated property driven more by plasticity than elasticity. Strictly, Vickers microhardness measures the penetration depth of a pyramidal Vickers tip into the surface of a material at a given load and load application time [43]. While a stiffer material resists the movement of a Vickers indenter more than a soft material, the indentation size primarily involves the ability for the material to deform around the indenter tip, which depends strongly on ease of nucleating and moving dislocations [44]. Therefore, the 7% stiffening with increasing x in Fig. 1 does not necessarily contradict the lower hardness in Fig. 2a.

In Fig. 2b, fracture toughness increases with hardness and decreases with v_a. These trends are opposite the expectation in well-studied, classic systems like WC ceramics, metals, and intermetallics, which tend to increase in K_{Ic} with stiffening elastic constants and reducing hardness [45,46]. In the vast majority of studies investigating hardness and fracture toughness, the material in question retains its fundamental character even when defects like vacancies are introduced, i.e. a metal with vacancies remains a metal. Conversely, the $RE_{3-x}Te_4$ samples in this study (and many other thermoelectric material systems) are unique because they can be doped to the level of either a metal or an intrinsic semiconductor. Accordingly, the changing x in RE—Te affects bonding, the Fermi level, and the density of states near the Fermi level in the material, all while simultaneously introducing intrinsic defects (vacancies) well-known to affect plasticity. Therefore, we conjecture that the wide-range of electronic properties in a single thermoelectric system may lead to unique and interesting trends in mechanical properties that merit further exploration.

Other potential explanations for the trends observed in Fig. 2 can not be ruled out. $RE_{3-x}Te_4$ materials tend to tarnish and oxidize in air far more rapidly with higher x. This deterioration of the material may affect mechanical properties, perhaps by weakening grain boundaries, creating internal flaws, or precipitating secondary phases near the sample surface. Previous work shows that grain size effects are essentially negligible for K_{IC} in $La_{3-x}Te_4$ with $x = 0.26$ prepared in a similar manner to this work [14]. However, interactions between dislocations and vacancies or microstructure (secondary phases, grain boundaries) are poorly understood in this system, and may have unanticipated effects on hardness and K_{IC}.

Temperature-dependent powder X-ray diffraction (pXRD) patterns in Fig. 3 rule out significant bulk secondary phase effects on mechanical properties at room temperature while providing additional insight into the effects of elastic stiffening with increasing x. The pXRD patterns at room temperature show mostly the $La_{3-x}Te_4$ phase within the detectable limits of the instrument for all samples except the $x = 0.33$ powder, which has some small fraction of secondary phases. Additional secondary phases form in all of the powders at higher temperatures as expected given a propensity for La-containing compounds to react with quartz vessels like those used in this experiment [1].

The coefficient of thermal expansion (α) was produced from temperature-dependent lattice parameter measurements in $La_{3-x}Te_4$ (Fig. 4). The calculated $\alpha = 1.6 \times 10^{-5}$ K^{-1} for $x = 0.26$ here is comparable to $\alpha = 1.5 \times 10^{-5}$ K^{-1} measured by May et al. in $La_{3-x}Te_4$ with $x = 0.19$ [1]. The values correspond to second order polynomial fits to the temperature-dependent pXRD lattice parameters, and represent average α values between 298 K and 673 K. Data is left out of the analysis above 673 K (but included in the SI) due to an upwards curve in lattice parameters with temperature in some samples. Such behavior is not observed elsewhere [1,30,47], and may be a consequence of $La_{3-x}Te_4$ reacting with the quartz capillaries at high temperatures or the changing temperature step from 50 K to 100 K above 673 K. Regardless, when the high temperature lattice parameters are included, the same general decrease in α with x remains.

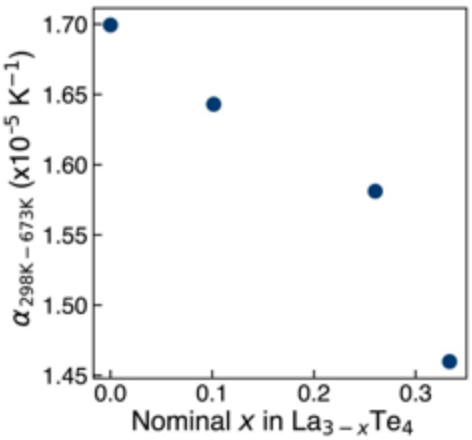

Fig. 4. Average thermal expansion (α) between 298 K and 673 K of $La_{3-x}Te_4$ as a function of x. Values are determined a second order polynomial fit of temperature-dependent x-ray diffraction lattice parameter measurements.

The decreasing α with increasing x in $La_{3-x}Te_4$ is consistent with Fig. 1 and Table 1 data given the close link between α and elastic stiffness – stiffening the bonds of a material suppresses its ability to expand. Therefore, the reduced α likely stems from charge carrier softening,

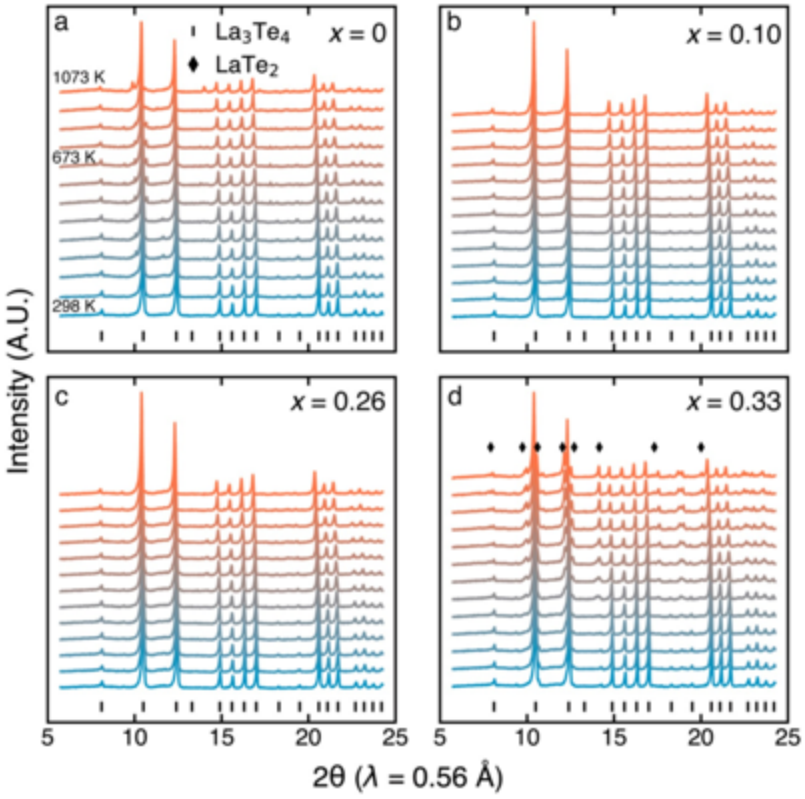

Fig. 3. High temperature X-ray diffraction between 298 K and 1073 K for $La_{3-x}Te_4$ with (a) $x = 0$, (b) $x = 0.10$, (c) $x = 0.26$, (d) $x = 0.33$ from a AgKα source ($\lambda = 0.56$ Å). Intensity is given in arbitrary units. Each waterfall plot contains the same measurement temperatures, with 50 K increments from 298 K to 673 K, followed by 100 K increments between 1073 K. The majority phase is indexed as La_3Te_4 in (a–c), with more degradation and significant $LaTe_2$ forming in (d). $LaTe_2$ phases are identified and were included in refinements, while the other impurity peaks were left untreated.

which similarly leads to higher v_s (and other elastic constants) at high x. Likewise, we expect similar trends in α for the other RE cations given the similar v_s trends observed with x in $Pr_{3-x}Te_4$ and $Nd_{3-x}Te_4$. The linearly changing α with x has significant implications for materials selection in thermoelectric modules. Thermal expansion mismatch can lead to undue stresses and catastrophic failure of a device at high temperatures [18]. Accordingly, thermoelectric devices are largely restricted to material combinations with similar α for the n- and p-type legs or for segmented leg materials. The fairly wide range of achievable α demonstrated here in $La_{3-x}Te_4$ implies that α can be tuned by changing x, which may expand the viable thermoelectric materials for partnering with $RE_{3-x}Te_4$ materials in next-generation thermoelectric devices.

3. Conclusions

$RE_{3-x}Te_4$ (RE = La, Pr, Nd) thermoelectric materials have high thermoelectric conversion efficiency but poor mechanical performance. This work illuminates the crucial role of vacancies (x) on elastic and mechanical properties in $RE_{3-x}Te_4$: increasing x stiffens and embrittles $RE_{3-x}Te_4$ materials. While elastic stiffening may be attributed to electronic carrier effects, the origin of embrittlement with increasing x is less certain. However, the mechanical property trends highlight the unique, underappreciated, and poorly understood nature of mechanical properties in thermoelectric materials, which may vary considerably across a wide range of doping levels. A significant change in thermal expansion with x suggests that $RE_{3-x}Te_4$ materials can be engineered by changing x to match the thermal expansion of other materials in a thermoelectric device to suppress thermal stress effects. Further, the intriguing trends involving x and carrier concentration merit further studies with other RE cations and extrinsic dopants, as well as microstructure studies, to better discern the exact mechanisms driving mechanical performance in this family of thermoelectric materials.

4. Experimental methods

$RE_{3-x}Te_4$ (RE = La, Pr, Nd) samples were synthesized from elemental La (HEFA Rare Earth Canada, 99.9%), Pr (Stanford Advanced Materials, 99.9%), Nd (Stanford Advanced Materials, 99.9%), and Te (5 N Plus, 99.999%) using a mechanochemical synthesis method common in easily-oxidized, high melting point thermoelectric materials [1,48]. The constituent elements were combined in an Ar-filled glovebox with nominal stoichiometries corresponding to x = 0–0.33. The weighted materials were then sealed into a stainless steel jar with stainless steel balls in an Ar environment, then loaded into a SPEX SamplePrep 8000 high energy ball miller and ball milled for over 10 h. The resulting powders were loaded into 0.5 in diameter graphite dies in an Ar glovebox then spark plasma sintered under vacuum. Pressing was carried out at 80 MPa pressure over 1000C for 30 min. The resulting cylindrical pellets were measured to have >98% theoretical density by Archimedes measurements in isopropyl alcohol.

Speed of sound was measured using a pulse-echo method with 5 MHz longitudinal and transverse transducers (Olympus V1091 and V157-RM) and a Tektronix TBS 1072B-EDU oscilloscope for recording waveforms. Transducers were affixed to samples using honey as a coupling agent, and the time between sound wave reflections was measured and used along with material thickness to calculate longitudinal and transverse sound velocities (v_l and v_t respectively). Error in this system is expected to vary by less than 1% [49] for a uniform thickness sample. Each sample was polished carefully to achieve less than 1% thickness variation across at least 5 unique locations on the sample.

Hardness was measured using the Vickers indentation method. All samples were polished to a 1 μm finish. An oil-based 1 μm suspension was used for the final polishing step to suppress oxidation. Hardness and fracture toughness measurements were performed using a Wilson VH 3100 hardness tester with an integrated optical microscope. Different indenter loads for several samples are included in the SI. Generally, hardness decreased with increased load and roughly approached a lower bound – a trend similar to previous work and attributed to the indentation size effect [14]. Samples with higher x spalled far more easily – a qualitative indicator of greater brittleness. For example, samples with x = 1/3 sometimes spalled under loads as low as 0.05 kgf, while samples with x near 0 remained fairly resilient to spalling at 0.5 kgf. All mechanical property measurements in Table 1 and Fig. 2 use 0.2 kgf load, at which all samples were reasonably close to converging on lower hardness bound while remaining resilient enough to spalling to get good statistics (at least 10 indents per sample). Hardness and crack length from Vickers indentations for several samples are plotted against indenter load in the supplemental information.

$La_{3-x}Te_4$ samples for powder XRD were hand ground using a mortar and pestle in an Ar-filled glovebox and sealed in carbon coated 0.5 mm diameter quartz capillary tubes under vacuum. Samples were then loaded into spinning stage contained within a furnace in a Stoe STADI-MP diffractometer configured in Debye-Sherrer geometry. The diffractometer was equipped with a AgKα source (λ = 0.56 Å). Samples were heated at 20 K/min to a target temperature and allowed to stabilize, then patterns were recorded across a single range between 2θ 5–25. Diffraction patterns were recorded in 50 K increments between 298 K and 673 K, then in 100 K increments between 673 K and 1073 K to suppress potential oxidation from extended exposure to at high temperatures.

Lattice parameters for calculating linear thermal expansion were determined by Rietveld refinement in the GSAS-II software [50]. Instrument parameter files were determined using a LaB_6 standard before refinements. Refinements began on a room temperature sample, then were extended to higher temperatures using the sequential refinement feature. Lattice parameter and background (Chebyshev polynomial with 6–8 variables) were refined first, followed by broadening from strain and particle size (crystallite size remained above 10 μm). Finally, atomic fractions, atomic coordinates, and thermal displacements were refined. Significant intensity from a $LaTe_2$ was identified at moderate to high temperatures in the patterns for $La_{3-x}Te_4$ with x = 0.33. Thus, for this sample, phase fractions of La_3Te_4 and $LaTe_2$ were also sequentially refined. Completing sequential refinements with and without the $LaTe_2$ phase included had little to no effect on the refined lattice parameter of the La_3Te_4 phase in this instance, suggesting that small amounts of impurity do not affect the determination of the linear thermal expansion coefficient in this work. An example pattern and refinement fit for La_3Te_4 is included in the supplementary information.

Credit author statement

James Male: Conceptualization, Methodology, Formal analysis, Investigation, Writing - Original Draft, Visualization; **Brea Hogan**: Methodology, Investigation, Resources, Writing - Review & Editing; **Max Wood**: Methodology, Writing - Review & Editing, Supervision; **Dean Cheikh**: Methodology, Writing - Review & Editing, Supervision; **G. Jeffrey Snyder**: Supervision, Project administration, Writing - Review & Editing, Funding acquisition; **Sabah Bux**: Supervision, Project administration, Writing - Review & Editing, Funding acquisition.

Declaration of competing interest

The authors declare that they have no known competing financial interests or personal relationships that could have appeared to influence the work reported in this paper.

Data availability

Data will be made available on request.

Acknowledgements

This work made use of the MatCI Facility supported by the MRSEC program of the National Science Foundation (DMR-1720139) at the Materials Research Center of Northwestern University. Work by James P. Male was supported by a National Aeronautics and Space Administration (NASA) Space Technology Graduate Research Opportunity. James P. Male and G. Jeffrey Snyder thank Award 70NANB19H005 from the U.S. Department of Commerce, National Institute of Standards and Technology, as part of the Center for Hierarchical Materials Design (CHiMaD). A portion of this work was performed at the California Institute of Technology/Jet Propulsion Laboratory under contract with NASA. This work was supported by the NASA Science Missions Directorate under the Radioisotope Power Systems Program's Technology Management Task.

Appendix A. Supplementary data

Supplementary data to this article can be found online at https://doi.org/10.1016/j.mtphys.2023.101016.

References

[1] A.F. May, J.P. Fleurial, G.J. Snyder, Thermoelectric performance of lanthanum telluride produced via mechanical alloying, Phys. Rev. B Condens. Matter 78 (12) (2008) 1–12, https://doi.org/10.1103/PhysRevB.78.125205.

[2] D. Cheikh, B.E. Hogan, T. Vo, P. Von Allmen, K. Lee, D.M. Crawford, A. Zevalkink, B.S. Dunn, J.P. Fleurial, S.K. Bux, Praseodymium telluride: a high-temperature, high-ZT thermoelectric material, Joule 2 (4) (2018) 698–709, https://doi.org/10.1016/j.joule.2018.01.013, doi:10.1016/j.joule.2018.01.013.

[3] S.J. Gomez, D. Cheikh, T. Vo, P. Von Allmen, K. Lee, M. Wood, G.J. Snyder, B. S. Dunn, J.P. Fleurial, S.K. Bux, Synthesis and characterization of vacancy-doped neodymium telluride for thermoelectric applications, Chem. Mater. (2019), https://doi.org/10.1021/acs.chemmater.9b00964.

[4] F. Qin, S.A. Nikolaev, A. Zevalkink, M. Wood, Y. Zhu, X. Tan, H. Avdeenko, Y. Ren, Q. Yan, L. Hu, G.J. Snyder, Crystal structure and atomic vacancy optimized thermoelectric properties in gadolinium selenides, Chem. Mater. 32 (23) (2020) 10130–10139, https://doi.org/10.1021/acs.chemmater.0c03581.

[5] J.M. Ma, S.M. Clarke, W.G. Zeier, T. Vo, P. Von Allmen, G. Jeffrey Snyder, R. B. Kaner, J.P. Fleurial, S.K. Bux, Mechanochemical synthesis and high temperature thermoelectric properties of calcium-doped lanthanum telluride La3-xCaxTe4, J. Mater. Chem. C 3 (40) (2015) 10459–10466, https://doi.org/10.1039/C5TC01648G, doi:10.1039/c5tc01648g.

[6] T. Vo, P. Von Allmen, C.K. Huang, J. Ma, S. Bux, J.P. Fleurial, Electronic and thermoelectric properties of Ce3Te4 and La3Te4 computed with density functional theory with on-site Coulomb interaction correction, J. Appl. Phys. 116 (13) (2014), https://doi.org/10.1063/1.4896670 doi:10.1063/1.4896670.

[7] X. Wang, R. Yang, Y. Zhang, P. Zhang, Y. Xu, Rare earth chalcogenide Ce3 Te4 as high efficiency high temperature thermoelectric material, Appl. Phys. Lett. 98 (22) (2011) 3–6, https://doi.org/10.1063/1.3597409.

[8] X. Wang, R. Liang, P. Fisher, W. Chan, J. Xu, Critical Design Features of Thermal-Based Radioisotope Generators: A Review of the Power Solution for Polar Regions and Space, vol. 3, 2020, https://doi.org/10.1016/j.rser.2019.109572, 10.1016/j.rser.2019.109572.

[9] M.B. Smith, C. Whiting, C. Bayliss, Nuclear considerations for the application of lanthanum telluride in future radioisotope power systems, in: 2019 IEEE Aerospace Conference Proceedings, IEEE, 2019, pp. 1–11, https://doi.org/10.1109/AERO.2019.8742136.

[10] C.S. Maxwell, D.F. Woerner, T.J. Hendricks, J.P. Fleurial, K.I. Gerdes, C. D. Bayless, J.F. Zakrajsek, Next-generation radioisotope thermoelectric generator study, in: IEEE Aerospace Conference Proceedings 2018-March, 2018, pp. 1–9, https://doi.org/10.1109/AERO.2018.8396738.

[11] Y. Gelbstein, Z. Dashevsky, M.P. Dariel, The search for mechanically stable PbTe based thermoelectric materials, J. Appl. Phys. 104 (3) (2008): 33702, https://doi.org/10.1063/1.2963359 doi:10.1063/1.2963359.

[12] G. Cerretti, O. Villalpando, J.P. Fleurial, S.K. Bux, Improving electronic properties and mechanical stability of Yb14Mn5Sb11 via W compositing, J. Appl. Phys. 126 (17) (2019): 175102, https://doi.org/10.1063/1.5118227.

[13] N. Peranio, G. Spiridonov, Z. Dashevsky, Y. Gelbstein, Thermoelectric, structural, and mechanical properties of spark-plasma-sintered chalcogenide and chalcogenide-based p-type Bi0.5Sb1.5Te3, J. Electron. Mater. 41 (6) (2012) 1546–1553, https://doi.org/10.1007/s11664-012-1950-8.

[14] J.M. Ma, S.A. Nikolaev, R.B. Kaner, J.P. Fleurial, V.A. Ravi, Hardness and fracture toughness of thermoelectric La3-x Te4, J. Mater. Sci. 49 (3) (2014) 1150–1156, https://doi.org/10.1007/s10853-013-7794-7.

[15] A.F. May, J.P. Fleurial, G.J. Snyder, Optimizing thermoelectric efficiency in La3-xTe4 via Yb substitution, Chem. Mater. 22 (9) (2010) 2995–2999, https://doi.org/10.1021/cm1004054.

[16] T.H. Ramsey, H. Steinfink, E.J. Weiss, Thermoelectric and electrical measurements in the La – Te system, J. Appl. Phys. 36 (2) (1965) 548–553.

[17] R.C. Vickery, H.M. Muir, Thermoelectric properties of rare earth chalcogenides, Adv. Energy Convers. 1 (1961) 179–186, https://doi.org/10.1016/0365-1789(61)90031-5, doi:10.1016/0365-1789(61)90031-5.

[18] V. Ravi, S. Firdosy, T. Caillat, E. Brandon, K. Van Der Walde, L. Maricic, A. Sayir, Thermal expansion studies of selected high-temperature thermoelectric materials, J. Electron. Mater. 38 (7) (2009) 1433–1442, https://doi.org/10.1007/s11664-009-0734-2.

[19] M.M. Al Malki, X. Shi, P. Qiu, G.J. Snyder, D.C. Dunand, Creep behavior and post-creep thermoelectric performance of the n-type thermoelectric alloy Yb0.3Co4Sb12, J. Materiomics 7 (1) (2021) 89–97, https://doi.org/10.1016/j.jmat.2020.07.012, 10.1016/j.jmat.2020.07.012.

[20] J.P. Male, L. Abdellaoui, Y. Yu, S. Zhang, N. Pienack, O. Cojocaru-Mirédin, C. Scheu, G.J. Snyder, Dislocations stabilized by point defects increase brittleness in PbTe, Adv. Funct. Mater. (2021): 2108006, https://doi.org/10.1002/adfm.202108006.

[21] G. Li, Q. An, B. Duan, L. Bernstein, M.A. Malki, M. Wood, H. Avdeenko, P. Zhai, Q. Zhang, S.I. Morozov, W.A. Goddard, G.J. Snyder, Fracture toughness of thermoelectric materials, Mater. Sci. Eng. R Rep. 144 (February) (2021) 1–12, https://doi.org/10.1016/j.mser.2021.100607.

[22] G. Li, H. Avdeenko, B. Duan, M.T. Agne, H. Wang, M. Wood, Q. Zhang, P. Zhai, W. A. Goddard, G.J. Snyder, Micro- and nanomechanical properties of thermoelectric lead chalcogenides, ACS Appl. Mater. Interfaces 9 (46) (2017) 40488–40496, https://doi.org/10.1021/acsami.7b15651. https://pubs.acs.org/doi/10.1021/acsami.7b15651. www.acsami.org.

[23] L. Bernstein, M.T. Agne, J.P. Male, S. Anand, G. Li, S.I. Morozov, G.J. Snyder, Estimating the lower-limit of fracture toughness from ideal-strength calculations, Mater. Horiz. (2022), https://doi.org/10.1039/d1mh01831k.

[24] G. Li, H. Avdeenko, M. Wood, W.A. Goddard, P. Zhai, Q. Zhang, G.J. Snyder, Mechanical properties of thermoelectric lanthanum telluride from quantum mechanics, J. Phys. Appl. Phys. 50 (27) (2017), https://doi.org/10.1088/1361-6463/aa7625.

[25] J.M. Ma, Improving the Mechanical Strength and Power Conversion Efficiency of High Temperature Thermoelectrics, Ph.D. thesis, University of California Los Angeles, 2019, https://escholarship.org/uc/item/0th2s0as.

[26] J.M. Ma, S.K. Bux, J.-P. Fleurial, V.A. Ravi, S.A. Firdosy, K. Star, R.B. Kaner, High Performance High Temperature Thermoelectric Composites with Metallic Inclusions, 2017, 5.

[27] K. Ikeda, K.A. Gschneidner, B.J. Beaudry, U. Atzmony, Heat capacity in superconducting and normal-state $LaSe_x$ (1.333 < ~x < ~1.500) compounds, Phys. Rev. B 25 (7) (1982) 4604–4617, https://doi.org/10.1103/PhysRevB.25.4604.

[28] A.F. May, M.A. McGuire, C. Cantoni, B.C. Sales, Physical properties of Ce 3-xTe 4 below room temperature, Phys. Rev. B Condens. Matter 86 (3) (2012) 1–8, https://doi.org/10.1103/PhysRevB.86.035135.

[29] V.V. Tikhonov, V.N. Svechnikov, R.G. Valeeva, A. Smirnov, Debye temperature of the La3Te-La2Te3 system, Sov. Phys. Solid State 17 (4) (1975) 795.

[30] O. Delaire, A.F. May, M.A. McGuire, W.D. Porter, M.S. Lucas, M.B. Stone, D. L. Abernathy, V.A. Ravi, S.A. Firdosy, G.J. Snyder, Phonon density of states and heat capacity of La3-x Te4, Phys. Rev. B Condens. Matter 80 (18) (2009) 1–9, https://doi.org/10.1103/PhysRevB.80.184302.

[31] T.J. Slade, S. Anand, M. Wood, J.P. Male, K. Imasato, D. Cheikh, M.M. Al Malki, M. T. Agne, K. Griffith, S.K. Bux, C. Wolverton, M.G. Kanatzidis, J.G. Snyder, Charge-carrier-mediated Lattice Softening Contributes to High zT in Thermoelectric Semiconductors, Joule 5 (5) (2021) 1168–1182, https://doi.org/10.1016/j.joule.2021.03.009.

[32] D.K. Shetty, I.G. Wright, P.N. Mincer, A.H. Clauer, Indentation fracture of WC-Co cermets, J. Mater. Sci. 20 (5) (1985) 1873–1882, https://doi.org/10.1007/BF00555296.

[33] C.B. Ponton, R.D. Rawlings, Vickers indentation fracture toughness test Part 1 review of literature and formulation of standardised indentation toughness equations, Mater. Sci. Technol. 5 (9) (1989) 865–872, https://doi.org/10.1179/mst.1989.5.9.865.

[34] R. Hanus, M.T. Agne, A.J. Rettie, Z. Chen, G. Tan, D.Y. Chung, M.G. Kanatzidis, Y. Pei, P.W. Voorhees, G.J. Snyder, Lattice softening significantly reduces thermal conductivity and leads to high thermoelectric efficiency, Adv. Mater. 31 (21) (2019): 1900108, https://doi.org/10.1002/adma.201900108. https://onlinelibrary.wiley.com/doi/full/10.1002/adma.201900108.

[35] G. Tan, S. Hao, R.C. Hanus, X. Zhang, S. Anand, T.P. Bailey, A.J.E. Rettie, X. Su, C. Uher, V.P. Dravid, G.J. Snyder, C. Wolverton, M.G. Kanatzidis, High thermoelectric performance in SnTe–AgSbTe2 alloys from lattice softening, giant phonon-vacancy scattering, and valence band convergence, ACS Energy Lett. 3 (3) (2018) 705–712, https://doi.org/10.1021/acsenergylett.8b00137. https://pubs.acs.org/sharingguidelines.

[36] T.J. Slade, K. Pal, J.A. Grovogui, T.P. Bailey, J. Male, J.F. Khoury, X. Zhou, D. Y. Chung, G.J. Snyder, C. Uher, V.P. Dravid, C. Wolverton, M.G. Kanatzidis, Contrasting SnTe-NaSbTe2and SnTe-NaBiTe2Thermoelectric alloys: high performance facilitated by increased cation vacancies and lattice softening, J. Am. Chem. Soc. 142 (28) (2020) 12524–12535, https://doi.org/10.1021/jacs.0c05650.

[37] T. Parashchuk, B. Wiendlocha, O. Cherniushok, R. Kosyl, K.T. Wojciechowski, High thermoelectric performance of p-type PbTe enabled by the synergy of resonance scattering and lattice softening, ACS Appl. Mater. Interfaces 13 (41) (2021) 49027–49042, https://doi.org/10.1021/acsami.1c14236, 10.1021/acsami.1c14236.

[38] K. Skokánková, H. Bach, R. Wäppling, S. Modrow, Superconducting La 3-x S 4 compounds, J. Phys. F Met. Phys. 10 (1980) 2459.

[39] G.D. Quinn, R.C. Bradt, On the Vickers indentation fracture toughness Test, J. Am. Ceram. Soc. 90 (3) (2007) 673–680, https://doi.org/10.1111/j.1551-2916.2006.01482.x.
[40] J. Eilertsen, M.A. Subramanian, J.J. Rasimas, Fracture toughness of Co4Sb12 and in 0.1Co4Sb12 thermoelectric skutterudites evaluated by three methods, J. Alloys Compd. 552 (2013) 492–498, https://doi.org/10.1016/j.jallcom.2012.11.066, 10.1016/j.jallcom.2012.11.066.
[41] C.B. Ponton, R.D. Rawlings, Vickers indentation fracture toughness test Part 2 application and critical evaluation of standardised indentation toughness equations, Mater. Sci. Technol. 5 (10) (1989) 961–976, https://doi.org/10.1179/mst.1989.5.10.961.
[42] F. Kosmac, M. Antonov, Comparative study on indentation fracture toughness measurements of cermets and cemented carbides, Proc. Estonian Acad. Sci. Eng. 12 (4) (2006) 388–398.
[43] E. Broitman, Indentation hardness measurements at macro-, micro-, and nanoscale: a critical overview, Tribol. Lett. 65 (1) (2017) 1–18, https://doi.org/10.1007/s11249-016-0805-5.
[44] J.S. Tse, Intrinsic hardness of crystalline solids, J. Superhard Mater. 3 (3) (2010) 46–65, https://doi.org/10.3103/S1063457610030044.
[45] E. Mazhnik, A.R. Oganov, A model of hardness and fracture toughness of solids, J. Appl. Phys. 126 (12) (2019), https://doi.org/10.1063/1.5113622.
[46] H. Niu, S. Niu, A.R. Oganov, Simple and accurate model of fracture toughness of solids, J. Appl. Phys. 125 (6) (2019), https://doi.org/10.1063/1.5066311, 10.1063/1.5066311.
[47] Y. Wang, Y.J. Hu, X. Chong, J.P.S. Palma, S.A. Erickson, K.E. Star, J.P. Fleurial, V. A. Ravi, S.L. Shang, L.Q. Chen, Z.K. Liu, Quasiharmonic calculations of thermodynamic properties for La3-xTe4 system, Compos. Mater. Sci. 142 (2018) 417–426, https://doi.org/10.1016/j.commatsci.2017.10.036.
[48] A. Zevalkink, D.M. Smiadak, J.L. Blackburn, A.J. Ferguson, M.L. Chabinyc, O. Delaire, J. Wang, K. Kovnir, J. Martin, L.T. Schelhas, T.D. Sparks, S.D. Kang, M. T. Dylla, G.J. Snyder, B. Ortiz, E. Toberer, A practical field guide to thermoelectrics: fundamentals, synthesis, and characterization, Appl. Phys. Rev. 5 (2015) (2018): 021303, https://doi.org/10.1063/1.5021094.
[49] R. Hanus, R. Gurunathan, L. Lindsay, M.T. Agne, J. Shi, S. Graham, G.J. Snyder, Thermal transport in defective and disordered materials, Appl. Phys. Rev. 8 (2021): 031311, https://doi.org/10.1063/5.0055593.
[50] B.H. Toby, R.B. Von Dreele, GSAS-II: the genesis of a modern open-source all-purpose crystallography software package, J. Appl. Crystallogr. 46 (2) (2013) 544–549, https://doi.org/10.1107/S0021889813003531.